8-2022

Neuronal Rhythms: Network And Cell-Based Mechanisms

Ricardo J. Erazo-Toscano
Georgia State University

Neuronal Rhythms: Network And Cell-Based Mechanisms

by

Ricardo Erazo-Toscano

Under the Direction of Gennady Cymbalyuk, PHD

A Dissertation Submitted in Partial Fulfillment of the Requirements for the Degree of

Doctor of Philosophy

In the College of Arts and Sciences

Georgia State University

2022

ABSTRACT

Life-supporting rhythmic motor functions like heart beating in invertebrates and breathing in vertebrates require indefatigable generation of a robust rhythm by specialized oscillatory circuits, Central Pattern Generators (CPGs). Yet, CPGs should be sufficiently flexible to adjust to changes of the environment and behavioral goals. Neuromodulation modifies the CPG's rhythm by co-regulating multiple ionic currents, including the Na^+/K^+ pump current, I_{pump}. In the leech heartbeat CPG, endogenous neuropeptide myomodulin downregulates I_{pump} and upregulates I_h to speed up the CPG's rhythm (Tobin & Calabrese, 2005). The interaction of these currents dramatically speeds up rhythm of the leech heartbeat CPG when I_{pump} is activated by increased internal Na^+ concentration, $[Na^+]_i$, produced by application of monensin(Kueh et al., 2016a). Comodulation of I_{pump} and I_h supports the CPG's functional activity in a wider range of the pattern's cycle period and avoids dysfunctional regimes (Ellingson et al., 2021).

We anticipate that interaction of I_{pump} and persistent Na^+ current, I_P, produces a mechanism supporting functional bursting. I_{pump} is an outward current activated by $[Na^+]_i$ and is a major source of Na^+ efflux. I_P is a low voltage activated inward current and is a major source of Na^+ influx. Both currents are active between and during bursts. We apply a combination of electrophysiology, computational modeling, and dynamic clamp to investigate the role of I_{pump} and I_P in the leech heartbeat CPG interneurons (HNs). Applying dynamic clamp, introducing additional I_{pump} and I_P into the dynamics of a living synaptically isolated HN neuron in real time (Erazo-Toscano et al., 2021), we show that their joint upregulation produces transition into a new bursting regime characterized by higher spiking frequency and more depolarized base potential during the burst. Further upregulation of I_{pump} speeds up the HN rhythm by shortening burst duration and interburst interval.

In summary, dynamic interaction of Na^+/K^+ pump current with persistent Na^+ current offers a mechanism of generation and regulation of robust and flexible pattern of bursting activity.

INDEX WORDS: Central pattern generator, Interneuron, Invertebrate, Oscillatory networks, Electrophysiology, Bursting neuron, Interneuron, Waves.

Neuronal Rhythms: Network And Cell-Based Mechanisms

by

Ricardo Erazo-Toscano

Committee Chair: Gennady Cymbalyuk

Committee: Ronald Calabrese

Remus Osan

Vladimir Bondarenko

Yaroslav Molkov

Astrid Prinz

Electronic Version Approved:

Office of Graduate Services

College of Arts and Sciences

Georgia State University

July 2022

DEDICATION

I dedicate this dissertation first and foremost to my papá, may he rest in peace, he taught me the skills I needed to push forth all my years of academic and personal life.

My wife Carolina who has stood by my side during the toughest and happiest times of my life.

To my mother who continues to be a driving force in my motivation

To my brother for his artistic and moral support

To all friends I made during my graduate career

All faculty who taught me useful neuroscience theory and practical skills I have applied to earn this degree

My former and current mentors: Remus Osan, Gennady Cymbalyuk, and Ronald Calabrese

TABLE OF CONTENTS

LIST OF TABLES

LIST OF FIGURES

LIST OF ABBREVIATIONS

CPG – Central pattern generator

HN – leech heart CPG interneuron

HCO – Half-center oscillator

Na^+ – sodium ion

K^+ – potassium ion

I_P – persistent Na^+ current

$\bar{g}_P$ – maximal conductance of I_P

I_{pump} – Na^+/K^+ pump current

I_{max}^{pump} – maximal I_{pump}

I_h – the hyperpolarization-activated current

$\bar{g}_h$ – maximal conductance of I_h

$[Na^+]_i$ – intracellular Na^+ concentration

BD – Burst Duration

IBI – Interburst interval

LIF – Leaky-Integrate-and-Fire

1 INTRODUCTION

Daily rhythmic movements such as walking, breathing, and invertebrate heart-beating are controlled by oscillatory neuronal networks known as Central Pattern Generators (CPG) (Calabrese et al., 2016; Marder & Bucher, 2001). Neuronal rhythmicity results from combinations of endogenous membrane currents and synaptic interactions between neurons (Marder & Bucher, 2001; Marder & Calabrese, 1996). CPGs share biophysical properties that support bursting activity; endogenous bursting neurons are ubiquitous building blocks of CPGs. Traveling waves of rhythmic motor patterns support an adaptable scheme for relaying neuronal rhythms in neuron networks (C. A. Cuellar et al., 2009; Dou et al., 2018; Ijspeert et al., 2007; Landsman & Slotine, 2012; Yokoyama et al., 2017). Traveling waves represent neuronal activity as a function of space and time, while neuronal rhythms represent neuron activity as a function of time. To represent synaptic and neuronal activity as a function of space, mathematical models are developed to represent neuronal connectivity as a function of space; such that, determined by a specific mathematical function (connectivity kernel), neurons are coupled to their nearest neighbors and the strength of the synaptic coupling decays as a function of the connectivity kernel and space; synaptic propagation is the result of synaptic and membrane currents.

Rhythmically active neurons have an array of membrane currents that allow the neuron to oscillate rhythmically (Marder & Bucher, 2001; Marder & Calabrese, 1996; Marder & Prinz, 2002; Prinz, Bucher, et al., 2004). Among such currents are non-inactivating persistent Na^+ current (I_P) and the Na^+/K^+ pump current (I_{pump}). I_P begins to activate near -60mV and saturates around -20mV; I_P can be activa during the spiking and silent phases of the bursting cycle. I_P triggers and maintains burst firing (Angstadt & Calabrese, 1989; Butera Jr et al., 1999; Del Negro et al., 2002; Elson & Selverston, 1997; Harris-Warrick, 2002; Opdyke & Calabrese, 1994; Prinz, Bucher, et al., 2004; Rybak et al., 2004; Rybak et al., 2003). A little-known contributor to

bursting activity is a Na^+/K^+ pump. The classical role of the pump is to maintain gradients; however, the Na^+/K^+ pump also produces outward current as it exchanges Na^+ and K^+ ions in an asymmetric fashion (Glitsch, 2001; Glynn, 1993; Skou, 1988). The current produced by the Na^+/K^+ pump plays an important role influencing rhythmic neuronal activity (Canavier, 1999; Jasinski et al., 2013; Koester & Siegelbaum, 2013; Li et al., 1996; Picton, Nascimento, et al., 2017; Picton, Zhang, et al., 2017; Rybak et al., 2014; Tobin & Calabrese, 2005a; Zhang et al., 2015; Zhang & Sillar, 2012). Activation of I_{pump} is voltage-independent and activity-dependent; I_{pump} is activated by intracellular Na^+ concentration ($[Na^+]_i$). I_{pump} can be controlled by neuromodulators (Dobretsov & Stimers, 2005; Tobin & Calabrese, 2005a). Due to their activation kinetics, I_P and I_{pump} can be active during the cycle's silent and active phases. We suggest I_P and I_{pump} could interact through Na^+ flux.

The leech heartbeat network is a unique testbed for ideas about rhythmogenesis in CPGs; experimental evidence comes together with biophysical modeling to provide grounds for these questions. The leech heartbeat CPG is a circuit of uniquely identifiable neurons. The heart CPG is comprised of endogenously bursting interneurons (HN) (Cymbalyuk et al., 2002a). All HN neurons are accessible for experimental manipulation. They produce stereotypical rhythmic patterns in synaptically coupled and isolated preparations (Cymbalyuk et al., 2002a). Kinetics of most HN currents have been characterized in voltage-clamp experiments (Angstadt & Calabrese, 1989, 1991; Olsen & Calabrese, 1996; Olsen et al., 1995). The HN model has made accurate predictions about HN currents and rhythmicity (Cymbalyuk & Calabrese, 2000, 2001; Kueh et al., 2016; Olypher et al., 2006a; Sorensen et al., 2002; Sorensen et al., 2004a). Previous real-time hybrid systems implementations with HN models and neurons proved to be a fruitful method to investigate the roles of intrinsic currents (Harris-Warrick, 2002; Olypher et al., 2006a; Sorensen et al., 2002; Sorensen et al., 2004a). We developed a new generation of hybrid real-time systems that estimate sodium concentration. Our dynamic clamp

implementation allowed us to study dynamic interactions between I_P and I_{pump} in a living rhythmic HN neuron. The real-time hybrid systems we use have proved advantageous to investigate basic principles that support rhythmic oscillations in HN neurons; we innovate with a dynamic clamp current based on dynamical evaluation of $[Na^+]_i$.

The activity of the Na^+/K^+ pump modulates bursting characteristics in rhythmically active neurons. Application of myomodulin decreases the period of the HN cycle in a dose-dependent fashion (Masino & Calabrese, 2002a). Myomodulin inhibits the Na^+/K^+ pump in HN neurons. Inhibition of the pump depolarized HN neurons without affecting membrane conductances; inhibition of the pump also decreased the HN cycle period (Tobin & Calabrese, 2005a). Monensin is a Na^+/H^+ antiporter which increases intracellular sodium concentration ($[Na^+]_i$) (Huczyski et al., 2007; Itoh et al., 2000); monensin stimulates the Na^+/K^+ pump. Application of monensin reduced HN burst duration and interburst interval. When monensin was applied, and I_h was blocked, HN interburst interval increased while burst duration stayed consistent with preparations with intact I_h (Kueh et al., 2016). These experiments highlighted the importance of the Na^+/K^+ pump in rhythm generation.

The persistent sodium current (I_P) plays an important role in initiating bursts and supporting spike frequency. However, in the HN model, I_P must be appropriately controlled. The model's sensitivity suggests this current as a critical player in the rhythm of HN neurons. Rhythmic oscillations in the HN model are sensitive to parameters that determine I_P; too much I_P produces tonic spiking activity while not enough I_P makes quiescence (Doloc-Mihu & Calabrese, 2016). HN HCO models predict that I_P lengthens the HN period (Cymbalyuk & Calabrese, 2001; Nadim et al., 1995; Olsen et al., 1995) and increases spike frequency (Nadim et al., 1995; Olsen et al., 1995). Modeling studies indicated that upregulation of I_P increases the HN period (Nadim et al., 1995; Olsen et al., 1995); I_P interacts with persistent K^+ current (I_{K2}) to produce long interplateau potentials (Cymbalyuk & Calabrese, 2001). I_P and I_{pump} can be active throughout the

cycle; their interaction is essential to understand basic principles that support neuronal rhythmicity. While I_P is active, dynamic $[Na^+]_i$ grows, which subsequently would activate the Na^+/K^+ pump. Altogether, experimental evidence and computational modeling suggest that I_P and I_{pump} interact to control interburst interval (IBI) and burst duration (BD).

Our overarching hypothesis states that the interaction between I_P and I_{pump} creates a flexible mechanism that generates bursting. We performed dynamic clamp experiments. The dynamic clamp uses the measured HN membrane potential to calculate $[Na^+]_i$ and activation of I_P as a part of a dynamical system computed in real time. The calculated currents I_P and I_{pump} are injected into the cell; we propose that their interplay mechanisms interact with I_h to determine the IBI. To assess our hypothesis, we exploited the parameter control made available with the dynamic clamp. We manipulated $\bar{g}_P$ and I_{max}^{pump} separately and systematically in synaptically isolated HN neurons. We performed two series of experiments: one series of experiments in normal saline and a subsequent series with an I_h blocker. We further developed a theoretical framework beyond the hypothesis, we studied propagation of neuronal spiking activity with numerical and analytical methods, a complement to neuron activity as a function of time (oscillator interneuron rhythm), we also investigate neuronal activity as a function of space (propagation of synaptic activity in a neuronal network). Traveling waves are a robust mechanism to relay synaptic activity, support neuron synchronization, and sequentially activate ensembles of neurons (Cohen et al., 1992; Ermentrout et al., 2006; Kleinfeld et al., 1994; Osan & Ermentrout, 2002; Van Vreeswijk et al., 1994). Waves play an important role relaying the rhythmic output of CPGs to muscles and neuronal networks (Cuellar et al., 2009; Dou et al., 2018; Ijspeert et al., 2007; Landsman & Slotine, 2012; Yokoyama et al., 2017). We investigated how neuronal rhythms propagate in networks assuming that synaptic coupling depended exclusively on the spatial distance between neurons. For certain kinds of neuronal networks, characterized by the connectivity kernel supporting small ranging connections, we determined

that traveling waves propagate robustly. We investigated the dynamics that control activity propagation and explore the resilience of the traveling wave to biological perturbations such as inhomogeneities in the neuronal network.

1.1 Literature Review

The central nervous system produces functional rhythms of activity that control bodily functions such as breathing, motor movements such as walking and swimming, and invertebrate heart beating. It is widely accepted that Central Pattern Generators control these rhythmic movements (Calabrese et al., 2016; Golowasch et al., 1999; Marder & Bucher, 2001; Marder & Calabrese, 1996; Marder & Prinz, 2002). Central Pattern Generators (CPGs) are networks of neurons capable of orchestrating rhythmic activity without sensory feedback or an innate rhythmic drive from the brain (Calabrese et al., 2016; Marder & Calabrese, 1996). Half-Center Oscillator (HCO) is an essential building block of CPGs; HCO is a minimal neuronal network of two mutually inhibitory neurons (Marder & Bucher, 2001). The activity of any neuronal network is determined by the interaction of neuron's properties and their synaptic connections (Calabrese et al., 2016; Katz, 2016; Marder & Calabrese, 1996; Marder & Prinz, 2002). Single neuron membrane properties include the expression of ionic channels, which carry inward and outward currents. Interactions of membrane currents control the membrane potential of the neuron (V_m). A problem in modern neuroscience is understanding how membrane currents interact to generate robust activity patterns (Cymbalyuk & Calabrese, 2000; Kueh et al., 2016; Marder & Prinz, 2002; Prinz, Bucher, et al., 2004; Tobin & Calabrese, 2005a). The rhythm of a CPG arises from neuron membrane currents and synaptic network interactions. Understanding the principles governing neuron rhythm will add an essential building block to the framework of neuronal oscillations.

The leech heartbeat CPG is a well-characterized neuronal network that produces complex rhythmic patterns. We developed a new generation of the dynamic clamp to examine the role of

the Na^+/K^+ pump controlling rhythmic activity. Our system calculates $[Na^+]_i$ and computes the magnitude of the current I_{pump} based on the neuron's membrane potential and a full HN model running in real-time. We propose I_{pump} interacts with I_P to control bursting characteristics such as BD and IBI. The leech heart CPG is comprised of endogenous bursting identified interneurons, organized as bilateral pairs, and distributed in ganglia along the ventral nerve cord (Calabrese et al., 2016; Weaver et al., 2010; Wenning, Cymbalyuk, et al., 2004; Wenning, Hill, et al., 2004). HN neurons in ganglia 3 and 4 (HN(3) and HN(4), respectively are coupled to their contralateral counterpart and form HCOs; 0.5mM bicuculline saline blocks inhibitory synaptic input in HN neurons (Schmidt, 1992). In contrast, HN neurons in ganglia 6 and 7 (HN(6) and HN(7), respectively) are not coupled to their contralateral correspondent; these ganglia permit access to synaptically isolated HN neurons without pharmacological manipulations. HN neurons HN(3), HN(4), HN(6), and HN(7) are endogenous bursting neurons with common bursting characteristic properties (Cymbalyuk et al., 2002a), (figure 1).

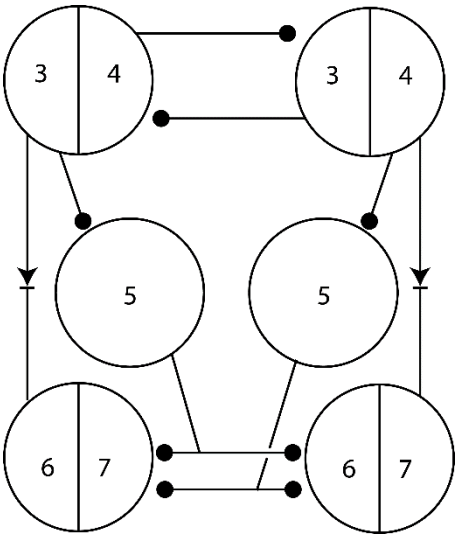

Figure 1. Circuit Diagram of leech heartbeat core CPG

The diagram shows that HN(3) and HN(4), form half-center oscillators, but HN(6) and HN(7) received their input from other ganglia and do not form HCOs (Norris et al., 2006).

The rhythmic patterns that support leech heart beating arise from the rhythmic properties of HN neurons. The Na^+/K^+ pump current (I_{pump}) and persistent Na^+ current (I_P) interact naturally to create a rhythmic system. The simplified process is: activation of I_P supports burst initiation and produces an increase of $[Na^+]_i$ (Opdyke & Calabrese, 1994); the Na^+/K^+ pump activates with $[Na^+]_i$ and produces an outward current. I_P is a current that supports oscillations in HN neurons (Opdyke & Calabrese, 1994); the interaction between I_P and persistent K^+ current (I_{K2}) has been shown to control interburst interval (Cymbalyuk & Calabrese, 2001). Doloc-Mihu and Calabrese (2011) constructed a database from simulated bursting characteristics of HN HCO models. The database allows researchers to conduct systematic exploration of the parameter space of the maximal conductances of intrinsic and synaptic currents. The database of HN HCO models consists of about 10 million simulations. The database explored the roles of maximal conductance of membrane and synaptic currents on the activity characteristics of the HN HCO models. Database analysis demonstrated HN model is very sensitive to $\bar{g}_P$; rhythmicity is possible within a limited parameter range (Doloc-Mihu & Calabrese, 2016). I_P is a persistent Na^+ current, available for activation at subthreshold potentials, and responsible for supporting rhythmicity in HN neurons.

Previous experiments demonstrated I_h interacts with I_{pump} to control the HN cycle period. Stimulation of the pump decreased BD; I_h interacts with I_{pump} to modulate IBI (Koester & Siegelbaum, 2013). I_h is the hyperpolarization-activated slow inward current. I_h begins to activate near -50mV and is fully activated near -75mV. I_h can be blocked with extracellular Cs^+; I_h supports recovery from inhibition and escape and release mechanisms of HCO rhythmicity (Angstadt & Calabrese, 1989; Wang & Rinzel, 1992). From an evolutionary perspective, CPGs share particular characteristics that facilitate the expression of rhythmic behavior, such as reciprocal inhibition and post-inhibitory rebound in HCO motifs (Katz, 2016). HCO motifs with inhibitory coupling support the alternating activity of the pair. Normal HN rhythmic activity

depends on I_h (Angstadt & Calabrese, 1989; Kueh et al., 2016). To fathom how the interaction of I_h, I_P, and I_{pump} control the HN rhythm, we performed experiments with normal saline and with 2mM Cs^+ (Schmidt, 1992). We blocked I_h to separate the oscillating behavior with and without this current. I_h is an important current supporting robust HN rhythmicity; I_h responds dynamically to other membrane currents.

In the context of rhythmic oscillations, what specific roles could the Na^+/K^+ pump play to control the periodic behavior of the neuron? It is widely accepted that in a neuron at rest, the Na^+/K^+ pump activity keeps stable Na^+ and K^+ gradients so that membrane potential (V_m) is constant (Brines et al., 1995; Calandriello et al., 1995; Ellis et al., 2003; Koester & Siegelbaum, 2013; Lees, 1993). In this dissertation, we explore a novel role of the Na^+/K^+ pump.

The Na^+/K^+ pump is phylogenetically preserved in vertebrate and invertebrate animals. The pump has several functional isoforms, among which α3β1 isoform is selectively expressed in neurons (Dobretsov & Stimers, 2005). The isoform α3β1 is activated only at high $[Na^+]_i$, for example, due to a burst of action potentials. The Na^+/K^+ pump is the enzyme that exchanges three intracellular Na^+ for two extracellular K^+ ions. The asymmetric exchange of ions produces an outward current. The classical role of the pump is to produce membrane gradients and sustain resting membrane potential (Dobretsov & Stimers, 2005). The novel role of the pump is to respond dynamically to $[Na^+]_i$ and interact with other membrane currents in a time scale of seconds. The pump's affinity to Na^+ enables an activity-dependent neuronal response. In the leech heartbeat CPG, the Na^+/K^+ pump current interacts with other endogenous currents to control the HN period (Kueh et al., 2016; Tobin & Calabrese, 2005a). In the Xenopus tadpole swimming CPG, the Na^+/K^+ pump is responsible for the ultra-slow afterhyperpolarization that follows continuous high-frequency neuronal firing characteristic of episodes of fictive locomotion (Zhang et al., 2015; Zhang & Sillar, 2012). In the rat locomotor CPG, the Na^+/K^+ pump controls the period of locomotor activity. Application of ouabain inhibits the pump and increases the

duration of locomotor activity; on the other hand, application of monensin stimulates the pump and decreases the time of locomotor bout (Picton, Nascimento, et al., 2017; Picton, Zhang, et al., 2017). In the pre-Botzinger complex, the persistent slow-inactivating Na^+ current (I_{NaP} ; similar to the leech I_P) is a subthreshold current supporting rhythmogenic properties. I_{NaP} interacts with burst terminating mechanisms to support rhythmic oscillations (Jasinski et al., 2013; Rybak et al., 2014). If expressed without compensatory outward current, I_{NaP} can induce seizures (Lin et al., 2012). Altogether, the experiments described demonstrate that the Na^+/K^+ pump plays a dynamic role in controlling neuronal activity; however, the exact function of the Na^+/K^+ pump coordinating neuronal rhythmicity remains not well understood.

HN(7) neurons allowed us to study single neuron dynamics without pharmacological manipulations; in contrast, HN(6)s are in a ganglion that has many motor neurons and the location of the HN(6) neurons is not as easily identifiable as of the HN(7) neurons. The baseline state of HN(7) neurons is in isolated ganglia in normal saline. The baseline $[Na^+]_i$ is the average of the calculated concentration over 8 or more cycles. At the baseline, isolated HN neurons burst endogenously. The endogenous baseline activity is disrupted by a nonspecific leak current introduced by the penetration of the sharp microelectrode (Cymbalyuk et al., 2002a). Our data show that the endogenous HN rhythm may be restored in living neurons impaled with sharp microelectrodes with the dynamic clamp technique by injecting I_{pump} and I_P. (Chapters 2, 3 and 4). The natural interaction between I_P and I_{pump} can support a basic rhythmogenic system. These currents interact through the intracellular sodium concentration and membrane potential.

In contrast, chapter 5 focuses on the theoretical implications to rhythmic and synaptic activity propagation. The problem of synaptic propagation affects ubiquitous neuronal activities, functional and pathological. A widely accepted assumption of traveling wave studies is that synaptic coupling can be represented as a function of space, with different mathematical functions representing short range (finite support kernel), mid-range (Gaussian kernel), and long

range connections (exponential kernel). Zhang and Osan (2016) found analytical solutions to the wave evolution in neuronal networks with the exponential kernel. Because the method includes derivations of the integral form of the Leaky-Integrate-and-Fire (LIF) model, derivations of the Gaussian kernel are too complex. In the finite support connectivity kernel, the connectivity function assumes that neurons are only coupled to their nearest neighbors within a synaptic space constant (σ), and that the strength of synaptic coupling does not decay with distance; therefore, one neuron is equally coupled to all neurons within one σ. Previous work demonstrated that networks with this kernel support traveling waves of activity (Ermentrout et al., 2006; Osan et al., 2003).

On one hand, neuronal rhythms represent neuron activities as a function of time; on the other hand, synaptic propagation represents neuron activities as a function of space. The finite support kernel mathematically represents space-dependent neuronal connectivity. Because of the simple assumptions of the finite support kernel, the findings provide general insights about synaptic activity propagation in neuronal networks.

1.2 Innovation

We implemented in real-time the augmented HN model that implements Na^+/K^+ pump dynamics (Erazo-Toscano, R. J., Ellingson, P. J., Calabrese, R. L., & Cymbalyuk, G. S. (2021) JoVE , (171), e61473; Erazo-Toscano, R. J., Fomenko, M., Core, S., Calabrese, R. L., Cymbalyuk, G. S. e. eNeuro (to be submitted)). We used this model to develop a new generation of real-time hybrid systems and investigate experimentally how the activity of the Na^+/K^+ pump shapes HN rhythmicity. The control of the Na^+/K^+ pump of bursting characteristics of rhythmic neurons has never been studied with the experimental control made available by the dynamic clamp. The pharmacological manipulations to stimulate and inhibit the pump do not grant the specific

parameter control of our dynamic clamp. The development of this fundamental tool allows us to research the role of the I_{pump} on the rhythmicity of HN neurons.

We investigated how the Na^+/K^+ pump sculpts neuron bursts and controls periodic oscillations. The dynamic response of the pump in an oscillatory system is not well understood. In contrast to other endogenous membrane currents, I_{pump} is voltage-independent but activity-dependent; this key characteristic activates I_{pump} as a response to spiking activity and keeps it active while the neuron is hyperpolarized.

The first objective of this dissertation is to investigate the role of the interaction of I_P and I_{pump} in controlling the bursting characteristics of isolated oscillator interneurons. The second objective is to understand how the interaction of I_P, I_{pump}, and I_h in controlling the interburst interval of isolated oscillation interneurons. The last objective of this dissertation is to characterize synaptic propagation in neuronal networks. The individual neuron and network connectivity characteristics determine the dynamics of activity propagation.

1.3 References

Angstadt, J. D., & Calabrese, R. L. (1989). A hyperpolarization-activated inward current in heart interneurons of the medicinal leech. *Journal of Neuroscience*, *9*(8), 2846-2857.

Angstadt, J. D., & Calabrese, R. L. (1991). Calcium currents and graded synaptic transmission between heart interneurons of the leech. *Journal of Neuroscience*, *11*(3), 746-759.

Barnett, W., & Cymbalyuk, G. (2011). Hybrid Systems Analysis: Real-Time Systems for Design and Prototyping of Neural Interfaces and Prostheses. *Biohybrid Systems: Nerves, Interfaces, and Machines*, 115-138.

Brines, M. L., Dare, A. O., & de Lanerolle, N. C. (1995). The cardiac glycoside ouabain potentiates excitotoxic injury of adult neurons in rat hippocampus. *Neuroscience letters*, *191*(3), 145-148.

Butera Jr, R. J., Rinzel, J., & Smith, J. C. (1999). Models of respiratory rhythm generation in the pre-Botzinger complex. II. Populations of coupled pacemaker neurons. *Journal of Neurophysiology*, *82*(1), 398-415.

Calabrese, R. L., Norris, B. J., & Wenning, A. (2016). The neural control of heartbeat in invertebrates. *Current Opinion in Neurobiology*, *41*, 68-77.

Calandriello, L., Curini, R., Pennisi, E. M., & Palladini, G. (1995). Spongy state (status spongiosus) and inhibition of Na, K-ATPase: a pathogenetic theory. *Medical hypotheses*, *44*(3), 173-178.

Canavier, C. C. (1999). Sodium dynamics underlying burst firing and putative mechanisms for the regulation of the firing pattern in midbrain dopamine neurons: a computational approach. *Journal of computational neuroscience*, *6*(1), 49-69.

Cohen, A. H., Ermentrout, G. B., Kiemel, T., Kopell, N., Sigvardt, K. A., & Williams, T. L. (1992). Modelling of intersegmental coordination in the lamprey central pattern generator for locomotion. *Trends in Neurosciences*, *15*(11), 434-438.

Cuellar, Tapia, J. A., Jurez, V., Quevedo, J., Linares, P., Martnez, L., & Manjarrez, E. (2009). Propagation of Sinusoidal Electrical Waves along the Spinal Cord during a Fictive Motor Task. *J. Neurosci.*, *29*(3), 798-810.

Cuellar, C. A., Tapia, J. A., Juárez, V., Quevedo, J., Linares, P., Martínez, L., & Manjarrez, E. (2009). Propagation of sinusoidal electrical waves along the spinal cord during a fictive motor task. *Journal of Neuroscience*, *29*(3), 798-810.

Cymbalyuk, G. S., & Calabrese, R. L. (2000). Oscillatory behaviors in pharmacologically isolated heart interneurons from the medicinal leech. *Neurocomputing*, *32*, 97-104.

Cymbalyuk, G. S., & Calabrese, R. L. (2001). A model of slow plateau-like oscillations based upon the fast Na+ current in a window mode. *Neurocomputing*, *38*, 159-166.

Cymbalyuk, G. S., Gaudry, Q., Masino, M. A., & Calabrese, R. L. (2002). Bursting in leech heart interneurons: cell-autonomous and network-based mechanisms. *Journal of Neuroscience*, *22*(24), 10580-10592.

Del Negro, C. A., Koshiya, N., Butera Jr, R. J., & Smith, J. C. (2002). Persistent sodium current, membrane properties and bursting behavior of pre-botzinger complex inspiratory neurons in vitro. *Journal of Neurophysiology*, *88*(5), 2242-2250.

Devices, M. (2008). The Axon Guide, A Guide to Electrophysiology & Biophysics Laboratory Techniques. *MDS Analytical Technologies, Sunnyvale, CA, USA*.

Dobretsov, M., & Stimers, J. R. (2005). Neuronal function and alpha3 isoform of the Na/K-ATPase. *Front Biosci*, *10*, 2373-2396.

Doloc-Mihu, A., & Calabrese, R. L. (2014). Identifying Crucial Parameter Correlations Maintaining Bursting Activity. *PLoS Comput. Biol.*, *10*(6), e1003678.

Doloc-Mihu, A., & Calabrese, R. L. (2016). Analysis of family structures reveals robustness or sensitivity of bursting activity to parameter variations in a half-center oscillator (HCO) model. *eNeuro*, *3*(4).

Dou, Y., Pandey, S., Cartier, C. A., Miller, O., & Bishop, K. J. (2018). Emergence of traveling waves in linear arrays of electromechanical oscillators. *Communications Physics*, *1*(1), 1-9.

Ellis, D. Z., Rabe, J., & Sweadner, K. J. (2003). Global loss of Na, K-ATPase and its nitric oxide-mediated regulation in a transgenic mouse model of amyotrophic lateral sclerosis. *Journal of Neuroscience*, *23*(1), 43-51.

Elson, R. C., & Selverston, A.. I. (1997). Evidence for a persistent Na+ conductance in neurons of the gastric mill rhythm generator of spiny lobsters. *Journal of Experimental Biology*, *200*(12), 1795-1807.

Ermentrout, B., Rubin, J., & Osan, R. (2006). Regular Traveling Waves in a One-Dimensional Network of Theta Neurons. *SIAM J. Appl. Math.* https://epubs.siam.org/doi/abs/10.1137/S0036139901387253

Glitsch, H. G. n. (2001). Electrophysiology of the sodium-potassium-ATPase in cardiac cells. *Physiological Reviews*, *81*(4), 1791-1826.

Glynn, I. M. (1993). All hands to the sodium pump (Annual Review Prize Lecture). *J. Physiol*, *462*, 1-30.

Golowasch, J., Casey, M., Abbott, L. F., & Marder, E. (1999). Network stability from activity-dependent regulation of neuronal conductances. *Neural Computation*, *11*(5), 1079-1096.

Harris-Warrick, R. M. (2002). Voltage-sensitive ion channels in rhythmic motor systems. *Current Opinion in Neurobiology*, *12*(6), 646-651.

Hill, A. A. V., Lu, J., Masino, M. A., Olsen, O. H., & Calabrese, R. L. (2001). A model of a segmental oscillator in the leech heartbeat neuronal network. *Journal of computational neuroscience*, *10*(3), 281-302.

Hill, A. A. V., Masino, M. A., & Calabrese, R. L. (2002). Model of intersegmental coordination in the leech heartbeat neuronal network. *Journal of Neurophysiology*, *87*(3), 1586-1602.

Huczyski, A., Ratajczak-Sitarz, M., Katrusiak, A., & Brzezinski, B. (2007). Molecular structure of the 1: 1 inclusion complex of monensin A sodium salt with acetonitrile. *Journal of molecular structure*, *832*(1-3), 84-89.

Ijspeert, A. J., Crespi, A., Ryczko, D., & Cabelguen, J.-M. (2007). From swimming to walking with a salamander robot driven by a spinal cord model. *science*, *315*(5817), 1416-1420.

Itoh, Y., Law, M. J., & Sokoloff, L. (2000). Effects of the Na+/H+ exchanger monensin on intracellular pH in astroglia. *Brain research*, *882*(1-2), 226-229.

Jasinski, P. E., Molkov, Y. I., Shevtsova, N. A., Smith, J. C., & Rybak, I. A. (2013). Sodium and calcium mechanisms of rhythmic bursting in excitatory neural networks of the pre-B otzinger complex: a computational modelling study. *European Journal of Neuroscience*, *37*(2), 212-230.

Katz, P. S. (2016). Evolution of central pattern generators and rhythmic behaviours. *Philosophical Transactions of the Royal Society B: Biological Sciences*, *371*(1685), 20150057.

Kleinfeld, D., Delaney, K. R., Fee, M. S., Flores, J. A., Tank, D. W., & Gelperin, A. (1994). Dynamics of propagating waves in the olfactory network of a terrestrial mollusk: an electrical and optical study. *Journal of Neurophysiology*.

Koester, J., & Siegelbaum, S. A. (2013). Membrane potential and the passive electrical properties of the neuron. *Principles of neural science, Ed*, *5*, 126-147.

Kueh, D., Barnett, W. H., Cymbalyuk, G. S., & Calabrese, R. L. (2016). Na+/K+ pump interacts with the h-current to control bursting activity in central pattern generator neurons of leeches. *Elife*, *5*, e19322.

Landsman, A. S., & Slotine, J.-J. (2012). Control of traveling-wave oscillations and bifurcation behavior in central pattern generators. *Physical Review E*, *86*(4), 041914.

Lees, G. J. (1993). Contributory mechanisms in the causation of neurodegenerative disorders. *Neuroscience*, *54*(2), 287-322.

Li, Y.-X., Bertram, R., & Rinzel, J. (1996). Modeling N-methyl-D-aspartate-induced bursting in dopamine neurons. *Neuroscience*, *71*(2), 397-410.

Lin, W.-H., Gnay, C., Marley, R., Prinz, A. A., & Baines, R. A. (2012). Activity-dependent alternative splicing increases persistent sodium current and promotes seizure. *Journal of Neuroscience*, *32*(21), 7267-7277.

Marder, E. (1991). Plateaus in time. *Current Biology*, *1*(5), 326-327.

Marder, E., & Bucher, D. (2001). Central pattern generators and the control of rhythmic movements. *Current Biology*, *11*(23), R986-R996.

Marder, E., & Calabrese, R. L. (1996). Principles of rhythmic motor pattern generation. *Physiological Reviews*, *76*(3), 687-717.

Marder, E., & Prinz, A. A. (2002). Modeling stability in neuron and network function: the role of activity in homeostasis. *Bioessays*, *24*(12), 1145-1154.

Masino, M. A., & Calabrese, R. L. (2002). Period differences between segmental oscillators produce intersegmental phase differences in the leech heartbeat timing network. *Journal of Neurophysiology*, *87*(3), 1603-1615.

Nadim, F., Olsen, y. H., De Schutter, E., & Calabrese, R. L. (1995). Modeling the leech heartbeat elemental oscillator I. Interactions of intrinsic and synaptic currents. *Journal of computational neuroscience*, *2*(3), 215-235.

Olsen, y. H., & Calabrese, R. L. (1996). Activation of intrinsic and synaptic currents in leech heart interneurons by realistic waveforms. *Journal of Neuroscience*, *16*(16), 4958-4970.

Olsen, y. H., Nadim, F., & Calabrese, R. L. (1995). Modeling the leech heartbeat elemental oscillator II. Exploring the parameter space. *Journal of computational neuroscience*, *2*(3), 237-257.

Olypher, A., Cymbalyuk, G., & Calabrese, R. L. (2006). Hybrid systems analysis of the control of burst duration by low-voltage-activated calcium current in leech heart interneurons. *Journal of Neurophysiology*, *96*(6), 2857-2867.

Opdyke, C. A., & Calabrese, R. L. (1994). A persistent sodium current contributes to oscillatory activity in heart interneurons of the medicinal leech. *Journal of Comparative Physiology A: Neuroethology, Sensory, Neural, and Behavioral Physiology*, *175*(6), 781-789.

Osan, R., & Ermentrout, B. (2002). The evolution of synaptically generated waves in one- and two-dimensional domains. *Physica D*, *163*(3), 217-235.

Osan, R., Rubin, J., Curtu, R., & Ermentrout, B. (2003). Traveling waves in a one-dimensional integrate-and-fire neural network with finite support connectivity. *Neurocomputing*, *52-54*, 869-875.

Picton, L. D., Nascimento, F., Broadhead, M. J., Sillar, K. T., & Miles, G. B. (2017). Sodium pumps mediate activity-dependent changes in mammalian motor networks. *Journal of Neuroscience*, *37*(4), 906-921.

Picton, L. D., Zhang, H., & Sillar, K. T. (2017). Sodium pump regulation of locomotor control circuits. *Journal of Neurophysiology*, *118*(2), 1070-1081.

Prinz, A. A., Bucher, D., & Marder, E. (2004). Similar network activity from disparate circuit parameters. *Nature neuroscience*, *7*(12), 1345.

Rybak, I. A., Molkov, Y. I., Jasinski, P. E., Shevtsova, N. A., & Smith, J. C. (2014). Chapter 1 - Rhythmic Bursting in the Pre-Boo}tzinger Complex: Mechanisms and Models. *Progress in Brain Research*, *209*, 1-23.

Rybak, I. A., Shevtsova, N. A., Ptak, K., & McCrimmon, D. R. (2004). Intrinsic bursting activity in the pre-Botzinger complex: role of persistent sodium and potassium currents. *Biological cybernetics*, *90*(1), 59-74.

Rybak, I. A., Shevtsova, N. A., St-John, W. M., Paton, J. F. R., & Pierrefiche, O. (2003). Endogenous rhythm generation in the pre-Botzinger complex and ionic currents: modelling and in vitro studies. *European Journal of Neuroscience*, *18*(2), 239-257.

Schmidt, J., Calabrese, R. L. (1992). Evidence that acetylcholine is an inhibitory transmitter of heart interneurons in the leech. *Journal of Experimental Biology*, *171*(1), 329-347.

Skou, J. C. (1988). Overview: The Na, K-Pump. Methods. *Enzymol.*, *156*, 1-25.

Sorensen, M., Cymbalyuk, G., Calabrese, R., & DeWeerth, S. (2002). Effect of a hyperpolarization-activated inward current on rhythmic activity in a hybrid half-center oscillator. In Ieee, Proceedings of the Second Joint 24th Annual Conference and the Annual Fall Meeting of the Biomedical Engineering Society][Engineering in Medicine and Biology,

Sorensen, M., DeWeerth, S., Cymbalyuk, G., & Calabrese, R. L. (2004). Using a hybrid neural system to reveal regulation of neuronal network activity by an intrinsic current. *Journal of Neuroscience*, *24*(23), 5427-5438.

Tobin, A.-E., & Calabrese, R. L. (2005). Myomodulin increases I h and inhibits the Na/K pump to modulate bursting in leech heart interneurons. *Journal of Neurophysiology*, *94*(6), 3938-3950.

Van Vreeswijk, C., Abbott, L. F., & Ermentrout, G. B. (1994). When inhibition not excitation synchronizes neural firing. *Journal of computational neuroscience*, *1*(4), 313-321.

Wang, X.-J., & Rinzel, J. (1992). Alternating and synchronous rhythms in reciprocally inhibitory model neurons. *Neural Computation*, *4*(1), 84-97.

Weaver, A. L., Roffman, R. C., Norris, B. J., & Calabrese, R. L. (2010). A role for compromise: synaptic inhibition and electrical coupling interact to control phasing in the leech heartbeat CpG. *Front. Behav. Neurosci.*, *4*.

Wenning, A., Cymbalyuk, G. S., & Calabrese, R. L. (2004). Heartbeat control in leeches. I. Constriction pattern and neural modulation of blood pressure in intact animals. *Journal of Neurophysiology*, *91*(1), 382-396.

Wenning, A., Hill, A. A. V., & Calabrese, R. L. (2004). Heartbeat control in leeches. II. Fictive motor pattern. *Journal of Neurophysiology*, *91*(1), 397-409.

Yokoyama, H., Hagio, K., Ogawa, T., & Nakazawa, K. (2017). Motor module activation sequence and topography in the spinal cord during air-stepping in human: Insights into the traveling wave in spinal locomotor circuits. *Physiological Reports*, *5*(22), e13504.

Zhang, H.-Y., Picton, L., Li, W.-C., & Sillar, K. T. (2015). Mechanisms underlying the activity-dependent regulation of locomotor network performance by the Na+ pump. *Scientific reports*, *5*, 16188.

Zhang, H.-Y., & Sillar, K. T. (2012). Short-term memory of motor network performance via activity-dependent potentiation of Na+/K+ pump function. *Current Biology*, *22*(6), 526-531.

2 CONTRIBUTION OF THE NA+/K+ PUMP TO RHYTHMIC BURSTING, EXPLORED WITH MODELING AND HYBRID SYSTEMS ANALYSES

Preface

This chapter is a copy from our published manuscript Erazo-Toscano, R. J., Ellingson, P. J., Calabrese, R. L., & Cymbalyuk, G. S. (2021). Contribution of the Na+/K+ Pump to Rhythmic Bursting, Explored with Modeling and Dynamic Clamp Analyses. JoVE (Journal of Visualized Experiments), (171), e61473. This chapter describes the experimental methods used in chapters 3 and 4.

2.1 Introduction

Heartbeat in leeches is driven by a CPG consisting of 9 bilateral pairs of heart interneurons (HN) distributed across as many mid-body segmental ganglia. At the core of the CPG are mutually inhibitory pairs of interneurons in the 3rd and 4th segmental ganglia that form half-center oscillators (HCOs) (Figure 2) but retain rhythmic bursting when synaptically isolated (pharmacologically bicuculline) (Cymbalyuk et al., 2002b). Others, such as the pair in the 7th segmental ganglia – the focus of our experiments here – are independent bursters receiving only descending input and thus easily isolated by severing the ganglion from the rest of the nerve cord. This independent bursting activity is sensitive to introduced leak current caused by penetration with sharp microelectrodes for recording but vigorously burst when recorded with loose patch methods (Cymbalyuk et al., 2002b). We have previously modeled both individual HN neurons and HN HCOs (H-H based single isopotential compartment models of HN neurons containing all known voltage-gated and synaptic currents) and successfully captured all the burst characteristics of living system (Prinz, Abbott, et al., 2004a). Myomodulin, an endogenous neuropeptide in leeches, markedly decreases period (T) of the burst rhythm of isolated HN

neurons and HN HCOs. This modulator acts to increase h-current (hyperpolarization-activated inward current - I_h) and to decrease I_{pump} (Tobin & Calabrese, 2005b). This observation led us to explore how I_{pump} interacts with I_h, and their co-modulation contributes to rhythmic activity of HN neurons. We found that activation of the pump by increasing $[Na^+]_i$ (using the ionophore monensin) speeds the HN burst rhythm in both HN HCOs and isolated HN neurons (Kueh et al., 2016). We also found that this speed up was dependent on I_h; when I_h was blocked (2mM Cs^+) then the burst period was not altered by this method of pump activation, but the burst duration (BD) was curtailed and the interburst interval (IBI) increased in both HN HCOs and isolated HN neurons (Kueh et al., 2016).

2.2 Protocol

Note: Invertebrate animal experimental subjects are not regulated by the NIH or Emory and Georgia State Universities. All measures are nevertheless taken to minimize suffering of the leeches used in this work.

2.2.1 Prepare isolated Ganglion 7 from the leech nerve cord

Maintain leeches *Hirudo verbana* (Leech.com, https://www.leech.com/collections/live-leeches) in artificial pond water (0.05% (w/v) Instant Ocean sea salt (Spectrum Brands Inc., Madison, WI) diluted in reverse osmosis water at 16^o on a 12:12 light-dark cycle.

Prepare leeches for dissection, by cold anesthetizing in a bed of crushed ice. Fill a black resin lined (Dow Sylgard® 170, Corning, NY) dissecting dish with chilled saline with 115 NaCl, 4 KCl, 1.7 CaCl2, 10 D-glucose, and 10 HEPES (in mM); pH adjusted to 7.4 with 1 M with NaOH.

Pin the leech dorsal side up and make a longitudinal cut through the body wall and expose internal organs. Individual mid-body ganglion 7 (seventh free segmental ganglion caudal to the brain) is removed by severing from the nerve cord after opening the sinus in which the nerve

cord resides, and pin with shortened minuten insect pins, ventral side up, in clear resin (Dow Sylgard® 184, Corning, NY) lined petri dishes.

Remove the perineurium (desheath) the ganglion with microscissors (e.g., Moria® Pascheff-Wolff spring scissors) and or scalpels and superfuse with saline at a flow rate of 50mL/min at room temperature.

2.2.2 Identify and record leech heart interneurons with sharp microelectrodes

Tentatively identify a HN(7) neuron of the bilateral pair by its canonical location at the posteriolateral position in midbody ganglion seven. Penetrate the putative HN(7) neuron with a sharp microelectrode filled with 2 M K Acetate and 20 mM KCl. This process allows one to record membrane potential and pass current with a single microelectrode. Definitively identify the HN(7) neuron by its characteristic spike shape and weak bursting activity (Figure 3C).

Recordings will last between 30 to 60 minutes. Acquire intracellular current and voltage traces sampling at rate of 3KHz using an Axoclamp® 2A amplifier (Molecular Devices, Sunnyvale, CA) in discontinuous current clamp mode and digitize with a Digidata® 1440A (Molecular Devices, Sunnyvale, CA) data acquisition and stimulation system.

2.2.3 Build a real time HN(7)

Custom build software in Simulink® (MathWorks, Natick, MA) using the DS1103 dSPACE® PPC Controller (or modern equivalent board and software) to implement in real time the model currents described in(Hill et al., 2001b; Kueh et al., 2016) or different model currents you wish to implement. Hodgkin-Huxley style equations are the preferred method for representing model currents. See(Barnett & Cymbalyuk, 2011a) for a detailed description of the implementation of our real time model and dynamic clamp prior to the addition of the pump current. We have now

implemented and added the pump current so that **all** the currents of the HN(7) neuron are included as follows:

$$C\frac{\mathrm{d}V}{\mathrm{d}t} = -\left(I_{\mathrm{Na}} + I_{\mathrm{P}} + I_{\mathrm{K1}} + I_{\mathrm{K2}} + I_{\mathrm{KA}} + I_{\mathrm{h}} + I_{\mathrm{CaF}} + I_{\mathrm{CaS}} + I_{\mathrm{Leak}} + I_{\mathrm{pump}}\right) \quad (1)$$

where *C* is the membrane capacitance (in nF), *V* is the membrane potential (in *V*), *t* is time (ins), and the currents are in nA. See (Kueh et al., 2016; Prinz, Abbott, et al., 2004a) for detailed ionic current descriptions and equations. Thus, we have a complete model HN(7) neuron running in real time (Figure 3).

Here the focus of inquiry is the Na^+/K^+ pump (I_{pump}) current and voltage-gated currents contributing significant Na^+ flux: a fast Na^+ current (I_{Na}), a persistent Na^+ current (I_P).

The Na^+/K^+ pump exchanges two extracellular K^+ ions for three intracellular Na^+ ions, it produces a net outward current and exchanges 3 time as much Na^+ as this current indicates. The Na^+/K^+ pump current has a sigmoidal dependence on intracellular Na^+ concentrations, which is expressed as follows:

$$I_{\mathrm{pump}} = \frac{I_{\mathrm{pump}}^{\mathrm{max}}}{1+\exp\left(\frac{[\mathrm{Na}]_{\mathrm{ih}}-[\mathrm{Na}]_{\mathrm{i}}}{[\mathrm{Na}]_{\mathrm{is}}}\right)} \quad (2)$$

where $[Na]_i$ is the intracellular Na^+ concentration, $I_{\mathrm{pump}}^{\mathrm{max}}$ is the maximum Na^+/K^+ pump current, $[Na]_{ih}$ is the intracellular Na^+ concentration for the half-activation of the Na^+/K^+ pump, and $[Na]_{is}$ the sensitivity of the Na^+/K^+ pump to $[Na]_i$. Intracellular Na^+ concentration that occur as a result of the Na^+ fluxes carried by ionic currents and the Na/K pump (Note the contribution of I_h and I_{Leak} to the Na^+ flux is small and not considered in the real-time model.):

$$\frac{\mathrm{d}[Na]_i}{\mathrm{d}t} = -\frac{I_{\mathrm{P}} + I_{\mathrm{Na}} + 3\,I_{\mathrm{pump}}}{\mathrm{vF}} \quad (3)$$

where, v is the volume (~6.7 pL) of the intracellular Na^+ reservoir, F is Faraday's constant, and the extracellular Na^+ concentration is kept constant.

2.2.4 Implement and vary dynamic clamp conductances/currents

Custom build software in Simulink® (MathWorks, Natick, MA) to allow the experimenter to implement and then change in real time dynamic clamp any of the programed conductances/currents of our real-time model of the HN(7) neuron. Our software implements all the conductances/currents in our model HN neuron on a DS1103 dSPACE® PPC Controller Board in real-time at a rate of 20 kHz with a ControlDesk® GUI (dSPACE, Paderborn, Germany)(Barnett & Cymbalyuk, 2011a). Dynamic clamp(Prinz, Abbott, et al., 2004a; Sharp et al., 1993) reads the voltage of the neuron in real time (Figure 2B) and calculates and injects in real time the amount of any current based on model equations and the set values of any $\bar{g}_x$ or I_x^{max}. In particular our GUI has entry boxes that allow changes in the I_{pump}^{max} and $\bar{g}_P$ that we add to the recorded HN(7) neuron with dynamic clamp (Figure 4). You will change these values, as we do during the video demonstration, to affect bursting in the HN(7) neuron. We differentiate between voltage-gated and leak conductances and the pump current which is regulated by calculated intracellular Na^+ concentration ($[Na^+]_i$). $[Na^+]_i$ is built up through Na^+ entry via the fast Na current (I_{Na}) that produces action potentials (spikes) and the persistent Na current (I_P) that provides the depolarization to support spiking. $[Na^+]_i$ is in turn reduced by the action of the pump – extrusion of Na^+.

Microelectrode induced leak will weaken bursting in the recorded HN(7) neuron but adding even small amounts of I_{pump}^{max} and $\bar{g}_P$ with dynamic clamp will stabilize bursting of the HN(7) neuron (Figure 2C). Start your experiments by adding a baseline value of I_{pump} (I_{pump}^{max} = 0.2 nA) - this makes up for the microelectrode induced leak but depresses excitability- and gradually increasing $\bar{g}_P$ - this increases excitability - until regular bursting ensues usually about 4-10 nS (Figure 6).

The experimenter can now co-vary these parameters and assess their effects on burst characteristics: spike frequency (f), interburst interval (IBI), burst duration (BD), burst period (T).

2.3 Representative Results

Modeling with the addition of I_{pump} (Kueh et al., 2016) brought the experimental findings presented in Introduction into sharper focus and began to explain the pump-assisted mechanism of bursting. The real time model demonstrated here has been tuned ($\bar{g}_x$ or I_x^{max} parameters chosen) so that it produces regular rhythmic activity falling within the bounds of normal activity as observed in experiments – spike frequency (f), IBI, BD, T) and continues to produce such activity when the myomodulin-modulated parameters I_{pump}^{max} (the maximal pump current) and $\bar{g}_h$ (maximal h-conductance) are varied or co-varied in the model. Thus, we have parameters values that can be used as a benchmark or canonical set for modeling experiments. In these model instances I_{pump} oscillates throughout the burst cycle as $[Na^+]_i$ oscillates around a baseline level. I_{pump} contributes to burst termination during the burst phase and activates I_h during the IBI - notice its maximal level near burst initiation (Figure 3).

The real-time HN(7) model has all implemented currents(Hill et al., 2001b; Kueh et al., 2016) available for dynamic clamping but here we focus on I_{pump}^{max} and $\bar{g}_P$ which are changeable on the fly in the dynamic clamp GUI (Figure 4). Dynamic clamp allows the experimenter to add or subtract (negative $\bar{g}_x$ or I_x^{max}) any conductance or current into a neuron artificially that mimics the voltage and ionic dependence of a real conductance or current. Thus, one can fully explore how a particular conductance/current interacts with the cells endogenous conductances/currents.

The real time HN(7) model indicates that the persistent Na current (I_P) in HN neurons contributes much of the Na^+ entry determining $[Na^+]_i$ (Figure 3) and thus I_{pump}. Because I_P is

active at relatively negative membrane potentials, it opposes I_{pump} even during the IBI. These observations indicate that it is instructive to explore interactions between I_{pump}^{max} and $\bar{g}_P$ in isolated HN neurons with dynamic clamp (hybrid systems analysis) as in (Calabrese & Prinz, 2009; Olypher et al., 2006b; Sorensen et al., 2004b). These experiments (currently continuing in our lab) are performed with sharp microelectrodes recordings in single synaptically isolated HN(7) neurons (seventh ganglion severed from the nerve cord). Thus far these experiments show that robust bursting is restored in tonically active HN neurons (due to microelectrode penetration introduced leak) by co-addition of I_P and I_{pump} with dynamic clamp (Figure 5). This is an important observation indicating that a bursting mechanism is available in these neurons - even when leak compromised - those results from the interaction of I_{pump} and I_P. Preliminary results indicate a strong complicated space of interaction, which can be explored in model and experiment (Figure 6).

We conclude:

- I_{pump} in response to periodic increases in $[Na^+]_i$ during bursting activity contributes to the burst rhythm through burst termination (decreasing BD).
- Interaction of I_P and I_{pump} constitutes a mechanism which is sufficient to support endogenous bursting activity; this mechanism can reinstate robust bursting in HN interneurons recorded intracellularly in ganglion 7.
- The interaction between I_P and I_{pump} through $[Na^+]_i$ affects HN burst period non-monotonically and ensures robustness of autonomous bursting.

2.4 Discussion

Modeling, dynamic clamp, and the resulting hybrid systems analyses that it enables are useful techniques for exploring how individual and groups of ionic conductance/currents contribute to the electrical activity of neurons. We demonstrated here the use of these techniques to explore how the Na/K pump's current (I_{pump}) interacts with voltage-gated currents, particularly the persistent Na current (I_P) to promote robust bursting in the leech heartbeat pattern generator's core heart interneurons. By adding dynamic clamp experiments to modeling one can test models in way that is not possible with ordinary voltage recording and current clamp techniques. The results gathered in the dynamic clamp experiments (Figure 6) will be used to further refine our model. The basic method of dynamic clamping demonstrated here can be customized to reflect the properties of any neuron under study as long as a mathematic model of neuronal currents can be determined with voltage clamp experiments.

To be successful in implementing experiments of the type shown here requires carfull impalement of a HN or other neuron when using a sharp microelectrode, because strong bursting is curtailed by the electrode penetration(Cymbalyuk et al., 2002b). It is critical that the impalement of the HN neuron cause minimal damage to the neuron (added leak) and input resistance should be monitored and must be in the range of 60 - 100 MOhms for successful experiments (Kueh et al., 2016).

Dynamic clamp is a powerful technique, but it has limitations imposed by neuronal geometry because the artificial conductances are implemented at the site of the recording electrode – usually the cell body – not at the site where rhythm-generating currents are usually localized (Calabrese & Prinz, 2009; Prinz, Abbott, et al., 2004a; Sharp et al., 1993). In leech HN neurons,

the cell body is electrically close to integration zone (main neurite) of the neuron where most active currents are localized, and spikes are initiated.

2.5 Disclosures

None

2.6 Acknowledgements

We thank Christian Erxleben for preliminary dynamic clamp experiments on HN(7) neurons that demonstrated their bursting capabilities. Angela Wenning aided the experiments with expert advice.

2.7 References

Barnett, W., & Cymbalyuk, G. (2011). Hybrid Systems Analysis: Real-Time Systems for Design and Prototyping of Neural Interfaces and Prostheses. *Biohybrid Systems: Nerves, Interfaces, and Machines*, 115–138.

Calabrese, R. L., & Prinz, A. A. (2009). Realistic modeling of small neuronal networks. *Realistic modeling of small neuronal networks*. Cambridge, Mass.: MIT Press.

Cymbalyuk, G. S., Gaudry, Q., Masino, M. A., & Calabrese, R. L. (2002). Bursting in leech heart interneurons: cell-autonomous and network-based mechanisms. *Journal of Neuroscience, 22*, 10580–10592.

Hill, A. A., Lu, J., Masino, M. A., Olsen, O. H., & Calabrese, R. L. (2001). A model of a segmental oscillator in the leech heartbeat neuronal network. *Journal of computational neuroscience, 10*, 281–302.

Kueh, D., Barnett, W. H., Cymbalyuk, G. S., & Calabrese, R. L. (2016). Na+/K+ pump interacts with the h-current to control bursting activity in central pattern generator neurons of leeches. *Elife, 5*, e19322.

Olypher, A., Cymbalyuk, G., & Calabrese, R. L. (2006). Hybrid systems analysis of the control of burst duration by low-voltage-activated calcium current in leech heart interneurons. *Journal of neurophysiology, 96*, 2857–2867.

Picton, L. D., Nascimento, F., Broadhead, M. J., Sillar, K. T., & Miles, G. B. (2017). Sodium pumps mediate activity-dependent changes in mammalian motor networks. *Journal of Neuroscience, 37*, 906–921.

Prinz, A. A., Abbott, L. F., & Marder, E. (2004). The dynamic clamp comes of age. *Trends in neurosciences, 27*, 218–224.

Rybak, I. A., Molkov, Y. I., Jasinski, P. E., Shevtsova, N. A., & Smith, J. C. (2014, January). Chapter 1 - Rhythmic Bursting in the Pre-Botzinger Complex: Mechanisms and Models. *Progress in Brain Research, 209*, 1–23. doi:10.1016/B978-0-444-63274-6.00001-1

Sharp, A. A., O'Neil, M. B., Abbott, L. F., & Marder, E. (1993). Dynamic clamp: computer-generated conductances in real neurons. *Journal of neurophysiology, 69*, 992–995.

Sorensen, M., DeWeerth, S., Cymbalyuk, G., & Calabrese, R. L. (2004). Using a hybrid neural system to reveal regulation of neuronal network activity by an intrinsic current. *Journal of Neuroscience, 24*, 5427–5438.

Tobin, A.-E., & Calabrese, R. L. (2005). Myomodulin increases I h and inhibits the Na/K pump to modulate bursting in leech heart interneurons. *Journal of neurophysiology, 94*, 3938–3950.

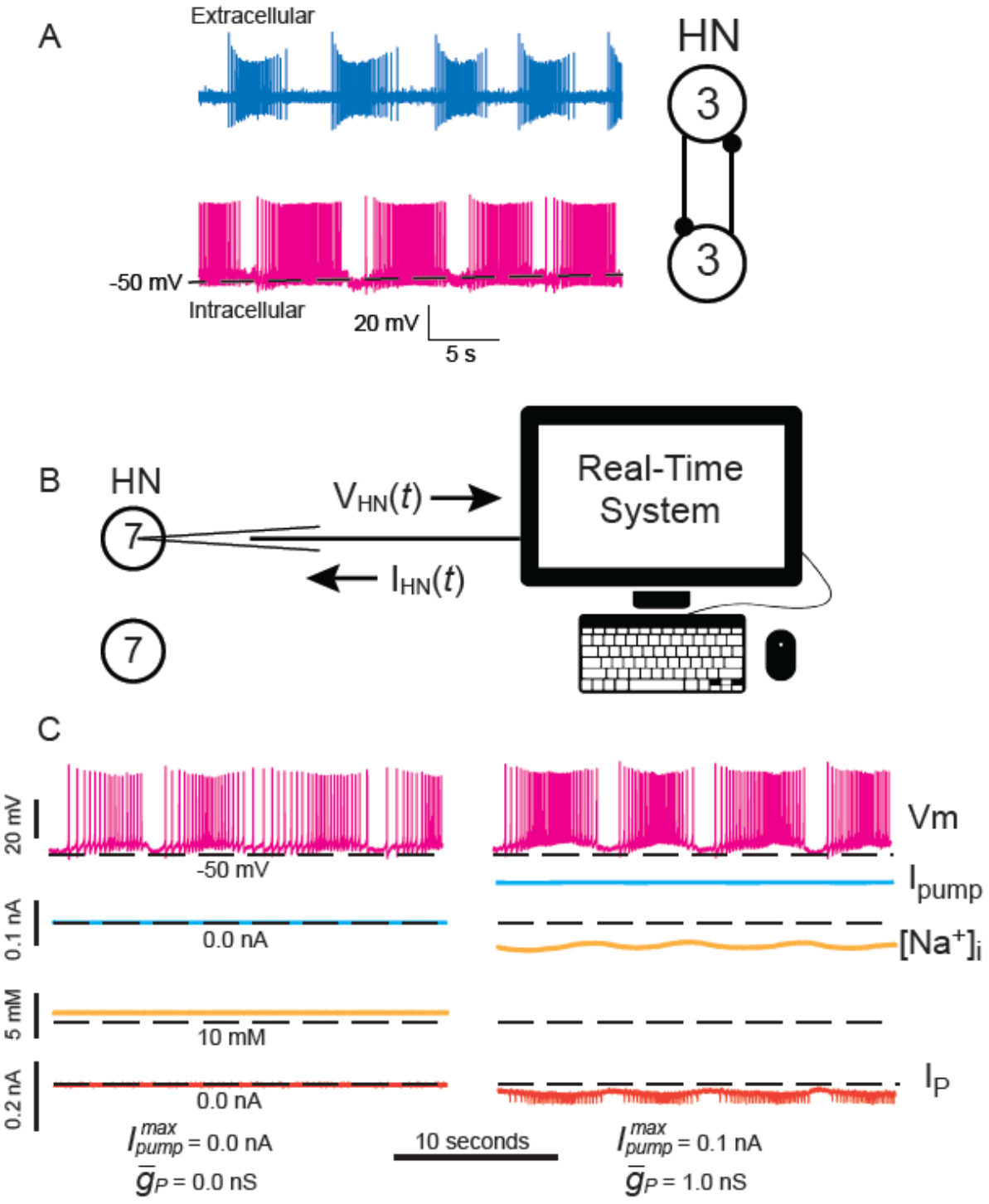
A
Extracellular
HN
3
3
-50 mV
Intracellular
20 mV
5 s
B
HN
7
7
$V_{HN}(t)$
$I_{HN}(t)$
Real-Time System
C
20 mV
-50 mV
Vm
I_{pump}
0.1 nA
0.0 nA
$[Na^+]_i$
5 mM
10 mM
0.2 nA
0.0 nA
I_P
I_{pump}^{max} = 0.0 nA
$\bar{g}_P$ = 0.0 nS
10 seconds
I_{pump}^{max} = 0.1 nA
$\bar{g}_P$ = 1.0 nS

Figure 2. Leech heart interneuron electrical activity and hybrid system implementation with dynamic clamp.

Normal bursting activity recorded extracellularly and intracellulary in a leech heartbeat HCO from a third ganglion (A); schematic of the recorded neurons and their mutually inhibitory synaptic connections at right. Hybrid system schematic when recording a HN(7) interneuron in a isolated ganglion 7; note there is no synaptic interaction between the two HN(7) interneurons (B). Bursting in a leak compromised HN(7) interneuron recommenced by adding a baseline value of I_{pump} (I_{pump}^{max} = 0.2 nA) - this makes up for the microelectrode induced leak but depresses excitability - and $\bar{g}_P$ - this increases excitability - until regular bursting ensues (4 nS) (C). Black dashed lines indicate baseline values.

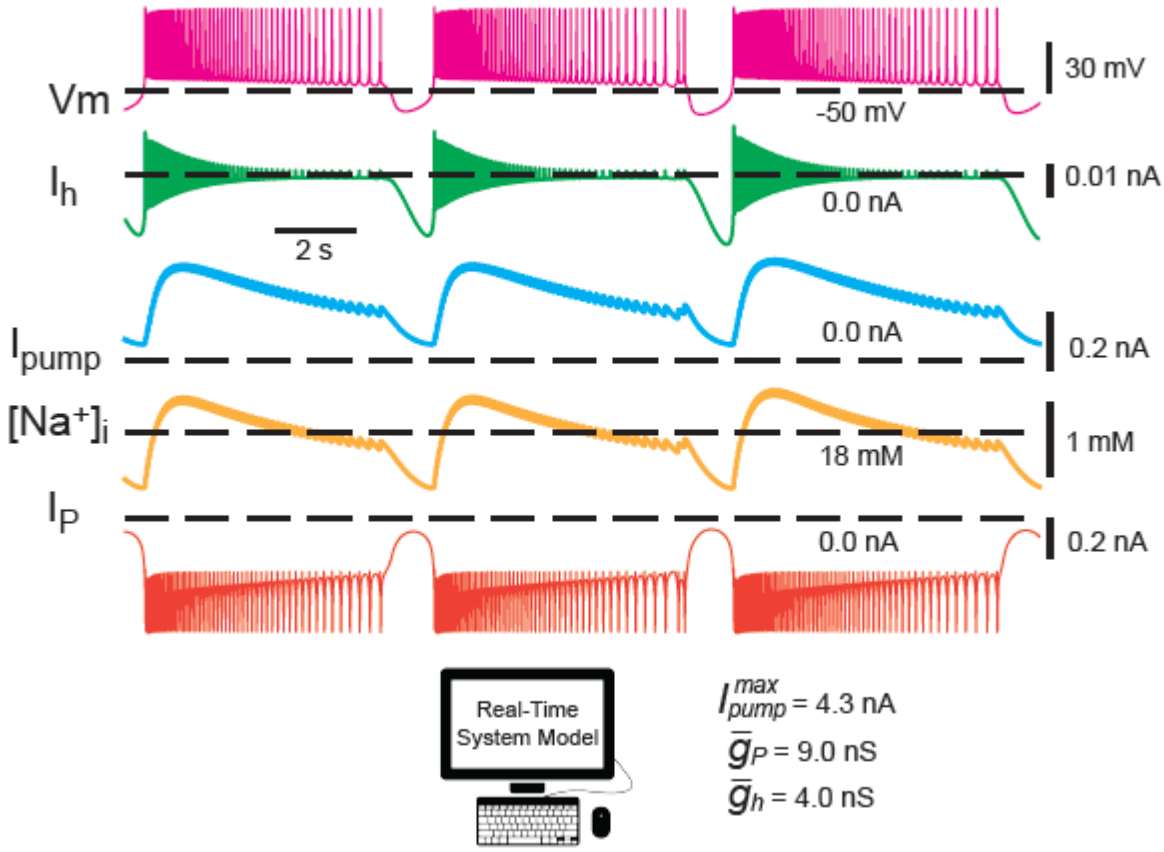

Figure 3. Single cell HN(7) interneuron model showing traces for I_{pump}, $[Na^+]_i$, I_h, and I_P as well as the membrane potential (V_m).

Outward hyperpolarizing currents are negative and inward depolarizing currents are positive. Black dashed lines indicate baseline values.

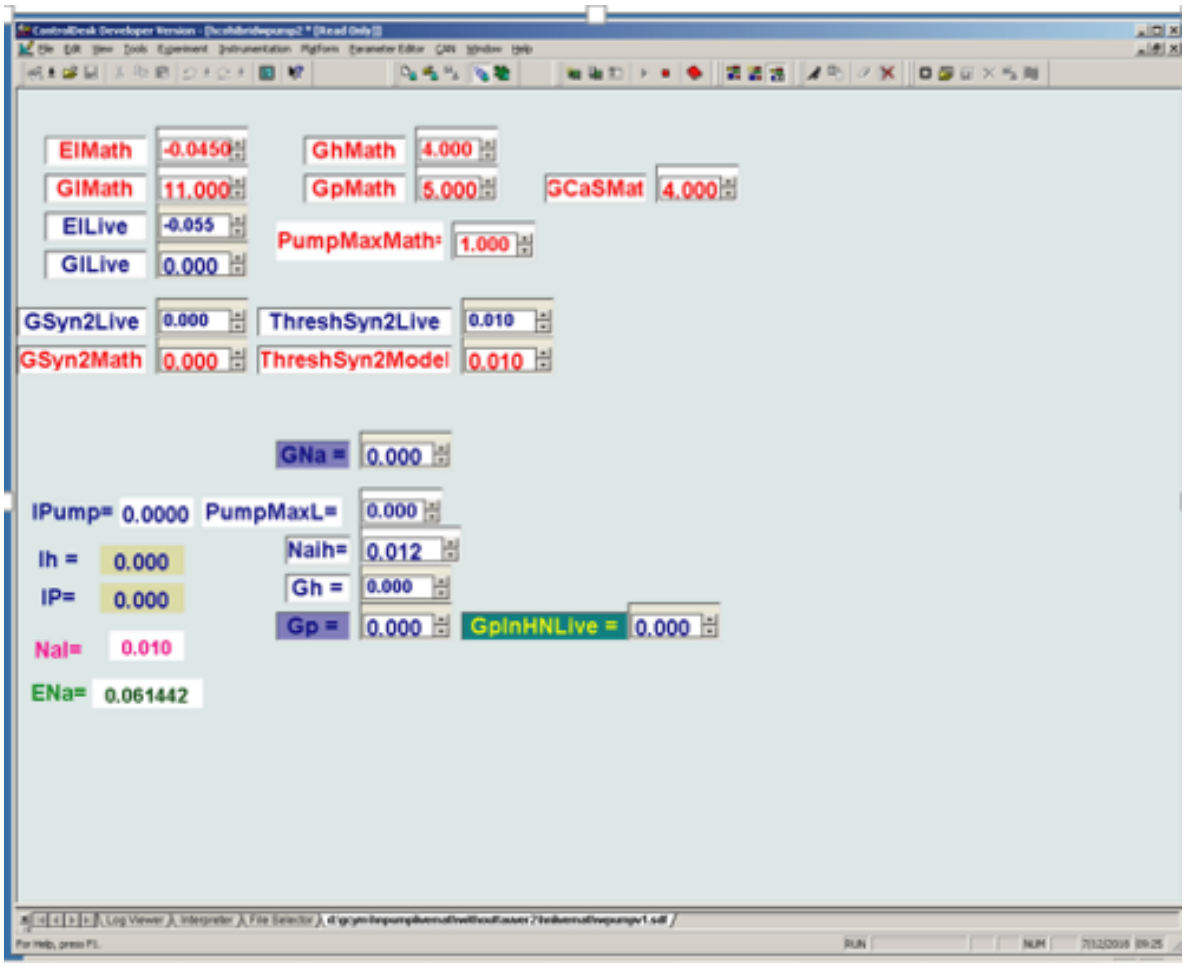

Figure 4. ControlDesk® GUI of real time HN(7) model and Dynamic Clamp implemented in Simulink® on a DS1103 dSPACE® PPC Controller Board.

Upper Left: Red Math are user-determined parameter boxes for the real time model whereas Blue Live are user-determined parameter boxes for the dynamic clamp. El, reversal potential of the leak current; Gl, leak conductance; Gh, h-current maximal conductance; Gp, P current maximal conductance; GCaS, slow calcium current maximal conductance; PumpMax, pump maximal current; [GSyn2 maximal synaptic conductance to the respective neuron; ThreshSyn2 spike crossing threshold for mediating a synaptic potential – these used to make a hybrid half center oscillator and not illustrated here.]. Lower Left for Dynamic Clamp. At the very left are 5 computed values of dynamic clamp variables IPump, pump current injected; Ih, h-current injected (not used here); IP, P-current injected; NaI, calculated internal Na concentration; ENa,

calculated sodium reversal potential. Lower Left for Dynamic Clamp. To the right of the computed variables are 6 user determined parameter boxes; GNa, assumed endogenous fast sodium maximal conductance use to calculate Na^+ flux associated with action potentials; PumMaxL, maximal pump current to be injected by dynamic clamp; Naih see equation (2); Gh, maximal conductance to determine h-current to be injected by dynamic clamp; Gp, assumed endogenous p maximal conductance use to calculate Na^+ flux associated with endogenous p current; GpinHNLive, maximal conductance to determine P-current to be injected by dynamic clamp.

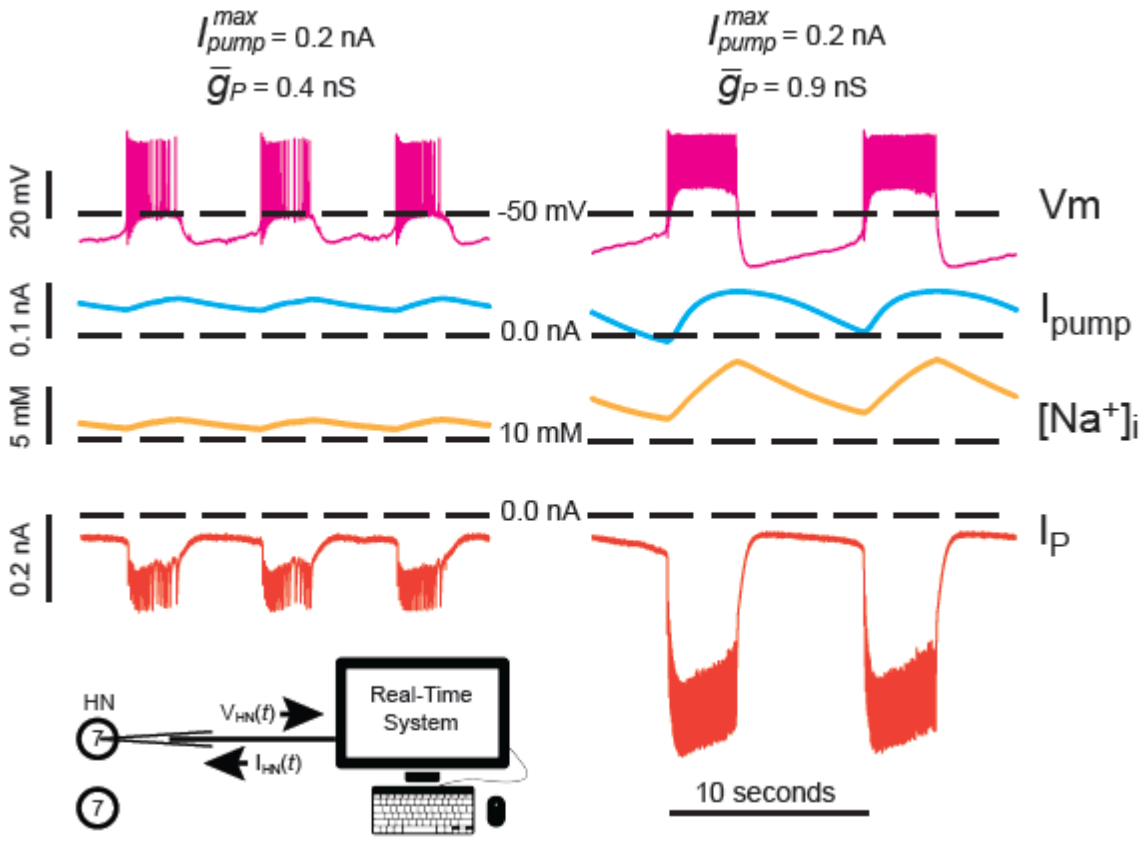

Figure 5. Hybrid systems analysis of independent HN(7) bursting.

Upregulation of $\bar{g}_P$ from 4.0 to 9.0 nS slows down the independent HN burst rhythm. Experimental traces show rhythmic bursting in isolated HN(7) neuron with dynamic clamp. The ranges of oscillation of $[Na^+]_i$ and Vm increase with upregulated $\bar{g}_P$. Traces top to bottom: recorded Vm, injected I_{pump}, calculated $[Na^+]_i$, and injected I_P. Black dashed lines indicate baseline values.

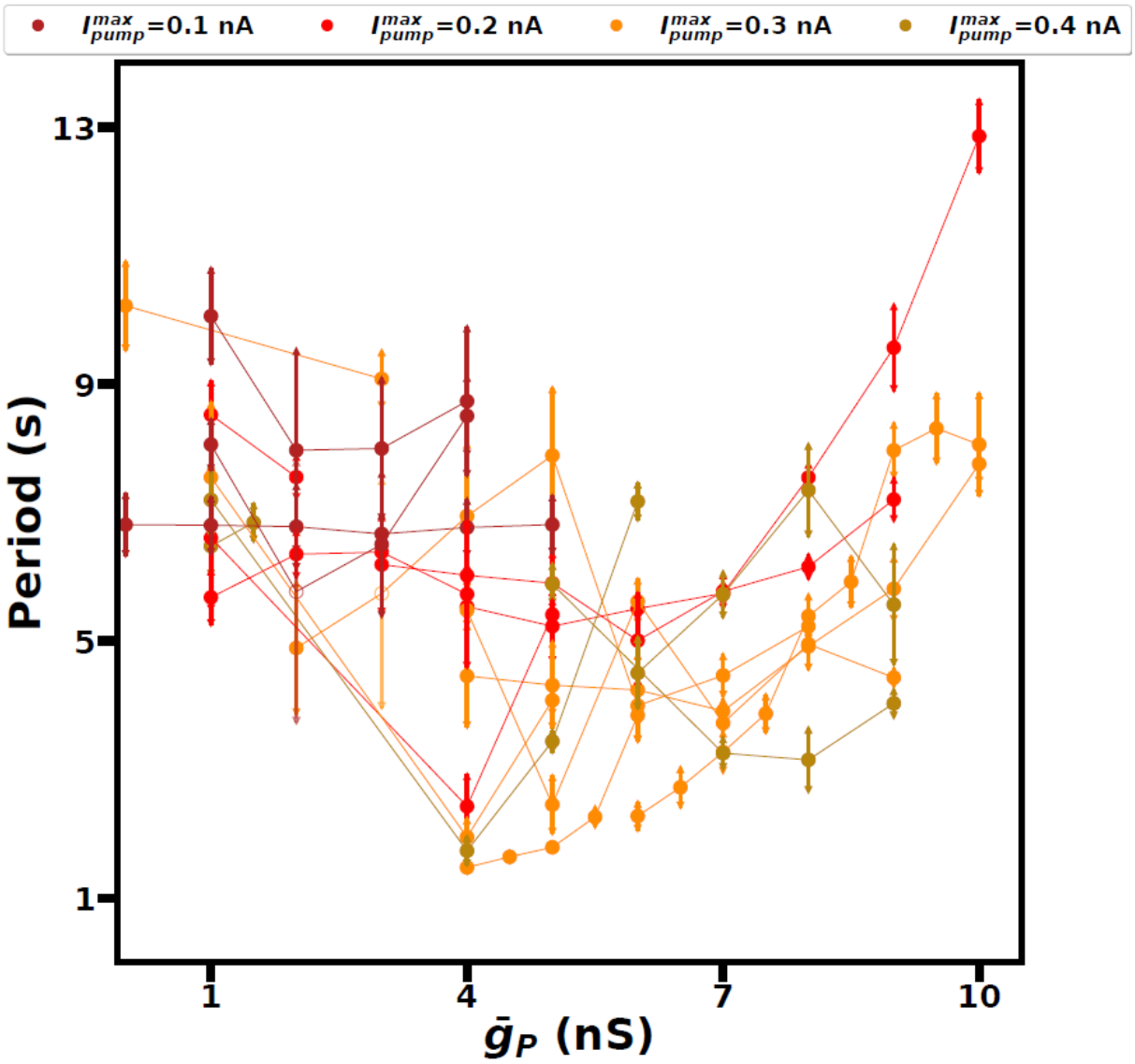

Figure 6. Data analysis of independent HN(7) bursting.

Upregulation of $\bar{g}_P$ tends to decrease, and then increase HN burst period. Colors represent levels of I_{pump}^{max}.

3 ROBUST BURSTING DYNAMICS BASED ON THE INTERACTION OF PERSISTENT NA AND NA/K PUMP CURRENTS: A DYNAMIC CLAMP APPROACH

Preface

This chapter is a preliminary version of our soon-to-be-submitted manuscript to eNeuro: Erazo-Toscano, R. J., Fomenko, M., Core, S., Calabrese, R. L., Cymbalyuk, G. S. Robust Bursting Dynamics Based on the Interaction of Persistent-Na and the Na/K Pump Currents: a Dynamic Clamp Approach. eNeuro (to be submitted).

3.1 Abstract

Life-supporting rhythmic motor functions like the heart-beating in invertebrates and the breathing in vertebrates require an indefatigable generation of a robust rhythm by specialized oscillatory circuits, Central Pattern Generators (CPGs). These CPGs should be sufficiently flexible to adjust to environmental changes and behavioral goals. Continuous self-sustained operation of bursting neurons requires intracellular Na^+ concentration to remain in a functional range and to have checks and balances of the Na^+ fluxes met on the bursting cycle-to-cycle basis. We hypothesize that at a high excitability state, the interaction of the Na^+/K^+ pump current, I_{pump} and persistent Na^+ current, I_P, produces a mechanism supporting functional bursting. I_P is a low voltage-activated inward current that initiates and supports the bursting phase. This current does not inactivate and is a significant source of Na^+ influx. I_{pump} is an outward current activated by $[Na^+]_i$ and is the major source of Na^+ efflux. Both currents are active and counteract each other between and during bursts. We apply a combination of electrophysiology, computational modeling, and dynamic clamp to investigate the role of I_{pump} and I_P in the leech heartbeat CPG interneurons (HN neurons). Applying dynamic clamp to introduce additional I_{pump} and I_P into the dynamics of a living synaptically isolated HN neuron in real-time, we show that their joint upregulation produces transition into a new bursting regime characterized by higher spike frequency and larger amplitude of the membrane potential

oscillations. Further upregulation of I_{pump} speeds up the HN rhythm by shortening burst duration and interburst interval.

3.1.1 Significance statement

Central Pattern Generators (CPGs) are neuronal networks that control rhythmic motor functions such as breathing and walking. Synaptic and membrane properties engage CPG neurons into generating functional bursting patterns; intracellular Na^+ concentration reflects the intensity of the spiking activity during bursts and relegates the Na^+/K^+ pump current for a critical role in sculpting these patterns by providing negative feedback in response to excessive excitation. Here, we show that the dynamic interaction of Na^+/K^+ pump current with persistent Na^+ current offers a mechanism of robust generation and flexible regulation of a robust and flexible pattern of bursting activity. We provide physiological data and present a simple model that explains the underlying dynamics of the oscillatory mechanism.

3.1.2 Keywords

Central Pattern Generator; interneuron; invertebrate; oscillatory networks; electrophysiology; bursting neuron; intracellular Na^+ concentration.

3.2 Introduction

Life-sustaining rhythmic motor behaviors such as breathing are controlled by oscillatory neuronal networks known as central pattern generators (CPGs). The oscillatory patterns in CPGs arise from the interaction of endogenous membrane and synaptic currents (Harris-Warrick, 1993; Marder & Calabrese, 1996; Prinz, Bucher, et al., 2004). CPGs must be flexible and adapt to behavioral goals and environmental conditions by changing the motor output period and frequency (Harris-Warrick & Marder, 1991; Katz, 1996). Many studies have demonstrated that membrane and synaptic properties are subject to neuromodulation that implements changes in the rhythmic patterns. Among these properties, neuromodulators such as myomodulin and dopamine target the activity of the Na^+/K^+ pump (Dobretsov & Stimers,

2005; Kueh et al., 2016; Picton, Nascimento, et al., 2017; Stimers & Dobretsov, 1998; Tobin & Calabrese, 2005a; Wang et al., 2012). The Na^+/K^+ pump sculpts the activity of CPG neurons by generating an outward current reflecting Na^+ entry associated with spiking activity. This feature, taken together with its voltage independence, distinguish the pump current from typical voltage-gated membrane currents (Dobretsov & Stimers, 2005; Parker J. Ellingson et al., 2021; Kueh et al., 2016; Picton, Nascimento, et al., 2017; Sharples et al., 2021). The biophysical mechanisms underlying the contribution of the pump activity in the generation of the neuronal rhythms are not fully understood.

We studied single-cell dynamics in endogenously bursting interneurons (HN neurons) from the leech heartbeat CPG. This CPG is comprised of pairs of HN neurons distributed along ventral nerve cord ganglia. HN neurons in ganglia 3, 4 and 7 have the same voltage- gated currents and behave as endogenous bursters when recorded extracellularly but lose rhythmicity when recorded with sharp microelectrodes (Cymbalyuk et al., 2002a). HN neurons have been well characterized through numerous voltage-clamp studies (Angstadt & Calabrese, 1989, 1991; Kueh et al., 2016; Opdyke & Calabrese, 1994; Simon et al., 1992; Tobin & Calabrese, 2005a), a biophysically accurate single compartment model has been constructed (Parker J. Ellingson et al., 2021; Hill et al., 2001a; Hill et al., 2002; Kueh et al., 2016) and rigorously tested experimentally (Parker J. Ellingson et al., 2021; Erazo-Toscano et al., 2021; Kueh et al., 2016; Olypher et al., 2006a; Sorensen et al., 2002), and special roles of the persistent Na^+ and pump currents identified (Doloc-Mihu & Calabrese, 2014; P. J. Ellingson et al., 2021; Erazo-Toscano et al., 2021; Hill et al., 2001a; Kueh et al., 2016; Opdyke & Calabrese, 1994; Tobin & Calabrese, 2005a), altogether making HN neurons an ideal candidate for studying the mechanisms of rhythmic bursting and the role of the Na^+/K^+ pump.

The persistent Na^+ current (I_P) is a non-inactivating voltage-gated inward current found in HN neurons; I_P supports burst formation and controls spike frequency (Opdyke & Calabrese, 1994).

I_P is a target of neuromodulation by neuropeptide FMRFamide and the rhythmicity of HN neurons is highly sensitive to I_P. For example, low concentrations of FMRFamide speed up the burst rhythm of HN neurons, while high concentrations disrupt neural activity (Nadim & Calabrese, 1997; Schmidt et al., 1995; Simon et al., 1992). I_P must be balanced by an outward current such as non-inactivating K^+ current , leak current (Doloc-Mihu & Calabrese, 2014) (e.g., the HN persistent K^+ current (I_{K2}): see Methods), or I_{pump}. However, the dynamics that arise from the interaction between I_P and either I_{K2} or I_{pump} are fundamentally different because I_{K2} represents a typical conductance-based voltage-activated current while I_{pump} is a voltage-independent Na^+-activated current.

Computational modeling and real-time hybrid systems such as the dynamic clamp are essential tools to unravel neuronal dynamics. We implemented a dynamic clamp to inject I_P and I_{pump} into an HN neuron based on a published computational model (Barnett & Cymbalyuk, 2011b; Cymbalyuk et al., 2002a; Parker J. Ellingson et al., 2021; Erazo-Toscano et al., 2021; Hill et al., 2001a; Hill et al., 2002; Kueh et al., 2016; Olypher et al., 2006a). Our methods allow us to investigate how the interaction of these two ionic currents affects the rhythmic activity of isolated HN neurons. Our experiments with the HN neurons revealed a new bursting regime distinguished by a large amplitude of voltage oscillations and high spike frequency (HVA bursting), elicited by the interaction of I_P and I_{pump}. We determined that upregulating I_{pump} simultaneously decreased burst duration and interburst interval of this bursting regime. We have developed a reduced computational model that explains the mechanism underlying the speeding up of the neuronal rhythm. We demonstrate that the interaction of I_P and I_{pump} creates a flexible and robust oscillatory mechanism that supports the HVA bursting.

3.3 Experimental methods

3.3.1 Animals, solutions, and preparation

Leeches *Hirudo verbana* (https://www.leech.com/collections/live-leeches) were kept in artificial pond water (0.05% w/v Instant Ocean Sea (Spectrum Brands Inc., Madison, WI) diluted in de-ionized water) at 16 ^{o}C on a 12:12 light-dark cycle. Before each dissection, the animals were immobilized by burying them in a bed of crushed ice. For the dissection, the animal was immersed in a dissecting dish filled with chilled leech saline containing 115 mM NaCl, 4 mM KCl, 1.7 mM $CaCl_2$, 10 mM D-glucose, and 10 mM HEPES in de-ionized water; pH adjusted to 7.4 with 1 M NaOH. The animals were pinned dorsal side up, and a longitudinal incision cut to expose the internal organs. Individual mid-body ganglia 7 were removed from the animal and pinned ventral side up in a 35 mm sylgard-coated (Sylgard, Dow Corning, Midland, MI) Petri dish and covered with saline. Directly before the experiment, the glial sheath was removed from the ganglion with microscissors and a scalpel. The preparation was superfused continuously with leech saline (bath volume about 0.5 ml, flow rate about 100 ml/min). All experiments were performed at room temperature (21 – 22 ^{o}C).

3.3.2 Electrophysiology

Electrodes were pulled on a Flaming/Brown micropipette puller (P-97, Sutter Instruments; http://www.sutter.com) from borosilicate glass (1 mm OD, 0.75 mm ID; A-M Systems; http://www.a-msystems.com). The glass electrodes were filled with 2 M KAcetate and 20 mM KCl; we performed quality control to select only electrodes with a resistance higher than $30\ \mathrm{M\Omega}$. All intracellular traces were acquired at a sampling rate larger than 3 kHz using an Axoclamp 2A amplifier (Molecular Devices; www.moleculardevices.com) in discontinuous current-clamp mode. Intracellular signals were digitized with an Axon Digidata 1440A digitizer (5 kHz acquisition rate) and recorded with the Clampex 10.4 software (Molecular Devices).

3.3.3 Dynamic clamp

HN neurons have been extensively studied using voltage clamp, and the following currents were described: a fast Na^+ current (I_{NaF}), a persistent Na^+ current (I_P) (Opdyke & Calabrese, 1994), a hyperpolarization-activated inward current (I_h) (Angstadt & Calabrese, 1989), and three K+ currents (Simon et al., 1992)- delayed rectifier-like K^+ current (I_{K1}), a persistent K^+ current (I_{K2}), and a fast transient K^+ current (I_{KA}). For each of these currents model, Hodgkin-Huxley style equations have been developed (Parker J. Ellingson et al., 2021; Erazo-Toscano et al., 2021; Hill et al., 2001a; Hill et al., 2002; Kueh et al., 2016). A pump current has also been isolated in voltage clamp (Tobin & Calabrese, 2005a), characterized, and model equations developed (Kueh et al., 2016). The dynamic clamp is implemented in Matlab and Simulink (Mathworks, Natick, MA) on dSpace real-time digital signal processing boards: the DS1104 R&D, and the DS1103 PPC (dSPACE Inc.) (Barnett & Cymbalyuk, 2011b; Olypher et al., 2006a). The dynamic clamp system executed the model HN persistent Na^+ current (I_P) and the model HN Na^+/K^+ pump current (I_{pump}) equations so that these currents can be added to or subtracted from the recorded neuron. The dynamic clamp implementation of these currents has been described previously (Barnett & Cymbalyuk, 2011b; Erazo-Toscano et al., 2021). Briefly, the dynamic clamp reads the membrane potential of the neuron and updates the current injected according to model equations evaluated in real-time ($> 3\ kHz$). The dynamic clamp also calculates the cell's native fast Na^+ current (spike-generating current) (I_{NaF}), native persistent Na^+ current, ($I_{P\ native}$), and native pump current, ($I_{pump\ native}$) along with the injected I_P and I_{pump} to estimate the intracellular Na^+ concentration ($[Na^+]_i$) using Equation 1.

Equation 1

$$\frac{d[Na^+]_i}{dt} = -\frac{I_P + I_{P\ native} + I_{NaF} + 3I_{pump} + 3I_{pump\ native}}{vF}$$

where vF (vF = 0.0024 nl*C/Mol) is the volume ($\approx 4.4\ \rho l$) of the cytosolic Na+ reservoir multiplied by the Faraday constant (96485 C /Mol). The extracellular Na^+ concentration ($[Na^+]_o$) is assumed to be constant. In the dynamic clamp model, we simplified the evaluation of Na^+ dynamics and did not include Na^+ fluxes generated by the leak and h-currents (compare to Equation 4) in consideration.

The calculated intracellular $[Na^+]_i$ is used to compute the injected I_{pump} and to evaluate native pump current:

Equation 2

$$I_{pump} = \frac{I_{max}^{pump}}{1 + e^{\left(\frac{[Na^+]_{ih} - [Na^+]_i}{[Na^+]_{is}}\right)}}$$

where I_{max}^{pump}, $[Na^+]_{ih}$, $[Na^+]_{is}$ determine the maximal value, the intracellular Na^+ concentration for half-activation, and the sensitivity of the Na^+/K^+ pump current to $[Na^+]_I$, respectively. On the other hand, the injected I_P depends on the recorded HN neuron's membrane potential and evaluated $[Na^+]_i$, governing Na^+ reversal potential. In our dynamic-clamp experiments, the I_{pump} and I_P were controlled by I_{max}^{pump} and $\bar{g}_P$, respectively; and where noted, we estimated the native currents $I_{P\text{-naitve}}$ ($\bar{g}_{P-native}$ = 5 nS) and $I_{pump\text{-native}}$ ($I_{max-native}^{pump}$= 0.1 nA) which were assumed to be endogenously present in HN neurons. The the model equations and parameters used in dynamic clamp are provided in supplementary data.

3.3.4 Data analysis of experimental burst characteristics

We computed the experimental burst characteristics using previously described methods (Masino & Calabrese, 2002b). We detected spikes in the membrane potential traces with a Matlab function identifying the peaks and selecting those with the height larger than 20 mV. First, we computed the interspike intervals (ISIs) and the ISIs larger than 800 ms were discriminated as the interburst intervals (IBIs). The burst duration (BD) was the time between

the first and last spikes of the burst (Figure 7), where a burst was defined as a group of five or more spikes. A group with a smaller number of spikes would be discarded and its time interval would be concatenated with the two large ISIs, surrounding this small group, into a single interburst interval. The interburst interval (IBI) was the time between the last spike of a burst and the first spike potential of the subsequent burst (Figure 7). IBI was assigned their preceding burst. The cycle period (T) was defined as the time difference between the median spikes of two subsequent bursts (Figure 7) and was assigned to the first of the two bursts.

We characterized a multi-scale, spiking-silence waveform of a bursting cycle by a basic envelope of the membrane potential oscillation with the depolarized and hyperpolarized phases. For the depolarized phase, we averaged membrane potential (V_m) over the time interval between the consecutive minima bounding each spike and assigned the obtained value for every point within this interval. Between bursts, V_m was harvested as is, without averaging. We used the envelope of bursting cycle to compare membrane potential waveforms obtained for different parameter sets and to compare with the simple oscillatory waveform of the two-dimensional model (Figure 7D).

We computed the amplitudes of the averaged membrane potential, $[Na^+]_i$, and I_{pump} oscillations of the bursting envelope applying the same method: we detected the peaks and troughs of the signal, then subtracted the trough values from the peak values in a pairwise fashion. We also computed the median $[Na^+]_i$ and I_{pump}, as the median value of the signal between peaks and troughs of the $[Na^+]_i$ and I_{pump}, respectively; thus, the median was computed for the backside of the waveform (from maximum to minimum), only. We reported the averaged median across recorded cycles of oscillations.

In summary, we gathered the following characteristics of bursting activity: burst duration (BD), interburst interval (IBI), amplitude of the voltage envelope, instantaneous spike frequency, $[Na^+]_i$ envelope amplitude, median $[Na^+]_i$, I_{pump} envelope amplitude, and median I_{pump}. We performed

normalization by dividing the dependent variables (DV) of interest (BD, IBI, $[Na^+]_i$ and I_{pump} amplitude values, $[Na^+]_i$ and I_{pump} median values) by the value of the corresponding DV at $I_{max}^{pump} = 0.3\ nA, \bar{g}_P = 6\ nS$. These reference values of the parameters were chosen since this combination consistently supported regular rhythmic bursting.

3.3.5 Machine Learning algorithms

We implemented a two-threshold algorithm to discriminate between low and high amplitude membrane potential and $[Na^+]_i$ oscillations in the dynamic clamp experimental data (Figure 7 D1 and D2). Expert assisted in discriminating the two regimes with the two-threshold algorithm on 35% of the experimental data by choosing the thresholds. As a result, the algorithm classified the neuron sample activity with '1' if the membrane potential amplitude and $[Na^+]_i$ amplitude were larger than 20 mV and 1 mM, respectively, and '0' otherwise. The output of the two-threshold algorithm was used to train a Gaussian Naïve-Bayes supervised machine learning (ML) algorithm, which then was applied to classify the remaining 65% of the data. Details about the ML algorithm can be found in the scikit-learn documentation (https://scikit-learn.org/stable/modules/naive_bayes.html).

We performed linear regression analyses between the amplitude of voltage bursting envelope (voltage amplitude) and $[Na^+]_i$ envelope amplitude and between the voltage amplitude and spike frequency; the regression analyses were performed in two complementary ways. First, we computed collinearity in an experiment-by-experiment fashion. Second, we computed collinearity on the pooled data.

3.3.6 Estimated Na^+ influx and efflux carried by native and injected currents

We estimated the native $I_{pump\text{-}native}$ and $I_{P\text{-}native}$ based on the canonical HN model (Parker J. Ellingson et al., 2021; Erazo-Toscano et al., 2021; Kueh et al., 2016), with the assumed native parameter values $\bar{g}_{P-native}$= 5 nS, $I_{max}^{pump-native}$= 0.1 nA, $\bar{g}_{NaF}$= 150 nS. We converted each

current to flux by dividing the current in by zF, where z is the valence of the ion of Na^+ (z= 1), and F is Faraday's constant (96485 C mol^{-1}). Each current flux is presented in mol s^{-1}. The total flux carried by each Na^+ current was computed for each period of the rhythmic pattern from the electrophysiological data, and subsequently averaged.

3.3.7 Simplified HN neuron model

We propose that the interaction between I_P and I_{pump} can explain the dynamical mechanism underlying the phenomena we observed experimentally and have developed a simplified version of the HN model focused on this interaction in the canonical HN model (P. J. Ellingson et al., 2021; Erazo-Toscano et al., 2021; Hill et al., 2001a; Hill et al., 2002; Kueh et al., 2016). It has two state variables: membrane potential, V_m, and intracellular Na^+ concentration, $[Na^+]_i$. The membrane potential variable governs four voltage-gated currents with instantaneous activation/inactivation: persistent sodium current with the two components ($I_{P\ native}, I_P$), fast sodium current (I_{NaF}), hyperpolarization-activated current (I_h), and non-inactivating potassium current (I_{K2}). The intracellular Na^+ concentration variable governs the pump current (I_{pump}) and modulates Na^+ currents through the changes in Na^+ reversal potential. Leak and hyperonization-activated currents were split into K^+ and Na^+ components ($I_{leak\text{-}K}$ and $I_{leak\text{-}Na}$ and $I_{h\text{-}K}$ and $I_{h\text{-}Na}$). This model adopted the same parameter values of the two injected currents I_P and two I_{pump} used in experiments. The equations of the simplified model are as follows:

Equation 3

$$\frac{d[Na^+]_i}{dt} = -\frac{I_{P\ native} + I_P\ + 3I_{pump} + I_{NaF} + I_{h-Na} + I_{leak-Na}}{vF}$$

In contrast to the dynamic clamp, in the 2D model, the evaluation of Na^+ dynamics includes native Na^+ currents in addition to dynamic clamp currents. The individual voltage-gated currents were computed with instantaneous activation and inactivation gating variables:

$$I_i = \bar{g}_i \cdot m_{\infty i}^{a_i}(V_m) \cdot h_{\infty i}^{b_i}(V_m) \cdot (V_m - E_i)$$

where $\bar{g}_i$ and E_i are the maximal conductance and reversal potential, respectively, with the subscript *'i'* identifying the type of the current (Table 1). The reversal potential for Na^+ currents E_{Na} was computed using the Nernst equation: $E_{Na} = \frac{RT}{zF} ln \frac{[Na^+]_o}{[Na^+]_i}$, where $[Na^+]_o$ is constant.

The voltage-gated activation and inactivation are instantaneous and denoted as the steady-state functions $m_{\infty i}(V_m)$ and $h_{\infty i}(V_m)$, respectively (Table 3). I_{pump} is determined by Eq. 2 with parameters from Table 2. $I_{leak\text{-}K}$ and $I_{leak\text{-}Na}$ are Ohmic currents (parameters in Table 2), determined by equation:

$$I_{leak-i} = g_{leak-i} \cdot (V_m - E_i)$$

Table 1. Cell constants and current parameters: maximal conductance $\bar{g}_i$, activation exponential a_i, inactivation exponential b_i, and reversal potential E_i

Cell constants	
C_m	0.25 nF
volume	0.0038 nl
$[Na]_o$	0.115 M

Current parameters				
Current	$\bar{g}_i$ (nS)	a_i	b_i	E_i (V)
$I_{P-native}$	9.85	1	0	E_{Na}
I_P	6	1	0	E_{Na}
I_{NaF}	150	3	1	E_{Na}
I_h	6	2	0	-0.021
I_{K2}	138	2	0	-0.07

Table 2. Parameters for special currents I_{leak} and I_{pump}

	$\bar{g}_{leak}$ (nS)	E_i (V)	
$I_{leak-Na}$	1.1	E_{Na}	
I_{leak-K}	8.8	-0.07	
	I_{max}^{pump} (nA)	$[Na^+]_{is}$ (M)	$[Na^+]_{ih}$ (M)
I_{pump}	Range [0.2 0.9]	0.0016	0.012

Table 3. Equations for computing steady-state activation $m_{\infty i}(V)$ and inactivation $h_{\infty i}$ (V)

Current: variable	Steady-state activation or inactivation functions
$I_{P-native}: m_{\infty}(V_m)$	$\frac{1}{1+e^{-160\cdot(V+0.0376)}}$
$I_P: m_{\infty}(V_m)$	$\frac{1}{1+e^{-120\cdot(V+0.04)}}$
$I_{NaF}: m_{\infty}(V_m)$	$\frac{1}{1+e^{-210\cdot(V+0.032)}}$
$I_{NaF}: h_{\infty}(V_m)$	$\frac{1}{1+e^{500\cdot(V+0.04)}}$
$I_h: m_{\infty}(V_m)$	$\frac{1}{1+2\cdot e^{184.14\cdot(V+0.057)}+e^{511.5\cdot(V+0.057)}}$
$I_{K2}: m_{\infty}(V_m)$	$\frac{1}{1+e^{-83\cdot(V+0.0285)}}$

3.3.8 Data analysis of the 2D model

The 2D oscillator interneuron model produces a simple oscillatory voltage waveform similar to the experimental membrane potential envelope waveform. To divide the cycle period into the phases corresponding to the bursting waveform, we set a threshold at -45 mV and considered the depolarized and hyperpolarized phases as corresponding to the burst and silent phases, respectively. Thus, in the 2D model simulation oscillations, BD is the time the simulated voltage is above the threshold, and the IBI is the time when it is below the threshold. To compute the simulation amplitudes of voltage and $[Na^+]_i$ amplitudes we subtracted the troughs from the peaks of the signal.

3.3.9 Optimization of the simplified HN model

We used an evolutionary algorithm to find a 2D model parameter set that fits envelop waveforms and temporal characteristics of bursting activity of an experimental set of used values of I_{max}^{pump}. The evolutionary algorithm optimized the parameters of native currents representing given recorded living neuron: maximal conductance of native I_h – $\bar{g}_h$, the voltage of ½ activation ($V_{½}$) of I_h, conductances of K^+ and Na^+ components of leak current, $g_{leak\text{-}K}$ and $g_{leak\text{-}Na}$, respectively, maximal conductance, steepness of activation, and voltage of half-activation of the native persistent Na^+ current, and the maximal conductance of persistent K^+ current – $\bar{g}_{K2}$. The algorithm kept the dynamic-clamp current (injected I_P and I_{pump}) parameters intact. To assess the quality of the model fitness, we introduced a cost function that took into account the differences in temporal characteristics and deviations in maxima and minima of membrane potential and $[Na^+]_i$ waveforms between the experimental and model activities.

Equation 4

$$F_{cost}$$

$$= \sum \left[\left(BD_{exp} - BD_{sim}\right)^2 + \left(IBI_{exp} - IBI_{sim}\right)^2 \right.$$

$$+ \frac{\left(V\ peak_{exp} - V\ peak_{sim}\right)^2 + \left(V\ trough_{exp} - V\ trough_{sim}\right)^2}{2}$$

$$\left. + \frac{\left([Na^+]_i\ peak_{exp} - [Na^+]_i\ peak_{sim}\right)^2 + \left([Na^+]_i\ \ trough_{exp} - [Na^+]_i\ \ trough_{sim}\right)^2}{2} \right]$$

The evolutionary algorithm generated a population of an 'f' number of parameter sets randomly generated around initial canonical set. We also refer to these parameter sets as individuals. The outcome of the cost function evaluated all individuals, and the parameter set with the smallest value of the function was passed on to create the next generation. At the next generation, a population of individuals was created by adding small noise (2.5% of the parameter value) to each optimization parameter of the passed individual (Ashlock, 2006; Eiben, 2015). The algorithm iterated the process for ‘n’ number of generations. We optimized the following targeted parameters: $g_{leak\text{-}Na}$, $g_{leak\text{-}K}$, $\bar{g}_h$, $\bar{g}_{NaF}$, native $\bar{g}_P$, the voltage of half-activation of native $I_{P\text{-}native}$, steepness of activation of native $I_{P\text{-}native}$, $\bar{g}_{K2}$ and the voltage of half-activation of I_{K2}. These parameters represented cell to cell variability between preparations. The cost function incorporated the outcome of the experimental protocol and kept the experimental values of the parameters $\bar{g}_P$ and I_{max}^{pump} the same while varying only the targeted parameters.

3.4 Results

We investigated dynamics emerging from the interaction between I_P and I_{pump} in isolated leech heart interneurons (HNs). We focused on the HN(7) interneurons because, it is essential for this study that in the seventh ganglion the two HNs do not have mutual synaptic connections and are thus isolated as soon as this ganglion is extracted. Thus, this preparation allows us to readily investigate single-cell dynamics without pharmacological intervention (Calabrese, 1977).

We introduced the two currents with the dynamic clamp, varied their parameters: $\bar{g}_P$ and I_{max}^{pump}, and investigated patterns of spiking activity. We used two protocols: 1), we kept I_{max}^{pump} constant (0.1 nA n=7, 0.2 nA n=6, 0.3 nA n=3, 0.5 nA n=3) and systematically varied $\bar{g}_P$ in a random order ($\bar{g}_P$ range from 1.0 to 7.0 nS); 2), we kept $\bar{g}_P$ constant (4 nS n=4, 5 nS n=5, 6 nS n=18, 7 nS n=3) and systematically varied I_{max}^{pump} in random order (I_{max}^{pump} range from 0.1 to 0.9 nA).

3.4.1 Injection of small I_P and I_{pump} reinstates bursting in HN neurons

The dynamics of a single HN are very sensitive to the shunting leak current introduced by sharp microelectrodes. The isolated HN interneurons exhibit bursting activity if recorded extracellularly with a loose whole-cell patch pipette and tonic spiking activity if recorded intracellularly with a sharp microelectrode (Cymbalyuk et al., 2002a). We found that we could reinstate bursting activity in HN neurons with sharp microelectrodes by introducing a relatively small currents I_P ($\bar{g}_P$= 1 nS) and I_{pump} (I_{max}^{pump}= 0.1 nA) using dynamic clamp. The reestablished bursting activity has properties typical for HN bursting: low voltage envelope amplitude underlying the slow membrane potential oscillations and the spike frequency similar to that obtained in extracellular recordings (Figure 1A) (Kueh et al., 2016; Tobin & Calabrese, 2005a). Below, we call this regime the Low Voltage Amplitude (LVA) bursting regime. Thus, dynamic-clamp currents, I_P and I_{pump}, support rhythmic bursting of HN neurons undeterred by the nonspecific leak current introduced by a sharp microelectrode (Cymbalyuk et al., 2002a) (Figure 7A).

3.4.2 The combination of I_{max}^{pump} and $\bar{g}_P$ distinguishes two bursting regimes exhibited by hybrid HN neurons

Using the first dynamic clamp protocol, we systematically increased $\bar{g}_P$ while keeping I_{max}^{pump} at a constant value (Figure 7A-C). When we increased $\bar{g}_P$ from 1.0 to 3.0 nS, the burst duration and interburst interval became irregular (Figure 1B, coefficient of variation = 0.38). When we further increased $\bar{g}_P$ to 6 nS the bursting activity became regular again and its waveform changed: the spike frequency and amplitude of the underlying envelope oscillations of V_m and $[Na^+]_i$ became

visibly high (Figure 7 C, D). These observations suggested the emergence of a new bursting regime as a result of the variation of I_{max}^{pump} and $\bar{g}_P$. Below, we call this regime the High Voltage Amplitude (HVA) bursting.

We systematically varied dynamic-clamp parameters, I_{max}^{pump} and $\bar{g}_P$, to test whether these two bursting regimes are quantitatively distinct. We found that the LVA bursting possesses the following properties, the amplitude of membrane potential envelope had mean=4.1 mV, SD=2.15 mV (n=15), spike frequency had mean=4.1 Hz, SD=1.4 Hz (n=15), and estimated amplitude of $[Na^+]_i$ oscillation was relatively low with mean=0.42 mM, SD=0.14 mM (n=15) (Figure 7A, Figure 8A). The other regime, the HVA bursting has high amplitude of envelope of membrane potential with mean=44.8 mV, SD=1.16 mV (n=22), high spike frequency with mean=17.11 Hz, SD=0.9 Hz (n=22), and high amplitude of $[Na^+]_i$ oscillation with mean=2 mM, SD=0.13 mM (n=22) (Figure 7C, Figure 8A). For control conditions in HN(7) neurons, the average spike frequency in the literature is 11.4 ± 2.2 Hz (Cymbalyuk et al., 2002a).

In all experiments, a sufficiently large increase of $\bar{g}_P$ caused the transition from the LVA to HVA bursting (Figure 8). We also observed intermediate states exhibiting mixed bursts with low and high-spike frequencies that resemble both HVA and LVA bursting (Figure 7B, Figure 8A $\bar{g}_P$ = 4 nS, black traces), which we discarded from further analysis because of the high variability of the period (coefficient of variation ≥0.27). In HVA bursting, I_P augmented the depolarization phase of the neuron, facilitated $[Na^+]_i$ influx, and supported increased spike frequency (Figure 8A). The strong positive correlation between voltage envelope and $[Na^+]_i$ oscillation amplitudes demonstrate that membrane potential depolarization and $[Na^+]_i$ influx grow together (experiment-by-experiment averaged r=0.98, p<0.01, pooled data r=0.766, p<0.001, n=22, Figure 8 B). The voltage amplitude and the spike frequency are also strongly positively correlated (experiment-by-experiment averaged r=0.96, p≤0.01, pooled data r=0.83, p<0.001, n=22, Figure 8C). The scatterplots (Figure 8 B and C) indicate the differences in the voltage

amplitude, the sodium concentration amplitude, and the spike frequency between the LVA and HVA bursting regimes. We used a two-threshold algorithm to classify our data and train a machine learning classification algorithm (Methods). We mapped the LVA and HVA bursting regimes distinguished by the classification algorithm on the parameter plane ($\bar{g}_P, I_{max}^{pump}$) (Figure 8D). While the LVA bursting clusters at the bottom left corner of the scatterplots, the HVA rhythm spreads out on the upper area of the plots (Figure 8 B and C).

In the HVA regime, we detected a critical effect: the high membrane potential during bursting and high-spike frequency increases the Na^+ influx. Contrasting LVA (Figure 9A) versus HVA (Figure 9B), the spiking activity within HVA bursts generates $[Na^+]_i$ influx higher than in LVA (Figure 9); for example, in the LVA rhythm, the average Na^+ influx from injected I_P at $\bar{g}_P$= 2.0 nS was ≈70 mM/s and from the estimated I_{NaF} was ≈11 mM/s (Figure 9C). In contrast, in the HVA rhythm, the average Na^+ influx from injected I_P at $\bar{g}_P$= 6.0 nS was ≈150 mM/s and from the estimated I_{NaF} was ≈50 mM/s (Figure 9C). In the LVA regime (with $\bar{g}_P$= 2.0 nS), the ratio of Na^+ influx from I_P and I_{NaF} was ≈7:1. In contrast, in the HVA regime (with $\bar{g}_P$= 6.0 nS), this ratio of Na^+ influx was ≈3:1. We increased $\bar{g}_P$ by a factor of 3 (from 2 to 6 nS), and the estimated Na^+ influx from I_P raised by a factor of ≈2 while from I_e by a factor of ≈5. Thus, spike frequency and voltage amplitude played a crucial role in controlling the relative contribution of I_{NaF} to the [Na+]i dynamics. The higher level of $[Na^+]_i$ more strongly activated I_{pump}; thus stronger outward current terminates earlier the burst and then stronger hyperpolarizes the cell. I_P drives the depolarization during the burst enhancing Na^+ influx, which interacts with I_{pump} creating a robust oscillatory mechanism.

A two-parameter map of $\bar{g}_P$ and I_{max}^{pump} shows that $\bar{g}_P$ determines the switch between LVA and the HVA bursting (Figure 8D). LVA and HVA bursting are segregated to different areas where $\bar{g}_P$ is lower (LVA) or higher (HVA); because of animal-to-animal variability, there is also an intersection area where both regimes were found.

3.4.3 In the HVA bursting, increase of I_{max}^{pump} decreases HN burst duration and interburst interval

The Na^+/K^+ pump current is voltage-independent and can be activated during and between bursts. Because the Na^+/K^+ pump current can thus regulate neuronal activity throughout the burst cycle, it potentially affects both BD and IBI. The Na^+/K^+ pump current is activated by increased $[Na^+]_i$. In both the LVA and HVA bursting regimes, $[Na^+]_i$ increases during bursts, but in the HVA, the $[Na^+]_i$ reaches higher values due to the increased joint contribution of injected I_P and estimated I_{NaF} (Figure 9). Then, the Na^+/K^+ pump remains active after the burst termination throughout the IBI. The interaction between I_{pump} and I_P controls the IBI by providing mutual feedback. The $[Na^+]_i$-dependence of the Na^+/K^+ pump enables it to respond to an increase in $[Na^+]_i$ and to terminate bursts (Figure 10, the peaks of the oscillations of I_{pump} coincide with the last spike of the burst). When $[Na^+]_i$ declines, the I_{pump} decreases, permitting I_P to depolarize the membrane potential and initiate a new cycle (Figure 10). The troughs of the oscillations of I_{pump} coincide with the first spike of each burst. In the HVA regime, upregulation I_{max}^{pump} speeds up the period of HN neurons (Figure 10, Figure 11 A and B).

Since the parameter I_{max}^{pump} describes the maximal output of the I_{pump} but does not affect the pump's sensitivity or concentration of half-activation of I_{pump}, I_{max}^{pump} determines $[Na^+]_i$ and I_{pump}. Namely, an increase of I_{max}^{pump} from 0.3 nA to 0.7 nA decreased the median $[Na^+]_i$ by 18% and the $[Na^+]_i$ amplitude by 27% (Figure 10, Figure 11 C and D), and increased the amplitude of oscillations of I_{pump} by 27% (Figure 11F) while not changing the median I_{pump} (Figure 11E).

3.4.4 Simple HN neuron model explains how I_{max}^{pump} controls burst duration and interburst interval

We investigated the oscillatory properties of the interaction of I_P and I_{pump} in a simple model with two dynamic variables, membrane potential-V_m and intracellular Na^+ concentration-$[Na^+]_i$. We curve-fitted this 2D model to match experimental data (Methods). Our simulations emulate

experiments following the protocol 2 (Methods): we kept all parameters constant, including conductance of injected I_P, $\bar{g}_P$= 6 nS, while systematically varied I_{max}^{pump} from 0.2 nA to 0.9 nA. The 2D model has a sub-set of currents (I_h, $I_{P\text{-native}}$, I_{K2}, I_{NaF}, $I_{leak\text{-}K}$ and $I_{leak\text{-}Na}$ components) incorporated as steady-state currents with their kinetics taken from the canonical model. They are incorporated to represent cell-to-cell variability in experiments. An injected persistent sodium current (I_P) and the injected Na^+/K^+ pump current (I_{pump}) have the same parameters as in experiments. The optimization algorithm simultaneously matched the waveforms of the experimental voltage envelope and $[Na^+]_i$, BD, and IBI with their simulated counterparts. Figure 12 shows an example of a model optimized to one representative experiment, including eight values of I_{max}^{pump}. The simulated BD and IBI follow the same trend of the dependence on I_{max}^{pump} as observed experimentally and are within range of experimentally observed characteristics (relative error: BD=0.10, IBI=0.09) (Figure 12A1-A2).

To relate the 2D model dynamics to experimental data, we outlined its phase portrait. We considered a phase plane of the two phase variables ($[Na^+]_i$, V_m), representing possible states of the model by the phase points with the coordinates determined by the two variables. We plotted its oscillatory trajectory projected along with the envelopes of experimentally obtained bursting waveforms (Figure 12B1-B3 and C1-C3). The oscillatory motion of the 2D model on the phase plane is governed by the equations 3 and 4 describing dependence of the speed of change of the phase variables V_m and $[Na^+]_I$, respectively, on the position of the system on the plane. We plotted the nullclines of the system and, thus, determined borders between domains on the plane where the corresponding variables change the sign of their speed, e.g. reverse directions of motion, since by definition a nullcline of a phase variable is a set of points on the phase plane where the derivative of the variable is zero. The intersection(s) between nullclines defines the stationary steady state(s) of the 2D system. The V_m-nullcline marks the model's states at which the inward currents are in precise balance with outward currents and, thus, the total current is

zero (Equation 3). Consequently, below the V_m-nullcline, the derivative of V_m is positive and V_m increases, while above the V_m-nullcline, the derivative of V_m is negative, and V_m decreases (repolarizes) (Figure 12B2). The V_m-nullcline has a z-shape, and with the described directions of the speed of V_m , the upper and lower branches of z-shaped nullcline attract the trajectories (stable branches) and the middle one, connecting these branches at the knee points, repels the trajectories, acting as a threshold between depolarized and hyperpolarized states or phases of the neuron. Similarly, the $[Na^+]_i$ -nullcline marks the neuron's states at which the inward Na^+ fluxes are in precise balance with outward Na^+ fluxes and the total Na^+ flux is zero (Equation 4). On the left side of the $[Na^+]_i$ -nullcline, the speed of $[Na^+]_i$ is positive and $[Na^+]_i$ increases, and on the right side of this nullcline, the speed reverses the sign and $[Na^+]_i$ decreases. The membrane potential V_m changes much faster than the intracellular Na^+ concentration, since the factors determining time scales of the equations are more than three orders of magnitude different, C_m<< vF. Thus, trajectories are almost immediately jump either to the upper or lower branch of the z-shaped V_m-nullcline, reaching a state close to the balance of the inward and outward currents without notable change in the intracellular Na^+ concentration and the phase point representing the model's state will be almost always located in a vicinity of these stable branches. If the $[Na^+]_i$-nullcline intersected V_m – nullcline at the middle unstable branch, the intersection point is an unstable stationary state. After reaching one of the V_m – nullcline's branches, the trajectory will evolve so, that the $[Na^+]_I$ will slowly change according to the sign of the speed, staying in the close vicinity to the V_m-nullcline. These dynamics produces a closed periodic orbit (limit cycle) on the phase plane (Figure 12 B1-B3) and synchronous oscillations of V_m and $[Na^+]_I$ versus time (Figure 12C1-C3).

The limit cycle comprises four sections: two slow and two fast. The slow sections follow the upper and lower branches of the z-shaped V_m-nullcline: the upper slow section of the orbit represents the depolarized, spiking phase and the lower slow section represents

hyperpolarized, quiescent phase of the bursting cycle. In contrast, the fast sections represent the rapid transitions between spiking and silent phases roughly at the knee points serving as the thresholds for these transitions (Figure 12B2, C2). Thus, these knee points of the z-shaped V_m -nullcline determine the range and thus amplitude of the oscillations of $[Na^+]_i$. The durations of the depolarized (BD) and hyperpolarized (IBI) phases are similarly determined by the $[Na^+]_i$ amplitude and separately determined by the speed of $[Na^+]_i$ along the corresponding upper and lower branches of the V_m-nullcline. Consideration of these two factors explains the dependence of the BD and IBI on I_{max}^{pump} .

We investigated how the phase portrait evolved along with the changes of I_{max}^{pump} from 0.2 nA to 0.9 nA (Figure 12 B1-B3). The range of the oscillations of $[Na^+]_i$ shortens with the increase of I_{max}^{pump} as the nullclines shift to the left along the $[Na^+]_I$ axis and the distance between the knee points shrinks (Figure 12B1-B3, Table 4). The parameter I_{max}^{pump} scales the sigmoidal activation curve of the Na^+/K^+ pump and with the larger factor the pump current would reach the same range at the smaller corresponding values and more narrow range of $[Na^+]_i$ (Figure 13A1-A2). As we increased I_{max}^{pump} from 0.3 to 0.9 nA, the activation curves became steeper while the median $[Na^+]_i$ and $[Na^+]_i$ amplitude decreased; Figure 13A1 and A2 show the activation curves for three levels of I_{max}^{pump}. The vertical and horizontal projections delimit the minimum and maximum I_{pump} and $[Na^+]_i$, respectively, and facilitate visual comparison between I_{max}^{pump} 0.3, 0.6 and 0.9 nA. This is consistent with the above analysis (Figure 11C-F), where we obtained that increasing I_{max}^{pump} decreases the $[Na^+]_i$ median and amplitude, while the amplitude of I_{pump} increases, and the median of I_{pump} remains unchanged. Altogether these analyses demonstrate that increasing I_{max}^{pump} produces a more significant I_{pump} while $[Na^+]_i$ decreases more rapidly, which compresses and shifts the $[Na^+]_i$ oscillations. This scaling effect explains the compression and the shift of the knee-points V_m-nullcline toward smaller intracellular Na^+ concentration

(Figure 13C,D). This factor predicts simultaneous shortening of the BD and IBI with the same rate relative to the increase of I_{max}^{pump}.

The second factor describes how the speed $\frac{d[Na^+]_i}{dt}$ along the slow sections of the limit cycle with the increase of I_{max}^{pump}. These changes are caused by the change of the magnitude of the total Na^+ flux (equation 4) and could be different for the depolarized and hyperpolarized phases of the cycle. More depolarized membrane potential supports higher Na^+ influx through the fast Na^+ and persistent Na^+ currents. Notably, the fast Na^+ current is fully deactivated at the hyperpolarized membrane potentials. Along with the above described compression (Figure 13) the hyperpolarized section of the cycle expands towards more hyperpolarized membrane potential where the persistent Na^+ current is further diminished by deactivation, produces smaller Na^+ influx and thus could suggest steeper dependence of the change of speed $\frac{d[Na^+]_i}{dt}$ on I_{max}^{pump} at the hyperpolarized section (Figure 13D).

We evaluated relative contributions of the second factor on BDs and IBIs by considering the slow motion of the phase point between the knee points along with the depolarized and hyperpolarized branches of the V_m-nullcline, respectively, with the speed $\frac{d[Na^+]_i}{dt}$. The speed changes along the branches and, for our approximations, we evaluated it at 200 points (100 points per branch section) distributed with equal intervals in terms of $[Na^+]_i$ between the knee points (vertical dashed lines), using equation 4 (Figure 13 C,D). The computed average speeds for these two sections over these points show that with the increase of I_{max}^{pump}, the average speed over the hyperpolarized section increased with the higher rate than over the depolarized one (Table 4). This factor predicts that IBI would shorten faster than BD relative to the increase of I_{max}^{pump}.

Table 4. Relative changes in the amplitude of the oscillations of $[Na^+]_i$ and the speed $\frac{d[Na^+]_i}{dt}$ during the burst and during interburst interval along with the increase of I_{max}^{pump}

I_{max}^{pump} (nA)	δ $[Na^+]_i$ amplitude	δ $\frac{d[Na^+]_i}{dt}$ Burst	δ $\frac{d[Na^+]_i}{dt}$ IB-Interval
0.2	1	1	1
0.3	0.63456	1.0455	1.1615
0.4	0.53326	1.068	1.2439
0.5	0.4881	1.082	1.3013
0.6	0.46322	1.0918	1.3458
0.8	0.43753	1.1053	1.414
0.9	0.43034	1.1104	1.4415

Approximation of the BD and IBI by the integration of the slow motion along with the slow branches of the V_m -nullcline roughly matches the values obtained from the simulated cycle with the relative errors of 18% (Table 5, Figure 15). With I_{max}^{pump} growing from 0.2 nA to 0.9 nA, the amplitude of oscillations of $[Na^+]_i$ shrinks by 57%, the average speed $\frac{d[Na^+]_i}{dt}$ during the burst increases by roughly 11%, while during the interburst interval it increases by 56% (Table 4, Figure 16). Altogether, the two factors, the dependence of the Na^+ concentration amplitude and speed on I_{max}^{pump}, explain the mechanism underlying the decrease of BD and IBI with the increase of I_{max}^{pump} in the dynamic-clamp experiments. The amplitude of $[Na^+]_i$ is the dominating factor determining the burst duration, while both the $[Na^+]_i$ amplitude and speed determine the interburst interval.

Table 5. Simulated and approximated characteristics bursting (BD and IBI). The estimations were done based on measurements made at 100 points on the depolarized and

hyperpolarized branches of V_m-nullcline between the knee-points. The average relative error between the simulated and approximate measurements were 18%.

I_{max}^{pump} (nA)	Simulated BD (s)	Approximated BD (s)	Simulated IBI (s)	Approximated IBI (s)
0.2	2.26	1.94	3.39	2.92
0.3	1.46	1.21	1.96	1.63
0.4	1.25	1.02	1.57	1.28
0.5	1.15	0.94	1.39	1.13
0.6	1.11	0.90	1.29	1.04
0.8	1.06	0.87	1.17	0.93
0.9	1.06	0.86	1.13	0.90

3.5 Discussion

We studied how the interaction of I_P and I_{pump} pace the rhythmic activity of single-cell oscillator interneurons of the leech heartbeat CPG (HN neurons) using the dynamic clamp technique. I_P and I_{pump} are native currents that are the target of neuromodulation by endogenous neuropeptides in the leech (Parker J. Ellingson et al., 2021; Kueh et al., 2016; Nadim & Calabrese, 1997; Opdyke & Calabrese, 1994; Schmidt et al., 1995; Tobin & Calabrese, 2005a). We showed that small amounts of I_P and I_{pump} introduced with dynamic clamp restore typical bursting of HN neurons (Low-Voltage Amplitude bursting regime); neuronal excitability and ability to repolarize are both compromised by the nonspecific leak current introduced by sharp electrode penetration (Cymbalyuk et al., 2002a) (Figure 7A). In every HN neuron that we studied, we found that co-regulation of I_P and I_{pump}, specifically increasing I_{max}^{pump} to at least 0.1 nA and $\bar{g}_P$ greater than 5.0 nS, gave rise to a new bursting regime, the High Voltage Amplitude

(HVA) bursting mode (Figure 7C, Figure 8). A machine learning classification algorithm confirmed a statistically significant difference between the LVA and the HVA bursting regimes (Figure 8). In addition, we showed that once in the HVA bursting regime, increasing I_{max}^{pump} decreases the burst duration (BD) and the interburst interval (IBI), effectively speeding up the rhythm of the oscillation; this mechanism allows flexible control of the pace of the neuronal bursting (Figure 10 and Figure 11). We understand the underlying dynamics of this bursting by considering the neuron membrane potential, the intracellular sodium concentration ($[Na^+]_i$) and how $[Na^+]_i$ responds to I_P and I_{pump}: I_P supports Na^+ influx and membrane potential depolarization, while I_{pump} governs $[Na^+]_i$ and supports membrane potential repolarization (Figure 9). These currents regulate burst initiation and termination, controlling the cycle period of the burst rhythm (Figure 12). We conclude that I_P and I_{pump} interact to form a robust and flexible oscillatory mechanism.

3.5.1 Small amounts of I_P and I_{pump} support the natural bursting of HN neurons

Invasive recording tools, such as sharp intracellular electrodes, can unintentionally affect measured neuronal activity (Cymbalyuk et al., 2002a; Pusuluri et al., 2021), while allowing manipulation of neuronal activity. Here, we demonstrated that appropriate inward and outward currents injection could compensate the sharp electrode membrane damage. Once again our work shows that the dynamic clamp technique is uniquely valuable for prototyping and experimenting all sorts of brain-machine interface research (Erazo-Toscano et al., 2021; Prinz, Abbott, et al., 2004b).

I_{pump} responds dynamically to $[Na^+]_i$, differentiating it from a steady (or voltage-gated) outward current. Thus, pump activity (as embodied in the parameter I_{max}^{pump}) modulates excitability in HN neurons; increasing pump activity diminishes excitability while decreasing the pump activity enhances excitability. Our experiments demonstrated that excitability must be preserved by mutually counterbalancing currents if bursting is to be maintained. An example illustrating this

principle is modulation by myomodulin, an endogenous leech neuropeptide. Myomodulin reduces the pump's activity and enhances I_h; in synaptically isolated HN neurons, weak bursting rhythms become robust with myomodulin application (Tobin & Calabrese, 2005a). The net effect is that myomodulin supports functional bursting and avoids dysfunctional seizure-like bursting regimes in HN neurons (P. J. Ellingson et al., 2021; Kueh et al., 2016; Tobin & Calabrese, 2005a). In contrast, enhancing only one current can disrupt functional activity in neurons. Ellingson et al., (2021) demonstrated that I_{pump} and I_h co-modulation gave rise to a pathway that supports functional activity. A proportional reduction in I_{pump} accompanied enhancement of I_h produces smooth changes in period.

3.5.2 Enhancing I_P and I_{pump} transitions neurons to an intense bursting mode

HN neurons compose the central pattern generator (CPG) that paces the rhythm of the leech heartbeat. Depending on environmental factors or behavioral goals, the leech heartbeat CPG should be able to adjust the pacing of the heartbeat. Our experiments demonstrate that HN neurons are capable of two bursting regimes differentiated by their level of excitability. In the LVA, excitability is low, and bursts are long with low spike frequency. In contrast, in the HVA, excitability is high, bursts are short with high spike frequency. Because neurons communicate through spikes, the differences in spike frequency between the LVA and HVA bursting regimes suggest these bursting regimes support different functions of neuronal activity.

3.5.3 The Na^+/K^+ pump monitors cellular activity

The Na/K pump is generally recognized as playing a critical role in self-regulating neuronal activity (Brodsky & Guidotti, 1990; Glynn, 1993; Luger, 1991; Skou, 1988), but less often is the underlying $[Na^+]_i$ that it regulates considered as a measure of neuronal activity. Our work estimated underlying fluctuations in $[Na^+]_i$ that accompany rhythm bursting. The amplitude of these fluctuations is determined by burst intensity (burst duration, voltage envelope amplitude, and spike frequency) (Figure 11) and thus serve as a proxy for the intensity of the bursting

regime. Na^+ sensors such as Na^+-dependent K^+ (I_{KNa}) currents could read out this proxy and synergize with the pump as suggested by Hage & Salkoff (2012), I_{KNa} may be involved in providing a large outward conductance common to many types of neurons. Functional co-expression of I_{KN} and persistent-sodium currents was observed at the single-channel level, indicating a specific relationship (Hage & Salkoff, 2012). Further, $[Na^+]_i$ activates the Na^+/K^+ pump, and because the pump activity consumes ATP and oxygen, $[Na^+]_i$ may act in an as yet undescribed homeostatic mechanism. The impact of these $[Na^+]_i$ fluctuations on cellular activity remains unexplored mainly, but our work suggests that it may be a fruitful avenue of future research.

3.5.4 A bursting mechanism afforded by the dynamical $[Na^+]_i$ exchange by I_P and I_{pump}

The 2-D model, which includes the Na^+/K^+ pump and intracellular Na^+ dynamics, captured and explained the changes in each of the two burst characteristics (burst duration, and interburst interval), and two waveform characteristics (voltage envelope and intracellular sodium oscillation amplitudes) within the experimental manipulation of dynamic-clamp I_{max}^{pump}. The 2-D model also confirmed our experimental results showing that increasing I_{max}^{pump} enhances membrane potential repolarization, which interacts with the persistent- Na^+ current to shorten the interburst interval (Figure 11B). Furthermore, the model suggests that when an isolated HN neuron has I_P augmented with the dynamic clamp, the pump current contributes to burst termination and consequently influences the burst duration (Figure 11A). Overall, our model quantitively reproduced the dependence of the burst characteristics on I_{max}^{pump} measured experimentally. Our model shows that one can estimate the burst duration and interburst interval based on the geometry of the nullclines. Thus, our model reveals that the Na^+/K^+ pump current is an essential regulator of neuronal activity.

The 2-D model accurately replicates the bursting characteristics and evolution of the voltage and $[Na^+]_i$ waveforms. Further, the model explains the mechanism that supports control over BD

and IBI observed experimentally and afforded by the interaction of I_P and I_{pump}. I_P and I_{pump} are near balance during the burst and the interburst interval, driving burst initiation and burst termination. The conventional understanding of control over bursting characteristics by conductance-based currents is fundamentally different; for example, activation of outward I_K or inactivation of inward I_{Ca} may terminate a burst, determined by activation/inactivation variables that change over time with a time constant. In contrast, in the mechanism formed by the interaction of I_P and I_{pump}, the two currents are balanced, supporting the burst, and the burst terminates through the saddle-node bifurcation in the slow subsystem. The slow variable in the 2-D model ($[Na^+]_i$) behaves as a relaxation oscillator; showing that $[Na^+]_I$ plays a pivotal role as an intermediary between the inward I_P and the outward I_{pump}; the amplitude grows and decays as HN neurons switch between LVA and HVA bursting regimes. Taking into account sodium concentration allowed us to thoroughly characterize the dynamics governing the burst characteristics in HN neurons.

3.6 References

Angstadt, J. D., & Calabrese, R. L. (1989). A hyperpolarization-activated inward current in heart interneurons of the medicinal leech. *Journal of Neuroscience*, *9*(8), 2846-2857.

Angstadt, J. D., & Calabrese, R. L. (1991). Calcium currents and graded synaptic transmission between heart interneurons of the leech. *Journal of Neuroscience*, *11*(3), 746-759.

Ashlock, D. (2006). *Evolutionary Computation for Modeling and Optimization*. Springer-Verlag GmbH. https://www.ebook.de/de/product/12472033/daniel_ashlock_evolutionary_computation_for_modeling_and_optimization.html

Barnett, W., & Cymbalyuk, G. (2011). Hybrid Systems Analysis: Real-Time Systems for Design and Prototyping of Neural Interfaces and Prostheses. *Biohybrid Systems: Nerves, Interfaces, and Machines*, 115-138.

Brodsky, J. L., & Guidotti, G. (1990). Sodium affinity of brain Na (+)-K (+)-ATPase is dependent on isozyme and environment of the pump. *American Journal of Physiology-Cell Physiology*, *258*(5), C803-C811.

Calabrese, R. L. (1977). The neural control of alternate heartbeat coordination states in the leech, Hirudo medicinalis. *Journal of Comparative Physiology*, *122*(1), 111-143.

Cymbalyuk, G. S., Gaudry, Q., Masino, M. A., & Calabrese, R. L. (2002). Bursting in leech heart interneurons: cell-autonomous and network-based mechanisms. *Journal of Neuroscience*, *22*(24), 10580-10592.

Dobretsov, M., & Stimers, J. R. (2005). Neuronal function and alpha3 isoform of the Na/K-ATPase. *Front Biosci*, *10*, 2373-2396.

Doloc-Mihu, A., & Calabrese, R. L. (2014). Identifying crucial parameter correlations maintaining bursting activity. *PLoS Comput Biol*, *10*(6), e1003678. https://doi.org/10.1371/journal.pcbi.1003678

Eiben, A. (2015). *Introduction to evolutionary computing*. Springer.

Ellingson, P. J., Barnett, W. H., Kueh, D., Vargas, A., Calabrese, R. L., & Cymbalyuk, G. S. (2021). Comodulation of h- and Na$$/K$$ Pump Currents Expands the Range of Functional Bursting in a Central Pattern Generator by Navigating Between Dysfunctional Regimes. *The Journal of Neuroscience*, JN-RM-0158-0121.

Ellingson, P. J., Barnett, W. H., Kueh, D., Vargas, A., Calabrese, R. L., & Cymbalyuk, G. S. (2021). Comodulation of h- and Na(+)/K(+) Pump Currents Expands the Range of Functional Bursting in a Central Pattern Generator by Navigating between Dysfunctional Regimes. *J Neurosci*, *41*(30), 6468-6483. https://doi.org/10.1523/JNEUROSCI.0158-21.2021

Erazo-Toscano, R. J., Ellingson, P. J., Calabrese, R. L., & Cymbalyuk, G. S. (2021). Contribution of the Na/K Pump to Rhythmic Bursting, Explored with Modeling and Dynamic Clamp Analyses. *Journal of Visualized Experiments*(171).

Glynn, I. M. (1993). All hands to the sodium pump (Annual Review Prize Lecture). *J. Physiol*, *462*, 1-30.

Hage, T. A., & Salkoff, L. (2012). Sodium-activated potassium channels are functionally coupled to persistent sodium currents. *Journal of Neuroscience*, *32*(8), 2714-2721.

Harris-Warrick, R. M. (1993). Pattern generation. *Current Opinion in Neurobiology*, *3*(6), 982-988.

Harris-Warrick, R. M., & Marder, E. (1991). Modulation of neural networks for behavior. *Annual review of neuroscience*, *14*(1), 39-57.

Hill, A. A. V., Lu, J., Masino, M. A., Olsen, O. H., & Calabrese, R. L. (2001). A model of a segmental oscillator in the leech heartbeat neuronal network. *Journal of computational neuroscience*, *10*(3), 281-302.

Hill, A. A. V., Masino, M. A., & Calabrese, R. L. (2002). Model of intersegmental coordination in the leech heartbeat neuronal network. *Journal of Neurophysiology*, *87*(3), 1586-1602.

Katz, P. S. (1996). Neurons, networks, and motor behavior. *Neuron*, *16*(2), 245-253.

Kueh, D., Barnett, W. H., Cymbalyuk, G. S., & Calabrese, R. L. (2016). Na+/K+ pump interacts with the h-current to control bursting activity in central pattern generator neurons of leeches. *Elife*, *5*, e19322.

Luger, P. (1991). *Electrogenic ion pumps*.

Marder, E., & Calabrese, R. L. (1996). Principles of rhythmic motor pattern generation. *Physiological Reviews*, *76*(3), 687-717.

Masino, M. A., & Calabrese, R. L. (2002). Phase relationships between segmentally organized oscillators in the leech heartbeat pattern generating network. *Journal of Neurophysiology*, *87*(3), 1572-1585.

Nadim, F., & Calabrese, R. L. (1997). A slow outward current activated by FMRFamide in heart interneurons of the medicinal leech. *Journal of Neuroscience*, *17*(11), 4461-4472.

Olypher, A., Cymbalyuk, G., & Calabrese, R. L. (2006). Hybrid systems analysis of the control of burst duration by low-voltage-activated calcium current in leech heart interneurons. *Journal of Neurophysiology*, *96*(6), 2857-2867.

Opdyke, C. A., & Calabrese, R. L. (1994). A persistent sodium current contributes to oscillatory activity in heart interneurons of the medicinal leech. *Journal of Comparative Physiology A: Neuroethology, Sensory, Neural, and Behavioral Physiology*, *175*(6), 781-789.

Picton, L. D., Nascimento, F., Broadhead, M. J., Sillar, K. T., & Miles, G. B. (2017). Sodium pumps mediate activity-dependent changes in mammalian motor networks. *Journal of Neuroscience*, *37*(4), 906-921.

Prinz, A. A., Abbott, L. F., & Marder, E. (2004). The dynamic clamp comes of age. *Trends in Neurosciences*, *27*(4), 218-224.

Prinz, A. A., Bucher, D., & Marder, E. (2004). Similar network activity from disparate circuit parameters. *Nature neuroscience*, *7*(12), 1345.

Pusuluri, K., Li, Y., Hochman, S., & Prinz, A. A. (2021). Enhanced ensemble computational models of mouse thoracic sympathetic postganglionic neurons with offline compensation of electrode artifacts. Journal of computational neuroscience,

Schmidt, J., Gramoll, S., & Calabrese, R. L. (1995). Segment-specific effects of FMRFamide on membrane properties of heart interneurons in the leech. *Journal of Neurophysiology*, *74*(4), 1485-1497.

Sharples, S. A., Parker, J., Vargas, A., Milla-Cruz, J. J., Lognon, A. P., Cheng, N., Young, L., Shonak, A., Cymbalyuk, G. S., & Whelan, P. J. (2021). Contributions of h- and Na(+)/K(+) Pump Currents to the Generation of Episodic and Continuous Rhythmic Activities. *Front Cell Neurosci*, *15*, 715427. https://doi.org/10.3389/fncel.2021.715427

Simon, T. W., Opdyke, C. A., & Calabrese, R. L. (1992). Modulatory effects of FMRF-NH2 on outward currents and oscillatory activity in heart interneurons of the medicinal leech. *Journal of Neuroscience*, *12*(2), 525-537.

Skou, J. C. (1988). Overview: The Na, K-Pump. Methods. *Enzymol.*, *156*, 1-25.

Sorensen, M., Cymbalyuk, G., Calabrese, R., & DeWeerth, S. (2002). Effect of a hyperpolarization-activated inward current on rhythmic activity in a hybrid half-center oscillator. In Ieee, Proceedings of the Second Joint 24th Annual Conference and the Annual Fall Meeting of the Biomedical Engineering Society][Engineering in Medicine and Biology,

Stimers, J. R., & Dobretsov, M. (1998). Adrenergic stimulation of Na/K pump current in adult rat cardiac myocytes in short-term culture. *The Journal of membrane biology*, *163*(3), 205-216.

Tobin, A.-E., & Calabrese, R. L. (2005). Myomodulin increases I h and inhibits the Na/K pump to modulate bursting in leech heart interneurons. *Journal of Neurophysiology*, *94*(6), 3938-3950.

Wang, Y.-C., Yang, J.-J., & Huang, R.-C. (2012). Intracellular Na+ and metabolic modulation of Na/K pump and excitability in the rat suprachiasmatic nucleus neurons. *Journal of Neurophysiology*, *108*(7), 2024-2032.

3.7 Figures

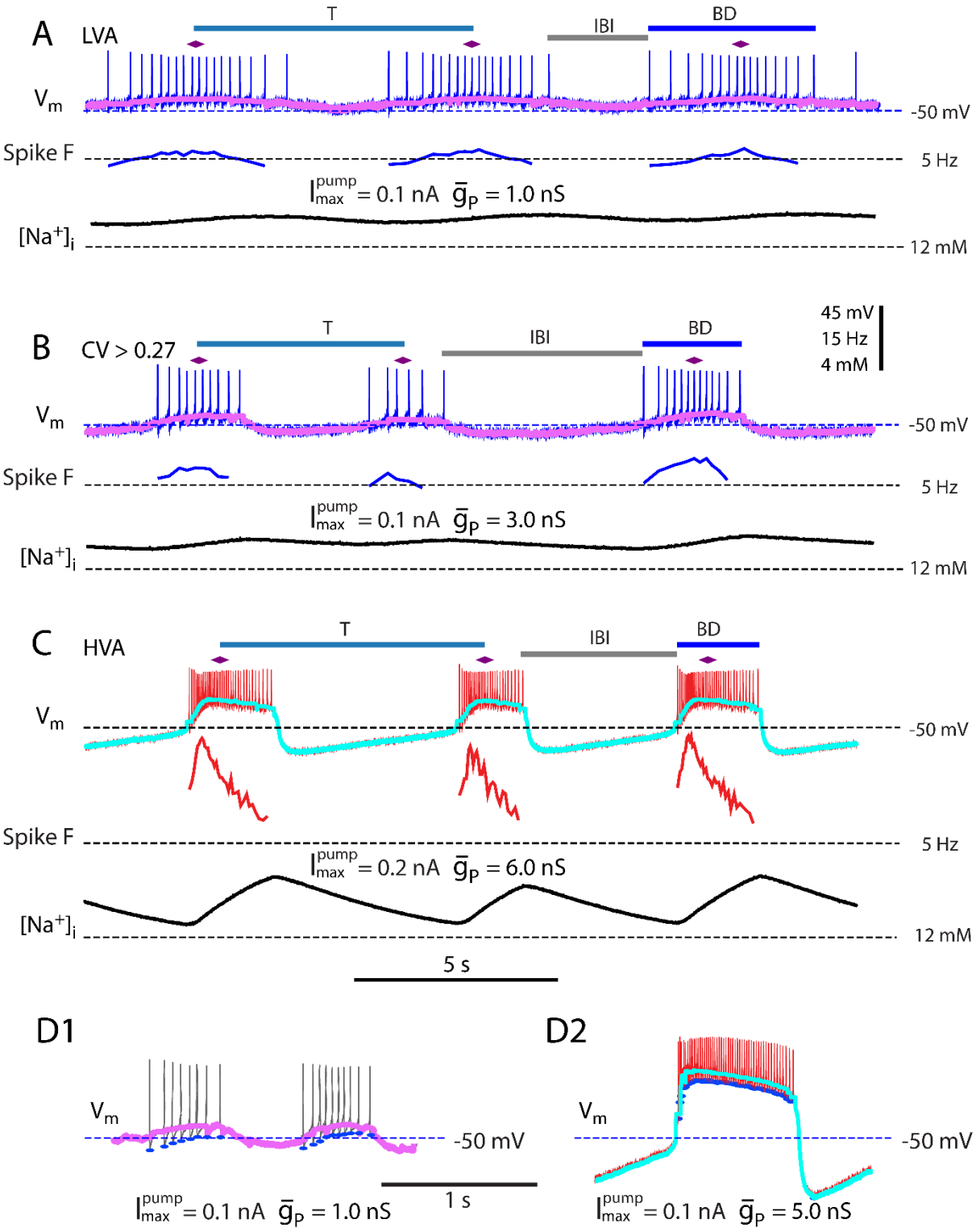
A
LVA
T
IBI
BD
V_m
-50 mV
Spike F
5 Hz
$I_{max}^{pump} = 0.1$ nA $\bar{g}_P = 1.0$ nS
$[Na^+]_i$
12 mM
B
CV > 0.27
45 mV
15 Hz
4 mM
$I_{max}^{pump} = 0.1$ nA $\bar{g}_P = 3.0$ nS
C
HVA
$I_{max}^{pump} = 0.2$ nA $\bar{g}_P = 6.0$ nS
5 s
D1
1 s
$I_{max}^{pump} = 0.1$ nA $\bar{g}_P = 1.0$ nS
D2
$I_{max}^{pump} = 0.1$ nA $\bar{g}_P = 5.0$ nS

Figure 7. Experimental data from a single HN(7) neuron with I_P and I_{pump} introduced by dynamic clamp to support bursting activity

In A, B, and C, membrane potential V_m (mV) top, the instantaneous spike frequency (Hz) (middle), and virtual internal Na^+ concentration ($[Na^+]_i$) (mM) (bottom) estimated by the dynamic clamp model (at the bottom). In this and all subsequent figures $[Na^+]_i$ is calculated using both estimated native (I_{pump}, I_P, and I_{NaF}) and dynamic clamp injected (I_{pump} and I_P) currents. Parameter values for $\bar{g}_P$ and I_{max}^{pump} are those used for dynamic clamp injected currents. The horizontal bars above the membrane potential traces mark the temporal characteristics of the bursting: bursting cycle period (T), the interburst interval (IBI), and the burst duration (BD). The purple diamonds over each burst tag the median spike used to compute the bursting cycle period. The thick colored curves over the voltage traces are the (voltage) envelopes of bursting waveforms (see Methods). In this and subsequent figures, high voltage amplitude (HVA) high spike frequency bursts are shown in red with the corresponding voltage envelope in cyan, and LVA bursts are shown in blue with the corresponding voltage envelope in magenta. A, B, and C are sample data for different dynamic clamp $\bar{g}_P$ and I_{max}^{pump} parameters from the same preparation. A: Coefficient of variation: 0.26, B: Coefficient of variation: 0.38,C: Coefficient of variation: 0.1. D1, D2: Computed voltage envelope with spike minima identified (blue ovals). These are representative bursts, LVA (D1) and HVA (D2) respectively, with different dynamic clamp parameters.

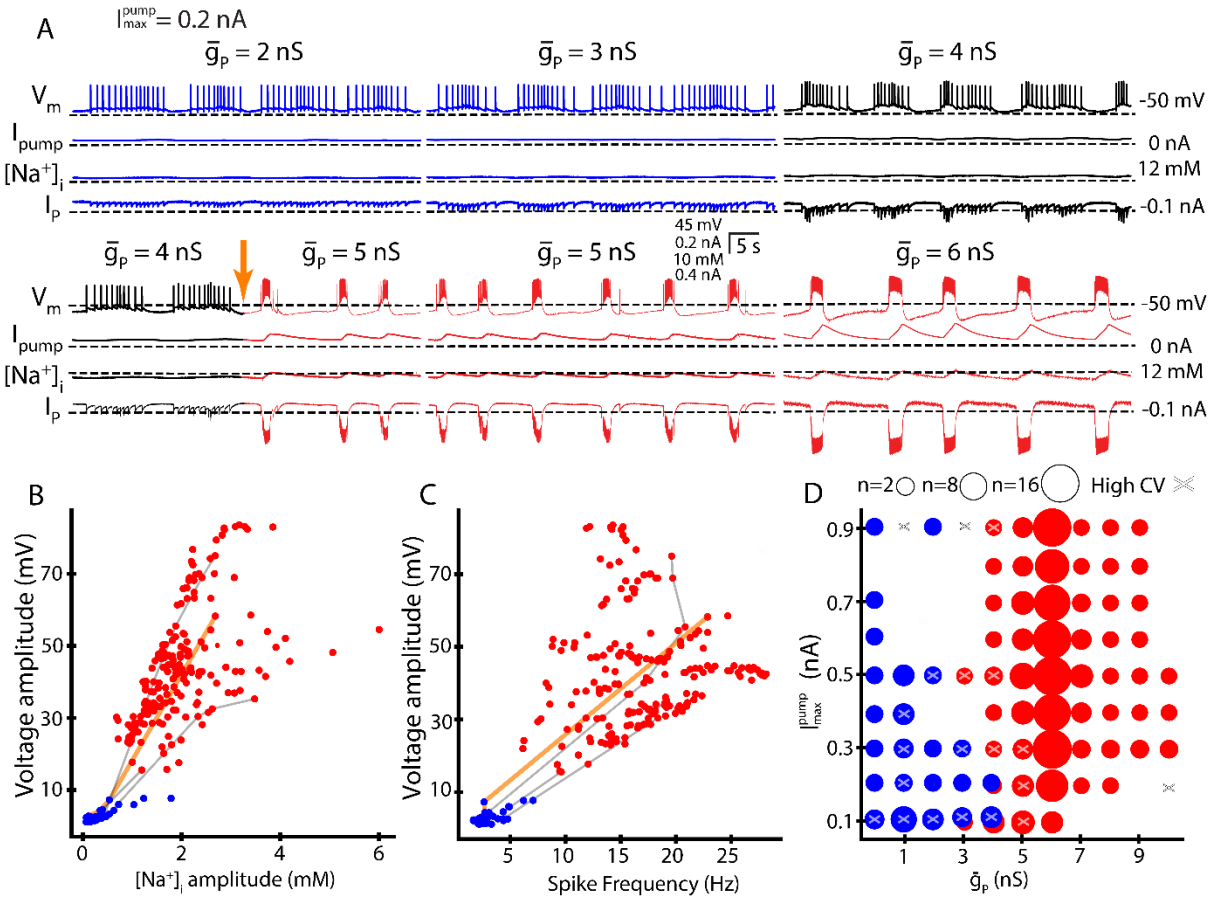

Figure 8. Two bursting regimes observed while varying $\bar{g}_P$ and I_{max}^{pump} introduced by dynamic clamp

A: This set of voltage traces exemplify how keeping I_{max}^{pump} at 0.2 nA and setting $\bar{g}_P$ above some critical value causes a transition of the neuron into the HVA bursting regime. In this and all subsequent figures I_{pump} and I_P are dynamic-clamp injected currents and $\bar{g}_P$ and I_{max}^{pump} are their parameter values, respectively. The voltage traces are from the same preparation under similar conditions; the only thing that changes between subsequent traces is the $\bar{g}_P$ parameter—the arrow points at the moment when the experimenter changed $\bar{g}_P$ from 4 to 5 nS. B: Scatterplot of waveform envelope voltage amplitude and $[Na^+]_i$ amplitude. C: Scatterplot of voltage amplitude and average intraburst spike frequency. D: Two-parameter map ($\bar{g}_P$ I_{max}^{pump}) of color-coded parameter sets exhibiting two different bursting regimes: the LVA and HVA bursting regimes are

separated to the left and right areas of the map, blue and red groups, respectively. There is an area where blue and red data points overlap at the border. The size of each circle indicated the number of accepted experiments with the color-coded outcome. ⋉ indicates that there were experiments with high variability in cycle period T (high coefficient of variation: K≥0.27) that were excluded with this parameter set from the analysis. The threshold for the transition from the LVA to the HVA bursting varies between neurons and could be subject to animal-to-animal variability (Wenning, Norris, Günay, Kueh, & Calabrese, 2018). B-D: Output from Gaussian Naive Bayes machine learning classification algorithm are color-coded by red and blue; red for the HVA bursting and blue for the LVA rhythm. Gray lines connect data points from the same experiment (voltage traces not shown). The gold line connects the data points from the sample traces (A). Data points connected in ascending $\bar{g}_P$ order, not in the order the parameters were varied. In most experiments, we varied $\bar{g}_P$ in a random order, but for illustration purposes, the parameters for the experimental traces in A are shown in ascending order.

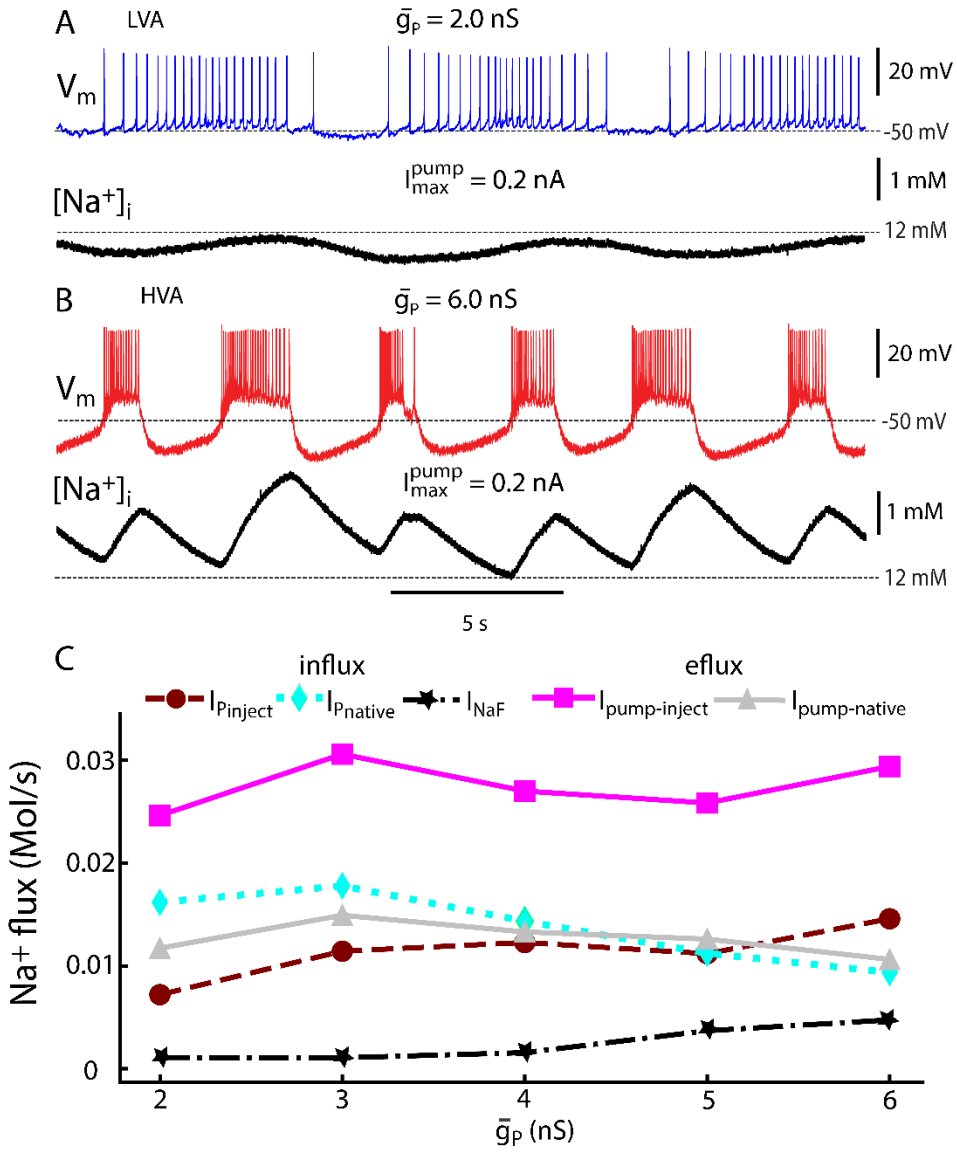

Figure 9. Virtual Na^+ fluxes produced by dynamic-clamp injected ($I_{Pinject}$ and $I_{pump-inject}$) and by estimated native currents (I_{NaF}, $I_{pump-native}$, and $I_{P-native}$)

A, B: voltage and virtual $[Na^+]_i$ traces from the LVA and HVA rhythms from the same preparation. Each burst produces a peak in $[Na^+]_i$. C: Averaged current-specific breakdown of influx and efflux of $[Na^+]_i$, as a function of dynamic-clamp injected $\bar{g}_P$. Only in this figure panel, we differentiate between the dynamic-clamp injected I_P and I_{pump}, and the native I_P, and I_{pump} otherwise all currents shown in figures are dynamic-clamp injected.

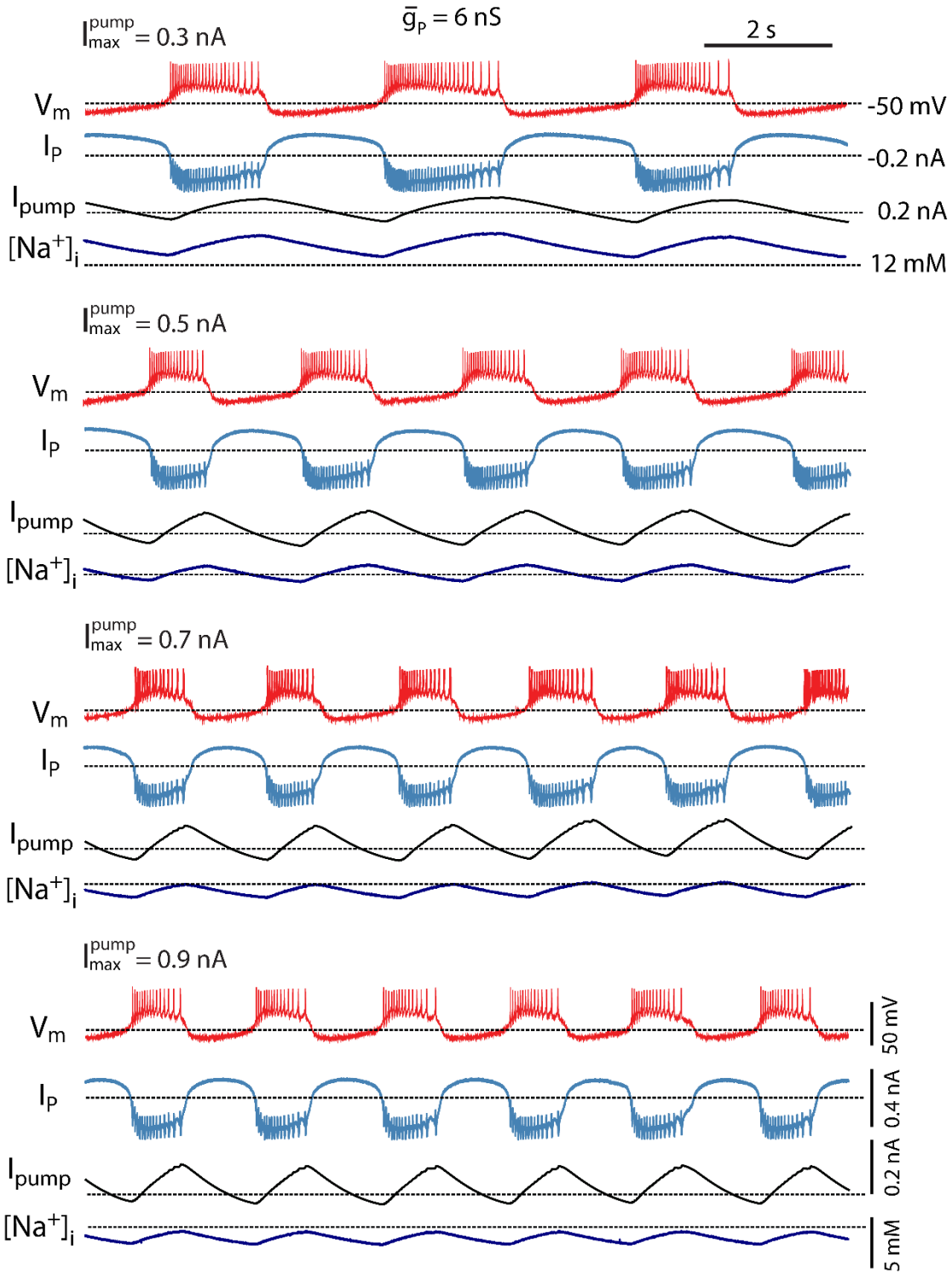

Figure 10. Increasing the maximal pump activity (I_{max}^{pump}) speeds up the HVA bursting regime.

A set of dynamic clamp traces shows that while keeping the HN(7) neuron in the HVA bursting regime with dynamic-clamp injected $\bar{g}_P = 6\ nS$, incrementing dynamic clamp injected I_{max}^{pump} decreased the burst duration and interburst interval, and thus the cycle period. Note that the upregulation of the I_{max}^{pump} changes the pump dynamics, by increasing the the amplitude of the I_{pump} oscillation but not its median value. Each experimental data sample is comprised of a set of four signal traces recorded in real-time by our dynamic clamp system, from top to bottom, the traces are membrane potential V_m (mV), injected I_P (nA), injected I_{pump} (nA), virtual $[Na^+]_i$ (mM).

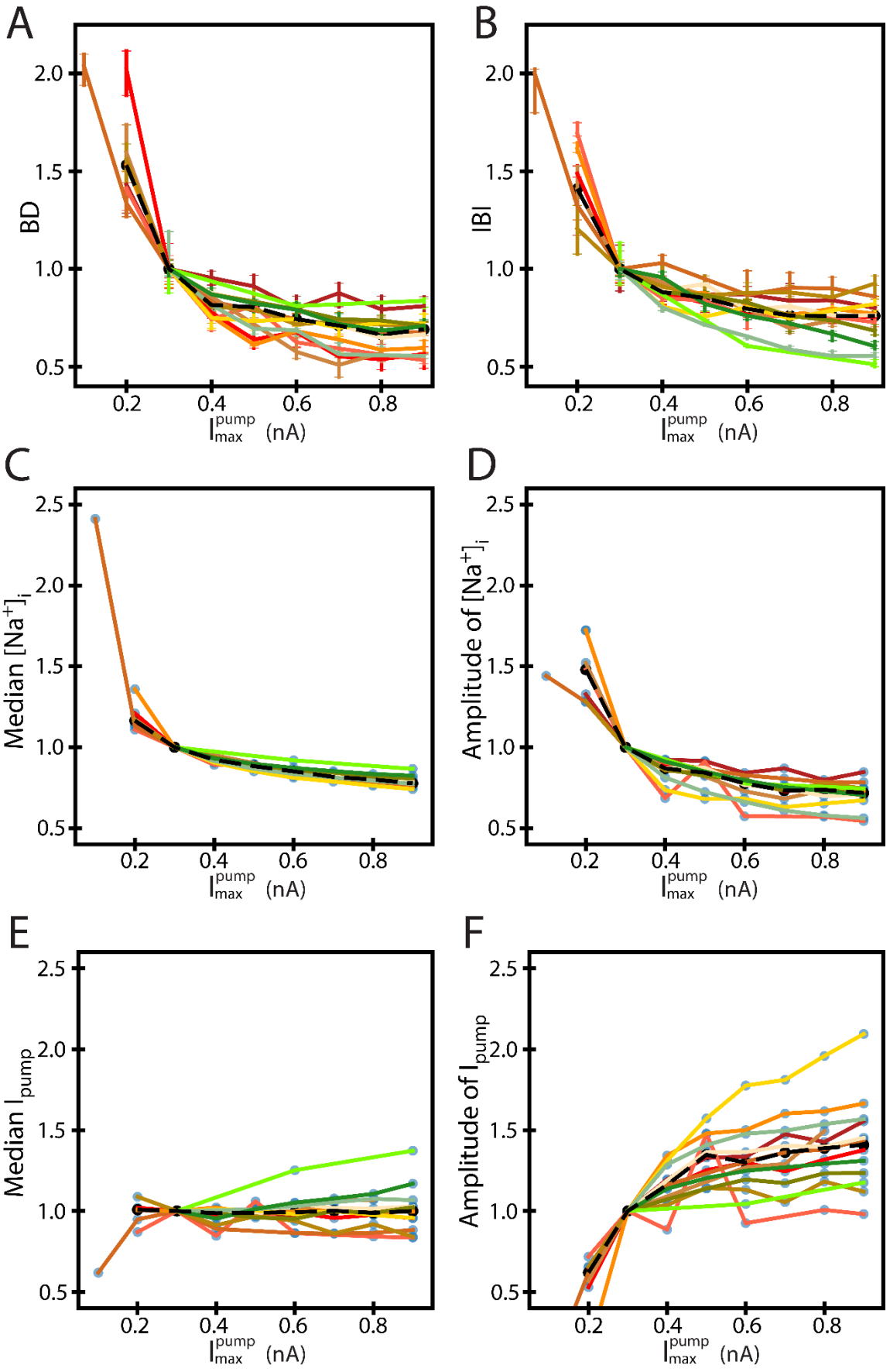
A
B
C
D
E
F
BD
IBI
Median [Na+]i
Amplitude of [Na+]i
Median Ipump
Amplitude of Ipump
Imax pump (nA)
0.5
1.0
1.5
2.0
2.5
0.2
0.4
0.6
0.8

Figure 11. Increasing dynamic-clamp injected I_{max}^{pump} decreased burst duration, interburst interval, and $[Na^+]_i$ dynamics in the HVA bursting regime.

The average trend across experiments in the HVA bursting regime shows that upregulation of dynamic-clamp injected I_{max}^{pump}decreases the following characteristics, burst duration (A) and interburst interval (B), the median intracellular $[Na^+]_i$ (C), and $[Na^+]_i$ amplitude (D). However, upregulating I_{max}^{pump} does not affect the median I_{pump} (E) but increases the amplitude of the I_{pump} oscillations (F). Changes of different characteristics are shown as normalized pooled data from multiple experiments, represented by different colors consistent between subplots. The dashed black line consists of the mean value across experiments for a given I_{max}^{pump}.

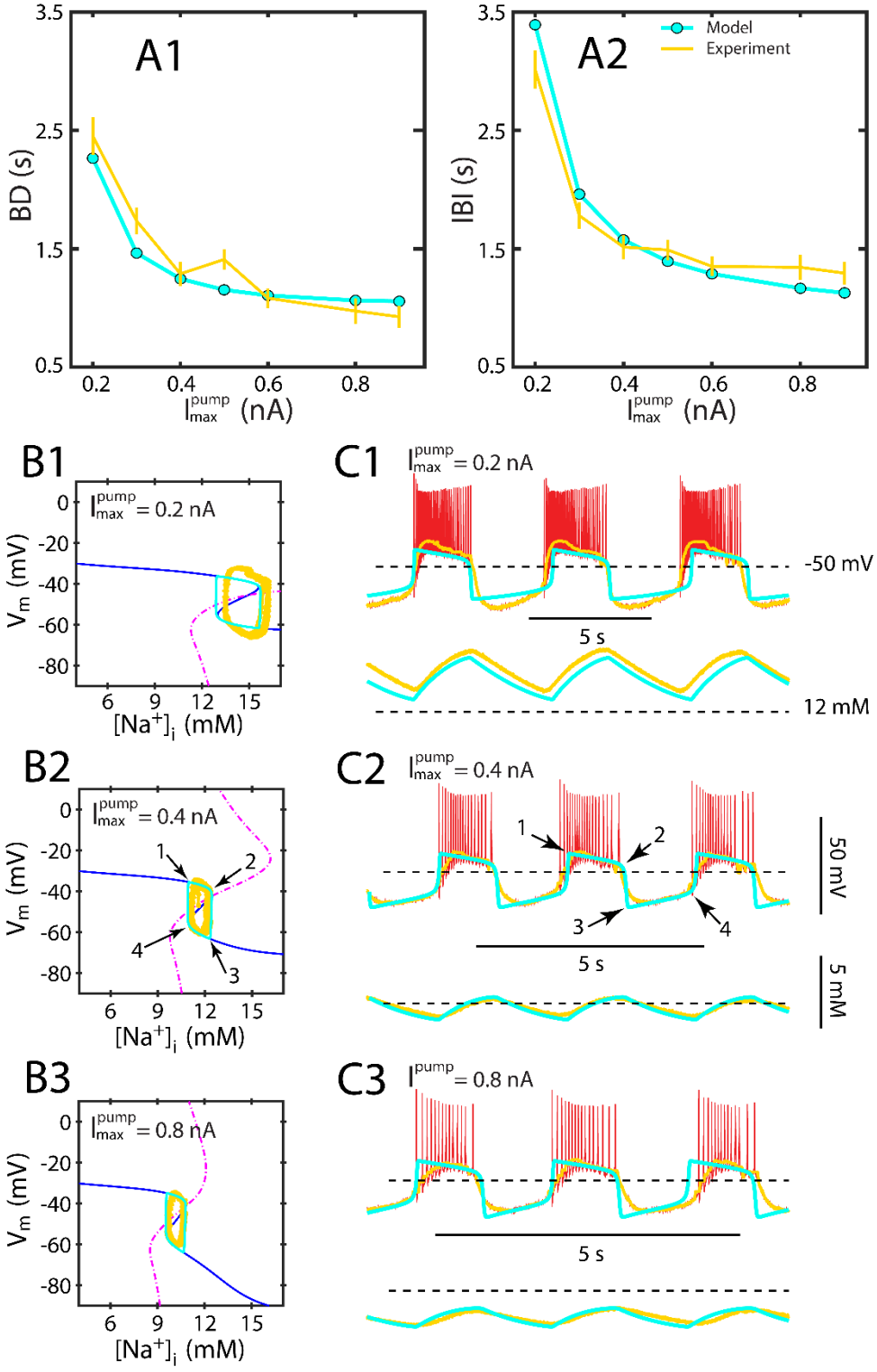
A1
A2
Model
Experiment
BD (s)
IBI (s)
I_{max}^{pump} (nA)
B1
B2
B3
I_{max}^{pump} = 0.2 nA
I_{max}^{pump} = 0.4 nA
I_{max}^{pump} = 0.8 nA
V_m (mV)
$[Na^+]_i$ (mM)
C1
C2
C3
-50 mV
12 mM
5 s
50 mV
5 mV
1
2
3
4

Figure 12. A two-dimensional HN model unravels the dynamics of the interaction of the persistent Na^+ and pump currents in a leech heart interneuron with I_P and I_{pump} augmented by dynamic clamp.

Our model explains the speeding up of the HVA bursting observed in the dynamic clamp experiments with increasing I_{max}^{pump}. A: Envelope characteristics of the 2D model (cyan) match corresponding bursting characteristics obtained from a single dynamic clamp experiment: up-variation of dynamic-clamp injected I_{max}^{pump} decreases BD and IBI. These graphs show the effect of up-variation I_{max}^{pump} from 0.3 to 0.9 nA, while keeping dynamic clamp injected $\bar{g}_P$ at 6 nS on BD (A1) and IBI (A2). The model mimicked the parameter changes of experimental protocol and did not change any other model parameters. These graphs demonstrate a good fit between experiment and model (BD relative error =0.1004, IBI relative error= 0.0913). B1-3: Phase portraits showing model periodic orbits (limit cycles) and nullclines and projected experimental data (left), accompanied by timeseries of the experimental and model membrane potential, membrane potential envelope, and $[Na^+]_i$ (right) for three different values of injected I_P. C: timeseries of experimental (yellow) and simulated (green) V_m envelope for three levels of I_{max}^{pump}. B2, C2: The V-nullcline is the Z-shaped blue curve and the $[Na^+]_i$ -nullcline is the magenta curve. The intersection between these nullclines determines location of the unstable steady state within the limit cycle. Their geometry defines the trajectory of the limit cycle of the model (Figure 6B).

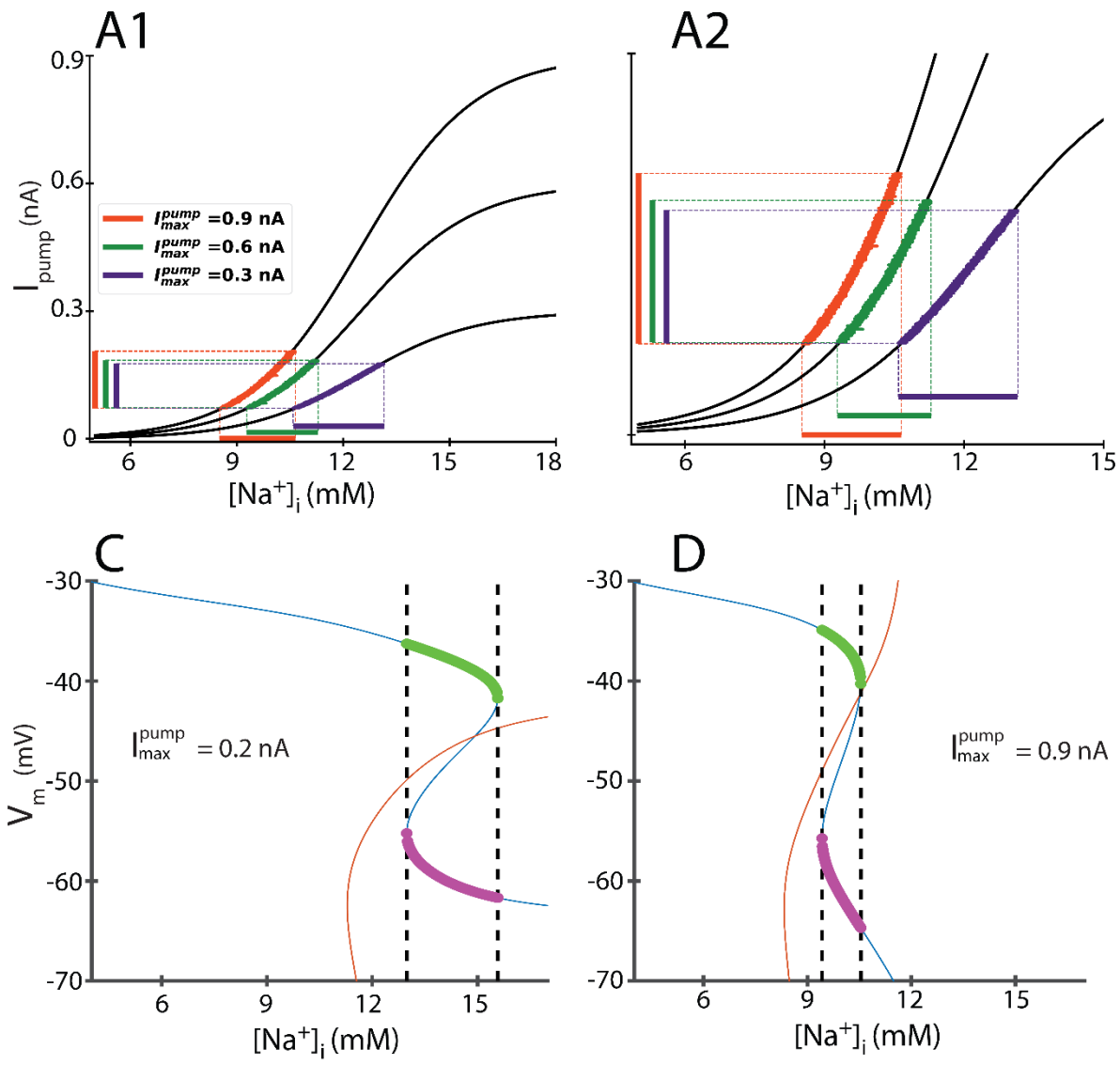

Figure 13. Amplitude of $[Na^+]_i$ in experimental data, and model nullclines in the phase plane

A1. Black curves represent activation functions for three levels of I_{max}^{pump}: 0.3, 0.6 and 0.9 nA. I_{pump} as a function of $[Na^+]_i$ plotted over the activation curves, color coded for each I_{max}^{pump}. Vertical projections to the left demark maximum and minimum I_{pump} values. Horizontal projections to the bottom demark maximum and minimum $[Na^+]_i$ values. A2: Zoomed inset of A1. These curves and ranges show the dependence of Na^+/K^+ activity as a function of $[Na^+]_i$. Consistent with figure 5, the range of $[Na^+]_i$ at I_{max}^{pump} 0.6 and 0.9 nA decreased relative to 0.3

nA, while the range of I_{pump} increased. B and C: Blue curve is the V-nullcline and red curve is the $[Na^+]_i$ nullcline. Green filled circles are 100 interpolated data points used to estimate burst duration; magenta circles are the 100 data points used to estimate the interburst interval. Vertical dashed lines project from the nullcline kneepoints and delimit the boundary of $[Na^+]_i$ amplitude. B: I_{max}^{pump}: 0.2 nA, C: I_{max}^{pump}: 0.9 nA.

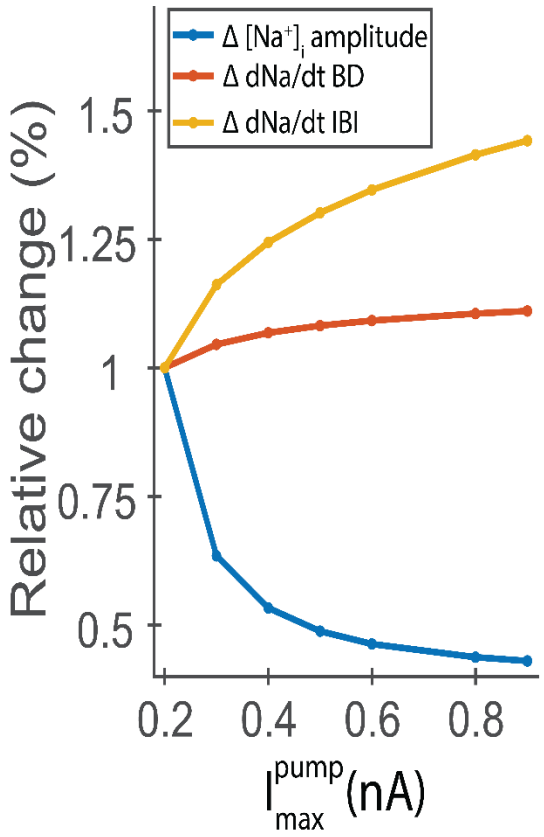

Figure 14. $[Na^+]_i$ amplitude decreases 57%, the $[Na^+]_i$ speed $\left(\frac{dNa}{dt}\right)$ during the burst increases 11%, and the $[Na^+]_i$ speed during the interburst interval increases significantly 44% as a function of I_{max}^{pump}.

These curves illustrate the relative change of the $[Na^+]_i$ amplitude and $[Na^+]_i$ speed as a function of I_{max}^{pump}. We collected the $[Na^+]_i$ amplitude and speed during the burst and interburst interval computed from the 100 points depicted in Figures 7C and 7D. To compute the relative change, we divided each $[Na^+]_i$ amplitude or speed by its correspondent collected at the initial point (I_{max}^{pump} =0.2 nA).

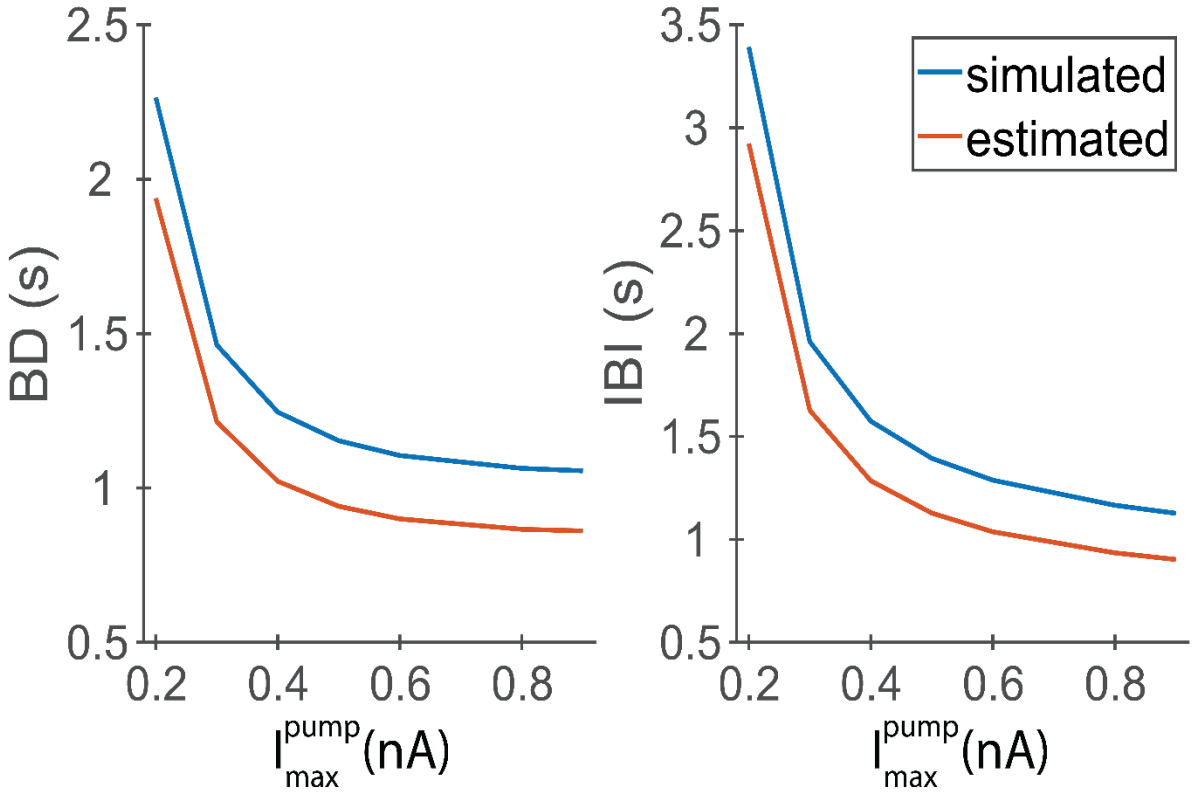

Figure 15. The estimated BD and IBI preserve the dependence on I_{max}^{pump} observed experimentally and confirmed by the 2-D HN model.

The estimated BD and IBI from nullcline analysis preserve the trend observed on the BD and IBI from simulations of the 2D model. Importantly, these estimates were computed by interpolating 100 points from the nullclines' geometry and demonstrating that the $[Na^+]_i$ speed plays an essential role in determining the BD and IBI. To compute these estimates, we used the points illustrated in Figure 13 (V and $[Na^+]_i$ coordinates) to compute the currents and $[Na^+]_i$ speed. We divided the change in $[Na^+]_i$ amplitude by the $[Na^+]_i$ speed to get the estimated BD and IBI.

3.7.1 Supplementary data: Dynamic clamp model

$$Cm\,\frac{dV}{dt} = -(I_{NaF} + I_P + I_{K1} + I_{K2} + I_{KA} + I_h + I_{CaF} + I_{CaS} + I_{pump} + I_{leak})$$

$$I_{NaF} = \bar{g}_{NaF} \cdot m_{NaF}^3 \cdot \mathrm{h}_{NaF} \cdot (V - E_{Na})$$

$$I_P = \bar{g}_P \cdot m_P \cdot (V - E_{Na})$$

$$I_{K1} = \bar{g}_{K1} \cdot m_{K1}^2 \cdot h_{K1} \cdot (V - E_K)$$

$$I_{K2} = \bar{g}_{K2} \cdot m_{K2}^2 \cdot (V - E_K)$$

$$I_{KA} = \bar{g}_{KA} \cdot m_{KA}^2 \cdot h_{KA} \cdot (V - E_K)$$

$$I_h = \bar{g}_h \cdot m_h^2 \cdot (V - E_h)$$

$$I_{CaF} = \bar{g}_{CaF} \cdot m_{CaF}^2 \cdot h_{CaF} \cdot (V - E_{Ca})$$

$$I_{CaS} = \bar{g}_{CaS} \cdot m_{CaS}^2 \cdot h_{CaS} \cdot (V - E_{Ca})$$

$$I_{pump} = \frac{I_{max}^{pump}}{1 + e^{\frac{[Na^+]_{ih} - [Na^+]_i}{[Na^+]_{is}}}}$$

$$I_{leak} = g_{leak} \cdot (V - E_{leak})$$

$$\frac{dm_{NaF}}{dt} = \frac{f_\infty(-150, 0.029, V) - m_{NaF}}{0.0001}$$

$$\frac{dh_{NaF}}{dt} = \frac{f_\infty(500, 0.03, V) - h_{NaF}}{\tau_{hNa}(V)}$$

$$\tau_{hNa}(V) = 0.004 + \frac{0.02}{cosh[300 \cdot (V + 0.0027)]} + \frac{0.006}{1 + e^{(500 \cdot (V + 0.028))}}$$

$$\frac{dm_P}{dt} = \frac{f_\infty(-120, 0.039, V) - m_P}{\tau(400, 0.057, 0.01, 0.2, V)}$$

$$\frac{dm_{K1}}{dt} = \frac{f_{\infty}(-143, 0.021, V) - m_{K1}}{\tau(150, 0.016, 0.001, 0.011, V)}$$

$$\frac{dh_{K1}}{dt} = \frac{f_{\infty}(111, 0.028, V) - h_{K1}}{\tau(-143, 0.013, 0.5, 0.2, V)}$$

$$\frac{dm_{K2}}{dt} = \frac{f_{\infty}(-83, 0.02, V) - m_{K2}}{\tau(200, 0.035, 0.057, 0.043, V)}$$

$$\frac{dm_{KA}}{dt} = \frac{f_{\infty}(-130, 0.044, V) - m_{KA}}{\tau(200, 0.03, 0.005, 0.011, V)}$$

$$\frac{dh_{KA}}{dt} = \frac{f_{\infty}(160, 0.063, V) - h_{KA}}{\tau(-300, 0.055, 0.026, 0.0085, V)}$$

$$\frac{dm_{h}}{dt} = \frac{f_{\mathrm{h}\infty}(V) - m_{h}}{\tau(-100, 0.073, 0.7, 1.7, V)}$$

$$f_{h\infty}(V) = \frac{1}{1 + 2 \cdot e^{180 \cdot (V + 0.047)} + e^{500 \cdot (V + 0.047)}}$$

$$\frac{dm_{CaF}}{dt} = \frac{f_{\infty}(-600, 0.0467, V) - m_{CaF}}{\tau(-330, 0.0467, 0.011, 0.024, V)}$$

$$\frac{dh_{CaF}}{dt} = \frac{f_{\infty}(350, 0.055, V) - h_{CaF}}{\tau(270, 0.055, 0.06, 0.31, V)}$$

$$\frac{dm_{CaS}}{dt} = \frac{f_{\infty}(-420, 0.0472,) - m_{CaS}}{\tau(-400, 0.0487, 0.005, 0.134, V)}$$

$$\frac{dh_{CaS}}{dt} = \frac{f_{\infty}(360, 0.055,) - h_{CaS}}{\tau(-250, 0.043, 0.2, 5.25, V)}$$

$$E_{Na} = 0.02526 ln\left(\frac{[Na^{+}]_{o}}{[Na^{+}]_{i}}\right)$$

Table 6. Parameters of dynamic clamp model.

$\bar{g}_{NaF}$	150	I_{pump}^{max}	[0.3, 0.9]
$\bar{g}_{P-inject}$	[1, 6]	Na_{ih}	0.012
$\bar{g}_{P-native}$	5	Na_{is}	0.0016
$\bar{g}_{K1}$	80	Na_o	0.115
$\bar{g}_{K2}$	80	E_K	-0.07
$\bar{g}_{KA}$	100	E_h	-0.021
$\bar{g}_h$	4	E_{Ca}	0.135
$\bar{g}_{CaF}$	5	E_e	-0.045
$\bar{g}_{CaS}$	4		
g_{leak}	7		

- Conductances are in nanoSiemens, and concentrations are in Moles, reversal potentials are in Volts, currents are in nanoAmps

4 INTERACTION OF I_{PUMP}, I_P, AND I_H IN CONTROLLING THE RHYTHMIC BURSTING ACTIVITY OF HN NEURONS.

4.1 Introduction

The previous chapter established that the persistent-sodium current (I_P) interacts with the Na^+/K^+ pump current (I_{pump}) to form a flexible oscillatory mechanism. This chapter explores how the I_P and I_{pump} mechanism interacts with the h-current (I_h). Specifically, how inhibiting the I_h affects the rhythm of leech heart interneurons (HN neurons) in the High Voltage Amplitude bursting regime described in chapter 3. Tobin and Calabrese (2005a) showed that I_h interacts with I_{pump} in controlling the bursting rhythm of HN neurons, when modulated by the endogenous leech neuropeptide Myomodulin. 1 μM Myomodulin application inhibits the Na^+/K^+ pump and enhances I_h, consequently shortening the period of the HN neurons in coupled half-center oscillators (HCOs). Myomodulin application decreases period, burst duration, interburst interval, increases spike frequency, and enhances burst robustness in synaptically isolated HN neurons (0.5 mM Bicuculline added to the saline). Applying 2 mM Cs^+ increases the period of HN neurons (Masino & Calabrese, 2002a; Tobin & Calabrese, 2005a). Applying first 2 mM Cs^+, and then 1μM Myomodulin decreases the period and increases the spike frequency compared to the pre-Myomodulin condition (Tobin & Calabrese, 2005a). Later studies confirmed those results and, further supported that I_h interacts with I_{pump} in controlling the rhythm of HN neurons. Kueh et al., (2016) showed that stimulating the Na^+/K^+ pump by increasing the intracellular sodium concentration ($[Na^+]_i$) with Na^+ ionophore monensin speeds-up the HN HCO rhythm symmetrically; subsequent application of 2 mM Cs^+ lengthens the IBI while the BD remains preserved. These observations support the hypothesis that I_h plays a vital role in determining burst initiation; further, because I_h partially depends on Na^+, I_h interacts with the Na^+/K^+ pump controlling the interburst interval in HN neurons.

In the previous chapter, we explored how the Na^+/K^+ pump activity is controlled intracellular sodium concentration ($[Na^+]_i$) during rhythmic bursting. Because I_h has Na^+ and K^+ components (Parker J. Ellingson et al., 2021; Kueh et al., 2016), I_h contributes to $[Na^+]_i$ and interacts with the Na^+/K^+ pump. Therefore, I_h action must influence the rhythm generated by the mechanisms of interaction of I_P and I_{pump} described in chapter 3. Further, the I_h and the I_P have some similarities, such as playing a role in burst initiation, supporting spike frequency and evolving in a slow timescale compared to transient currents. Based on conclusions from the literature and chapter 3, we hypothesized that I_h plays a role in determining burst initiation: reducing I_h lengthens the interburst interval of isolated HN(7) neurons in the HVA bursting regime. Here we investigated how partial reduction of I_h, with dynamic clamp and pharmacological manipulation, affected the burst rhythm of isolated HN neurons.

4.2 Methods

4.2.1 Dynamic clamp

We implemented the dynamic clamp model from our previous publication (Erazo-Toscano et al., 2021) to subtract I_h. To reduce the native I_h with dynamic clamp, we injected $\bar{g}_h$= -4 nS, based on the canonical value of $\bar{g}_h$ in the HN model (Kueh et al., 2016). The dynamic clamp I_h was based on the equations:

$$I_h = m_h^2 \cdot \bar{g}_h \cdot (V - E_h)$$

$$\frac{dm_h}{dt} = \frac{f_{h\infty}(V) - m_h}{\tau_h}$$

$$\tau_h = 0.7 \cdot \frac{1.7}{1 + e^{-100 \cdot (V + 0.073)}}$$

The other dynamic clamp currents I_P and I_{pump} were those described in our previous publication (Erazo-Toscano et al., 2021).

4.2.2 Data normalization and oscillation amplitudes computation

We analyzed the following (dependent variables) characteristics of bursting: burst duration (BD), interburst interval (IBI), $[Na^+]_i$ amplitude, $[Na^+]_i$ peaks, $[Na^+]_i$ troughs, I_{pump} amplitude, I_{pump} peaks, I_{pump} troughs. Each of these characteristics was normalized in an experiment-by-experiment fashion as a function of I_{max}^{pump}: we divided each dependent variable by its value collected with I_{max}^{pump} = 0.3 nA in normal saline (control condition). We computed the amplitude of membrane potential, $[Na^+]_i$, and I_{pump} oscillations by detecting the peaks and troughs of the signal, then subtracted the troughs from the peaks in a pairwise fashion.

4.2.3 Dynamic clamp parameter variation

The dynamic clamp parameters were manipulated as follows: keep $\bar{g}_P$= 6.0 nS, (chosen because it assured HVA bursting) and systematically vary I_{max}^{pump} (0.3, 0.6, 0.9 nA); namely, an

I_{max}^{pump} sweep. For all these experiments, we performed one I_{max}^{pump} sweep in the control condition, and a subsequent sweep blocking I_h (either pharmacologically or with dynamic clamp subtraction).

4.2.4 Statistics

We performed repeated measures two-way analysis of variance (ANOVA) and post-hoc multiple comparison using Tukey's honest difference test. Data analysis implemented in Python 3.7 using the statsmodels Python module.

4.3 Results

4.3.1 Partially subtracting I_h with dynamic clamp ($\bar{g}_h$= -4 nS) increased the IBI and the BD

I_h plays an essential role in controlling IBI. I_h contributes to burst initiation, determining the IBI; I_h also partially contributes to $[Na^+]_i$ affecting I_{pump} and, thus, I_h may have an indirect albeit small effect on BD. Our dynamic clamp setup allowed us to manipulate I_h in HN(7) neurons without pharmacological manipulation. Figure 17 shows the trends in HN(7) neuron burst characteristics in normal saline before (control) and after subtracting I_h with dynamic clamp ($\bar{g}_h$ = -4 ns). Consistent with data from chapter 3, the trends in control (normal saline no dynamic-clamp I_h) show that HN(7) burst duration (BD) (Figure 16, A1) and interburst interval (IBI) (Figure 16, A2) decreased when we augmented dynamic clamp I_{max}^{pump}. The trends in the I_h subtraction ($\bar{g}_h$= -4 nS) condition showed that when we subtracted I_h with dynamic clamp, the BD (Figure 16, B1) and IBI increased (Figure 16, B2). On average, subtracting I_h with dynamic clamp lengthened the BD by ≈20% and IBI by ≈60% (Table 7). Altogether our dynamic clamp experiments demonstrate that subtracting I_h with dynamic clamp lengthens BD and IBI in HN(7) neurons.

IBI lengthening supports our hypothesis, but BD lengthening was somewhat unexpected. We ought to look at individual experimental data to better interpret these results; in a nutshell Cs+

affects the membrane capacitance, and thus sometimes affects the burst duration, but the effect on IBI are explained by blocking I_h. Figure 17 shows the voltage traces from a sample experiment and illustrates the temporal difference between HN(7) neuron rhythms in control and I_h subtraction conditions. The sample experimental traces show that when we subtracted I_h with dynamic clamp, the $[Na^+]_i$ amplitude increased (Figure 17, A1-3, B1-3 $[Na^+]_i$), which subsequently increased the amplitude of I_{pump} and hyperpolarized the membrane potential during the IBI. Further analysis of variance (ANOVA) of the pooled data demonstrated that the $[Na^+]_i$ troughs and peaks depend on I_{max}^{pump} and do not vary between control and I_h subtraction (Figure 18 A, B) (troughs: ANOVA F=20.11, $p \leq 0.0001$, Tukey's Multi-comparison test $p \leq 0.01$; peaks: ANOVA F=45.17, $p \leq 0.0001$, Tukey's Multi-comparison test $p \leq 0.05$. N=5); however, the $[Na^+]_i$ and I_{pump} amplitudes increased when we subtracted I_h, for all I_{max}^{pump} values (Figure 18 C, D) ($[Na^+]_i$ amplitude ANOVA F=12.56 , $p \leq 0.001$, Tukey's Multi-comparison test $p \leq 0.005$; I_{pump} amplitude ANOVA F=15.96 , $p \leq 0.001$, Tukey's Multi-comparison test $p \leq 0.001$). Characterization of the activation curves of I_{pump} as a function of $[Na^+]_i$ further supports these notions (Figure 19). Figure 19 shows that the amplitudes of $[Na^+]_i$ and I_{pump} lengthen when I_h was subtracted with dynamic clamp. Our statistical and graphical analysis demonstrates that subtracting I_h alters the Na^+ dynamics of HN neurons by enhancing the amplitude of $[Na^+]_i$ and I_{pump} oscillations.

To understand why the BD increased when we subtracted I_h, we noted that the $[Na^+]_i$ troughs systematically, although not statistically significantly, are at a lower concentration with $\bar{g}_h$= -4 nS compared to the troughs in the control condition. When a burst initiated in the control condition, the $[Na^+]_i$ was closer to the concentration of half-activation of the I_{pump} than during I_h subtraction. Because in I_h subtraction the initial $[Na^+]_i$ was lower at the beginning of the burst (Figure 17), it took more time to accumulate enough $[Na^+]_i$ and activate the I_{pump} and terminate the burst. The IBI lengthened because I_h contributes to burst initiation, and by subtracting it, we restricted the

currents that contribute to burst initiation to I_P and I_{CaS}. As shown above, our results demonstrate that I_h plays a vital role in controlling the HN bursting mechanism.

	BD	IBI
Control	1.00	1.00
$\bar{g}_h$= -4 nS	1.20	1.60
0.5 mM Cs	0.96	1.39
2 mM Cs	1.76	1.27

Table 7. Normalized burst characteristics in control, I_h subtract ($\bar{g}_h$= -4.0 nS) (N=5), 0.5 mM Cs^+ (N=5), and 2mM Cs^+ (N=7) with I_{max}^{pump}= 0.3 nA

4.3.2 A partial block of I_h with 0.5mM Cs^+ increased IBI but did not affect BD

For the next series of experiments, we tested whether a small concentration of a pharmacological I_h blocker would corroborate our dynamic clamp I_h subtraction experimental results. We performed two sets of dynamic clamp I_{max}^{pump} parameter variation: first in control (normal saline), and then in 0.5 mM Cs^+ saline (Methods). Figure 20 shows the HN(7) neuron burst characteristics trends in control and 0.5 mM Cs^+ saline. In the control condition, these trends consistently show that BD (Figure 20, A1) and IBI (Figure 20, A2) decrease when we augment the dynamic clamp I_{max}^{pump}. Pooled trends in 0.5 mM Cs^+ saline showed that the BD slightly decreased when we blocked I_h with 0.5 mM Cs^+ (Figure 20, B1) while the IBI significantly increased (Figure 20, B2). On average, blocking I_h with 0.5 mM Cs^+ shortened the BD by ≈4% and lengthened the IBI by ≈39% (Table 7). Such an effect of Cs^+ application on HN neurons' burst characteristics has been reported previously (Kueh et al., 2016; Tobin & Calabrese, 2005a). Altogether our results in 0.5 mM Cs^+ support IBI lengthening with dynamic clamp

subtraction. Although we observed a discrepancy in the average BD in 0.5 mM Cs^+ compared to I_h subtraction, our 0.5 mM Cs^+ results are consistent with previously published data.

Application of 0.5 mM Cs^+ saline modified neuronal $[Na^+]_i$ dynamics, which altered I_{pump} activity and thus the burst rhythm of HN neurons. Figure 21 shows experimental sample voltage traces in normal (control), and 0.5 mM Cs^+ saline from one preparation. A contrast can be observed in $[Na^+]_i$ and I_{pump} from control and 0.5 mM Cs^+ with I_{max}^{pump}=0.3, 0.6 and 0.9 nA (Figure 21, A1-3, B1-3). In normal saline, the baseline $[Na^+]_i$ is greater than in 0.5 mM Cs^+; therefore, the I_{pump} decreased. Further, when I_{max}^{pump}=0.3 nA, the maximum injected I_P also decreased in 0.5 mM Cs^+ compared to control. Analysis of I_{pump} activation curves showed a remarkable contrast between the control condition and 0.5 mM Cs^+. Application of 0.5 mM Cs^+ increased the $[Na^+]_i$ and I_{pump} amplitudes compared to the control condition (Figure 22). Further, the increase of the $[Na^+]_i$ and I_{pump} amplitudes is consistent with the dynamic clamp I_h subtraction data. These results support the notion that I_h plays an essential role in interacting with the I_{pump} to contribute to the burst rhythm of HN neurons.

4.3.3 Pharmacologically blocking I_h with 2mM Cs^+ induced irregular activity in isolated HN neurons

For the third series of experiments, we tested whether there was a dose-dependent effect of Cs^+ on the rhythm of HN neurons (increased the Cs^+ concentration to 2 mM). Figure 23 shows that in normal saline (control) these neurons showed a normal rhythmic dependence on I_{max}^{pump} variation; however, when we changed the superfusion solution to 2mM Cs^+ saline, the rhythmic activity of HN neurons was inconsistent. First, the variability of BD and IBI increased in 2 mM Cs^+ compared to control (Figure 23, B1, B2). Second, the rhythmic dependence on I_{max}^{pump} variation was abolished in 3/7 preparations. Third, the trends across experiments are inconsistent between preparations. Given these reasons, subsequent data analyses were hindered because of the variability of the data.

We observed that superfusing HN neurons with 2 mM Cs^+ saline produced irregular activity in some neurons, while others preserved their rhythmicity. Three voltage trace examples illustrate the variability of the data: Figure 24 shows a sample experiment that preserved its rhythmicity in 2 mM Cs^+ saline. Figure 25shows a sample experiment with highly irregular rhythmic activity. Figure 26 shows a sample experiment in which 2 mM Cs^+ saline enhanced BD and IBI. Because Cs^+ is a non-specific I_h blocker, the application of 2 mM Cs^+ saline may affect membrane input resistance affecting neuronal excitability. Altogether, these experimental results demonstrate that a high Cs^+ concentration, gave inconsistent results and in some cases disrupts the rhythmic activity of single HN(7) neurons.

4.4 Conclusions

4.4.1 Partial I_h reduction with dynamic clamp and partial pharmacological blockade (0.5 mM Cs^+) showed consistent results

Subtracting I_h with dynamic clamp ($\bar{g}_h$= -4nS) consistently lengthened the IBI in HN neurons approximately 60% compared to their control condition in all the preparations tested. Similarly, partial blockade if I_h with 0.5 mM Cs^+ lengthened the IBI by approximately 40% on average, confirming our dynamic clamp results. Remarkably, we observed lengthening in the IBI of isolated HN neurons with dynamic clamp and 0.5 mM Cs^+ blockade of I_h. Our results demonstrate that I_h plays an important role in interacting with I_P and I_{pump} to control burst initiation and determine the IBI.

Our analysis demonstrated that when I_h was partially reduced (whether with dynamic clamp or 0.5 mM Cs^+), the $[Na^+]_i$ amplitude increased (Figure 19 and Figure 22). We observed such an effect statistically (Figure 18) and aided with the activation curves, which are visually intuitive (Figure 19 and Figure 22). Our results demonstrate that in the partial I_h blockade condition, the

I_{pump} activity was significantly enhanced compared to the control condition in the 0.5 mM Cs^+ blockade but not with the dynamic clamp subtraction (Figure 19 and Figure 22).

4.4.2 Na^+ dynamics are at the heart of the burst generating mechanism

Our experiments demonstrate that I_{pump} activity is a function of $[Na^+]_i$, and that the Na^+/K^+ pump is actively participating in the rhythmic bursting of HN neurons. In that context, it becomes intuitive that I_P interacts with I_{pump} to sustain a burst generative mechanism. Further, additional currents that contribute to $[Na^+]_i$ interact with the Na^+/K^+ pump, such as I_{NaF} and I_h. For example, our results demonstrate that a partial blockade of the I_h alters the $[Na^+]_i$, which subsequently affects the bursting of isolated HN neurons. Therefore, the mechanism we investigated in chapters 3 and 4 shows that $[Na^+]_i$ is an essential measure of neuronal activity.

4.5 References

Ellingson, P. J., Barnett, W. H., Kueh, D., Vargas, A., Calabrese, R. L., & Cymbalyuk, G. S. (2021). Comodulation of h- and Na$$/K$$ Pump Currents Expands the Range of Functional Bursting in a Central Pattern Generator by Navigating Between Dysfunctional Regimes. *The Journal of Neuroscience*, JN-RM-0158-0121.

Erazo-Toscano, R. J., Ellingson, P. J., Calabrese, R. L., & Cymbalyuk, G. S. (2021). Contribution of the Na/K Pump to Rhythmic Bursting, Explored with Modeling and Dynamic Clamp Analyses. *Journal of Visualized Experiments*(171).

Kueh, D., Barnett, W. H., Cymbalyuk, G. S., & Calabrese, R. L. (2016). Na+/K+ pump interacts with the h-current to control bursting activity in central pattern generator neurons of leeches. *Elife*, *5*, e19322.

Masino, M. A., & Calabrese, R. L. (2002a). Period differences between segmental oscillators produce intersegmental phase differences in the leech heartbeat timing network. *Journal of Neurophysiology*, *87*(3), 1603-1615.

Masino, M. A., & Calabrese, R. L. (2002b). Phase relationships between segmentally organized oscillators in the leech heartbeat pattern generating network. *Journal of Neurophysiology*, *87*(3), 1572-1585.

Tobin, A.-E., & Calabrese, R. L. (2005). Myomodulin increases I h and inhibits the Na/K pump to modulate bursting in leech heart interneurons. *Journal of Neurophysiology*, *94*(6), 3938-3950.

4.6 Figures

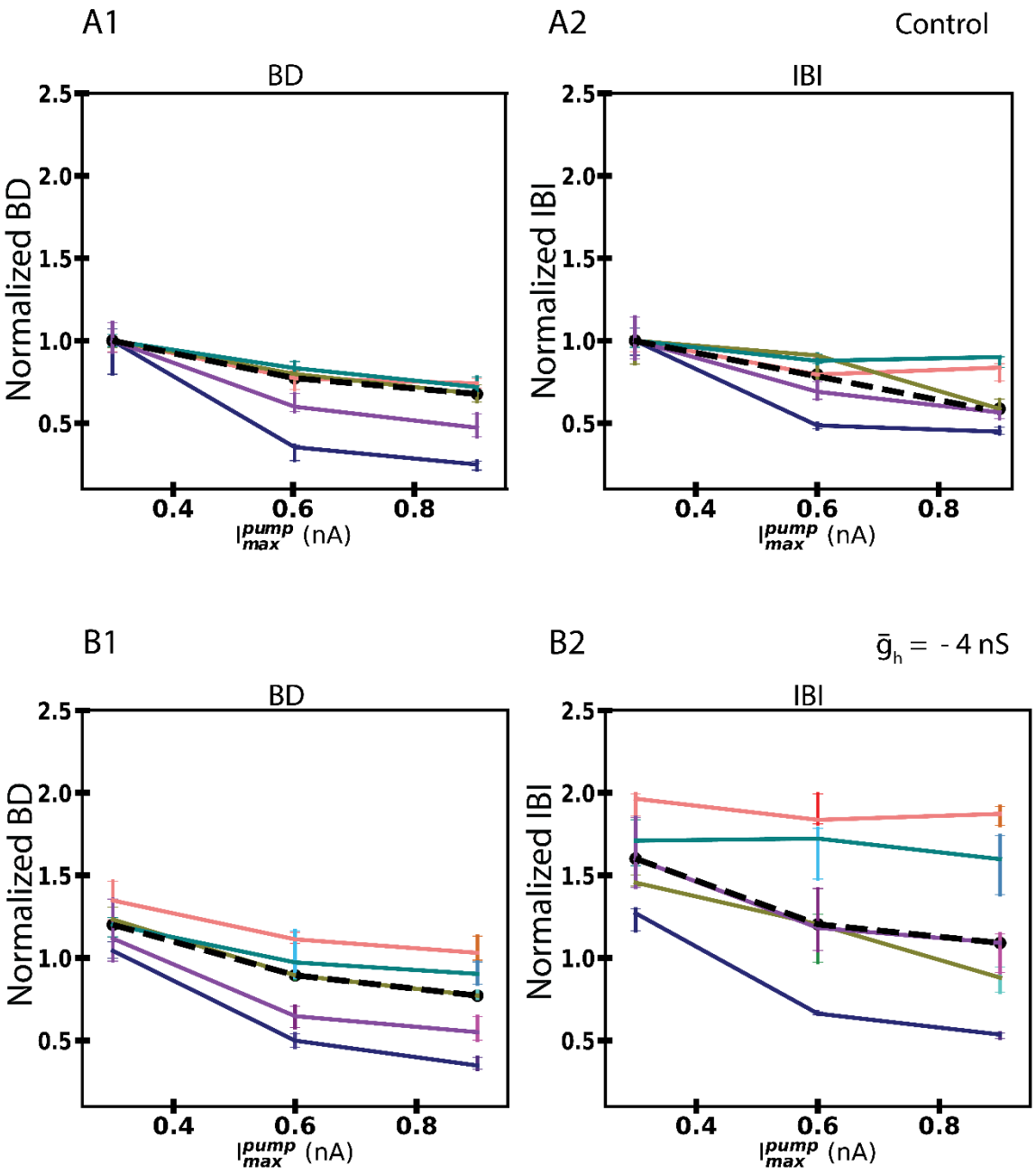
A1
BD
Normalized BD
2.5
2.0
1.5
1.0
0.5
0.4
0.6
0.8
I_{max}^{pump} (nA)
A2
Control
IBI
Normalized IBI
B1
BD
B2
$\bar{g}_h$ = - 4 nS
IBI

Figure 16. Subtracting I_h with dynamic clamp lengthens IBI by >50%, and BD ≈ 25%

Normalized burst characteristics in normal saline before (control) and after subtracting I_h with dynamic clamp ($\bar{g}_h = -4\ nS$). A1: control burst duration, A2: control interburst interval, B1: dynamic clamp ($\bar{g}_h = -4\ nS$) burst duration, B2: dynamic clamp ($\bar{g}_h = -4\ nS$) interburst interval. Each color represents a different preparation, and the overlying black dashed line is the average across experiments (N=5). The vertical lines are the first and third quantiles of the burst characteristics.

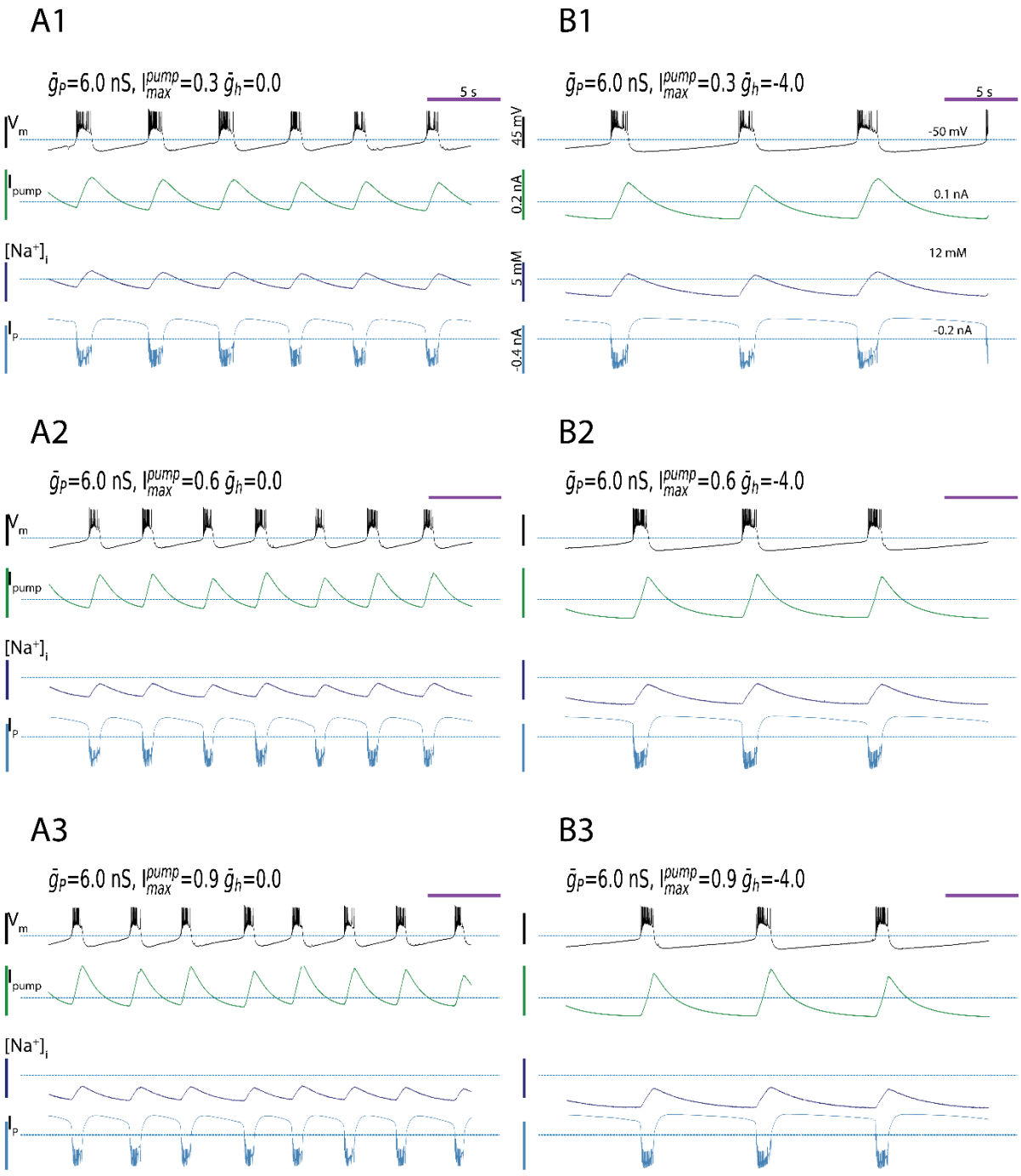

Figure 17. Sample voltage traces subtracting I_h with dynamic clamp

Experimental data in normal saline before (control) and after subtracting I_h with dynamic clamp ($\bar{g}_h = -4\ nS$). These data from a single experiment show that by subtracting I_h with dynamic

clamp, IBI an BD lengthen. The data correspond to the light coral curve in Figure 16. A1-3: Voltage, I_{pump}, $[Na^+]_i$, and I_P under control condition ($\bar{g}_h$= 0.0 nS.), three different levels of I_{max}^{pump} 0.3 (A), 0.6 (B), 0.9 (C) nA. B1-3: Experimental traces with I_h subtraction $\bar{g}_h$= -4.0 nS.

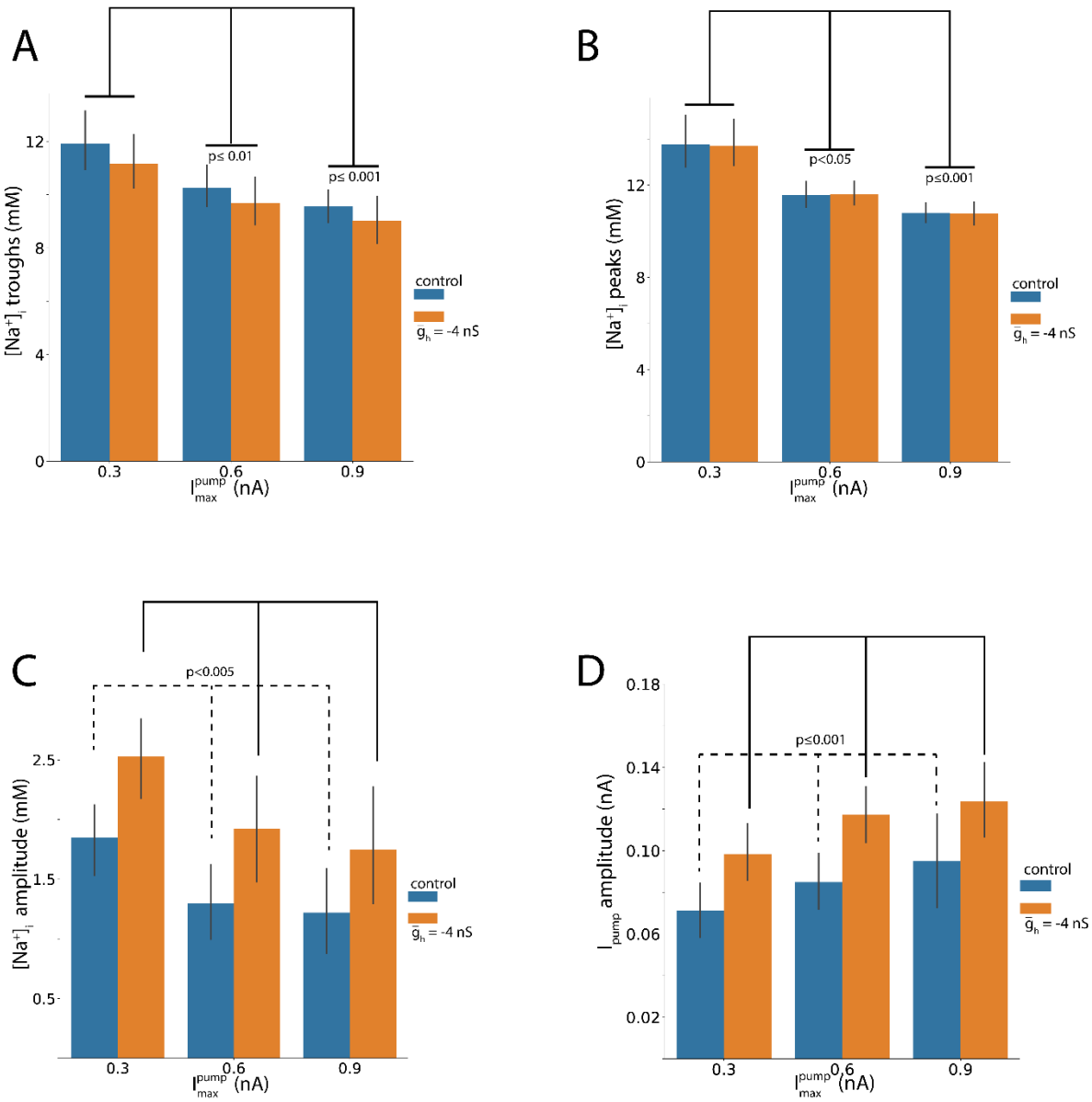

Figure 18. $[Na^+]_i$ peaks and troughs depend exclusively on the I_{pump}^{max} parameter, while $[Na^+]_i$ and I_{pump} amplitude depend on $\bar{g}_h$. Bar graphs of $[Na^+]_i$ and I_{pump} troughs and peaks, and

$[Na^+]_i$ and I_{pump} amplitude, as a function of I_{max}^{pump}; the lines connect statistically significant linear association with ANOVA: A, $[Na^+]_i$ troughs, B: $[Na^+]_i$ peaks, C: $[Na^+]_i$ amplitude, D: I_{pump} amplitude.

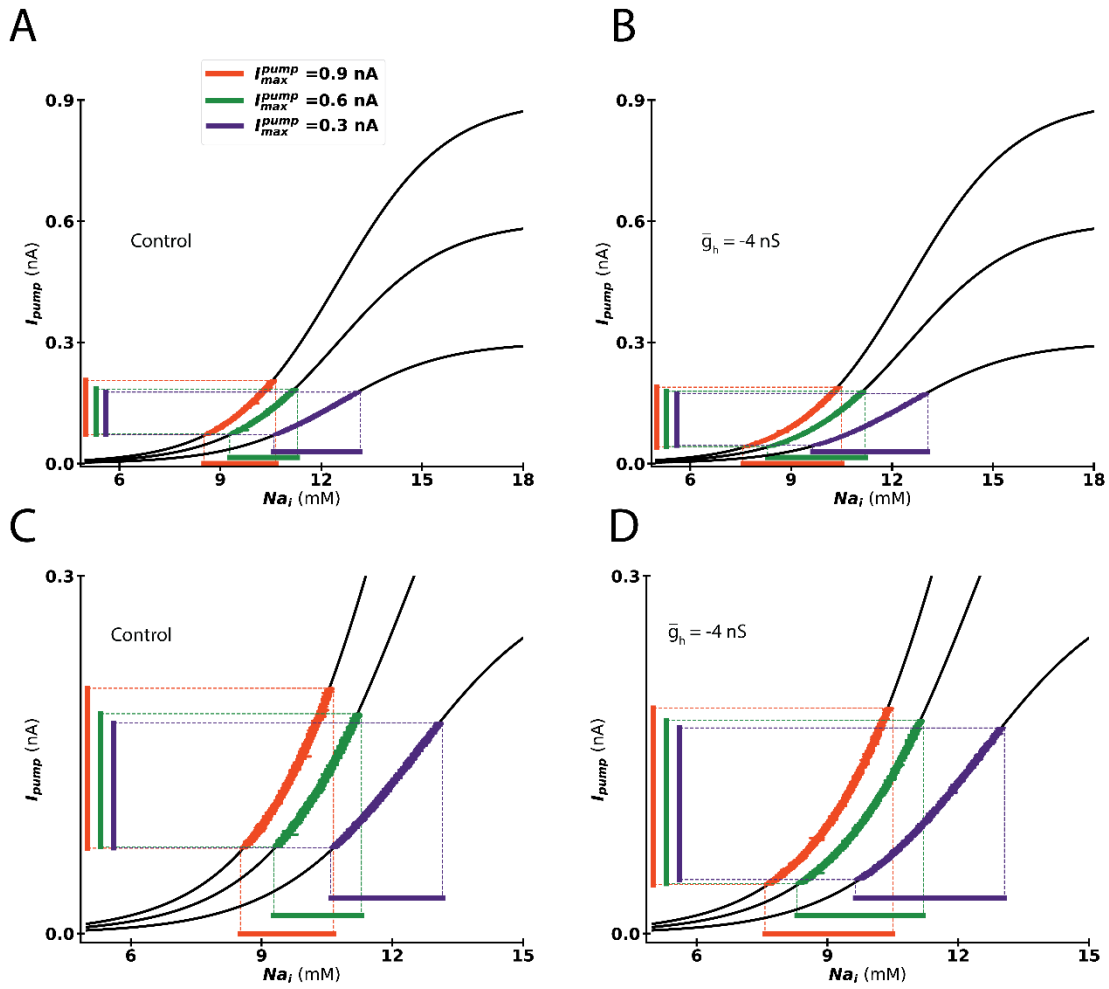

Figure 19. I_{pump} activation curves show that when we subtract I_h ($\bar{g}_h$= -4 nS), I_{pump} and $[Na^+]_i$ amplitudes increase. Data consistent with pharmacological partial I_h blockade 0.5 mM Cs^+ (Figure 22). A: control condition ($\bar{g}_h = 0.0\ nS$), normal size. B: I_h subtraction condition ($\bar{g}_h = -4.0\ nS$), normal size. C: control condition, zoomed-up axis. D: I_h subtraction condition, zoomed-up axis.

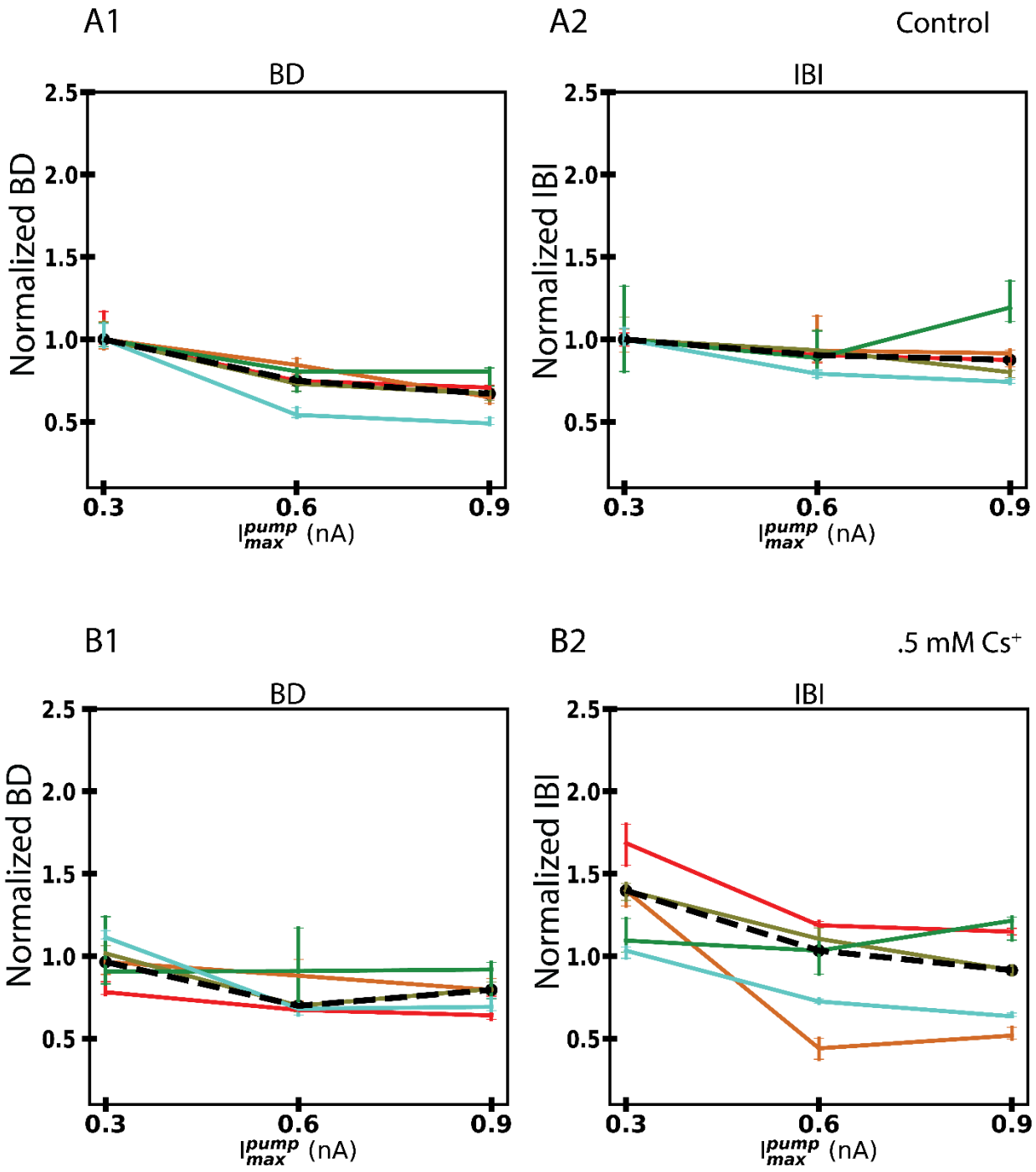

Figure 20. Partial I_h blockade with 0.5 mM Cs^+ lengthened IBI by ≈ 45%, but did not affect BD.

Normalized burst characteristics in normal (control) and 0.5 mM Cs^+ saline. A1: control burst duration, A2: control interburst interval, B1: 0.5 mM Cs^+ burst duration, B2: 0.5 mM Cs^+ interburst interval. Each color represents a different preparation, and the overlying black dashed line is the average across experiments (N=5). The vertical lines are the first and third quantiles of the burst characteristics.

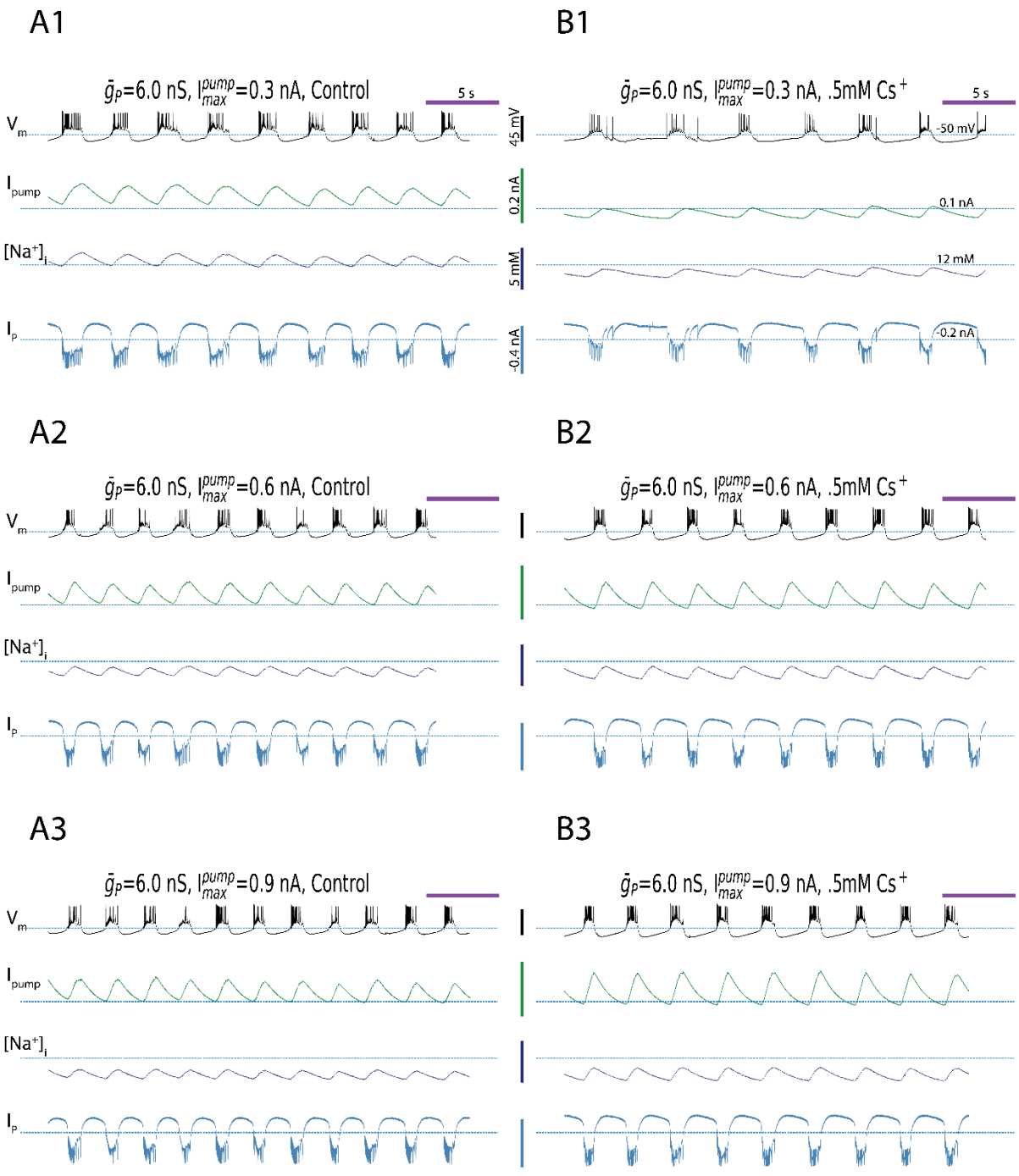

Figure 21. Sample traces showing effect of 0.5 mM Cs^+ lengthening IBI

Experimental data in normal (control) and 0.5 mM Cs^+ saline. These sample traces demonstrate how application of 0.5 mM Cs^+ lengthens IBI. The data correspond to the red curve in Figure 20. A1-3: Voltage, I_{pump}, $[Na^+]_i$, and I_P under control condition (normal saline), three different levels of I_{max}^{pump} 0.3 (A), 0.6 (B), 0.9 (C) nA. B1-3: Experimental traces with partial I_h block (0.5 mM Cs^+)

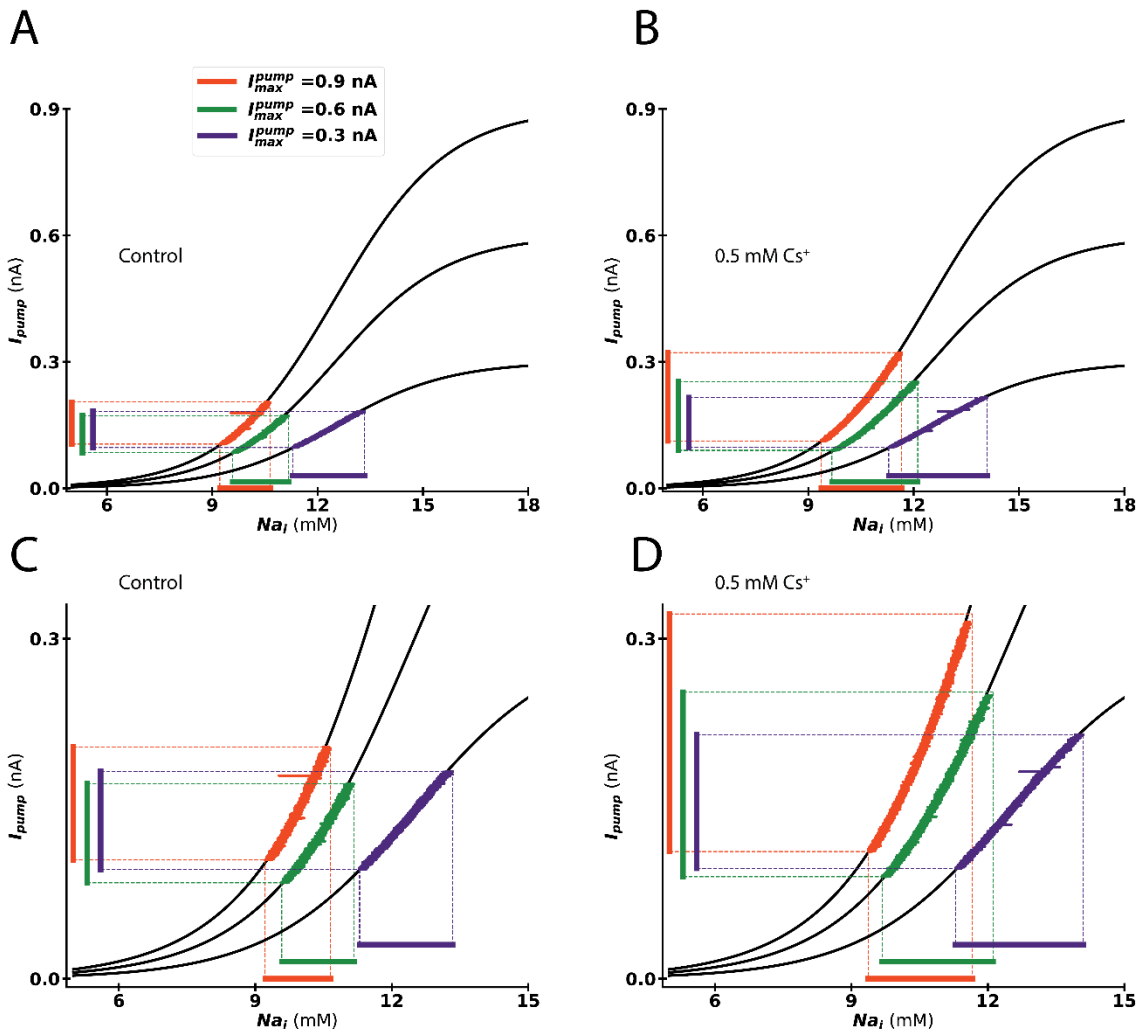

Figure 22. I_{pump} activation curves show that when we partially block I_h (0.5 mM Cs^+), I_{pump} and $[Na^+]_i$ amplitudes increase. Data consistent with dynamic clamp subtraction (Figure 19). A: control condition, normal size. B: I_h partial block condition (0.5 mM Cs^+ saline), normal size. C: control condition, zoomed-up axis. D: : I_h partial block condition (0.5 mM Cs^+ saline), zoomed-up axis.

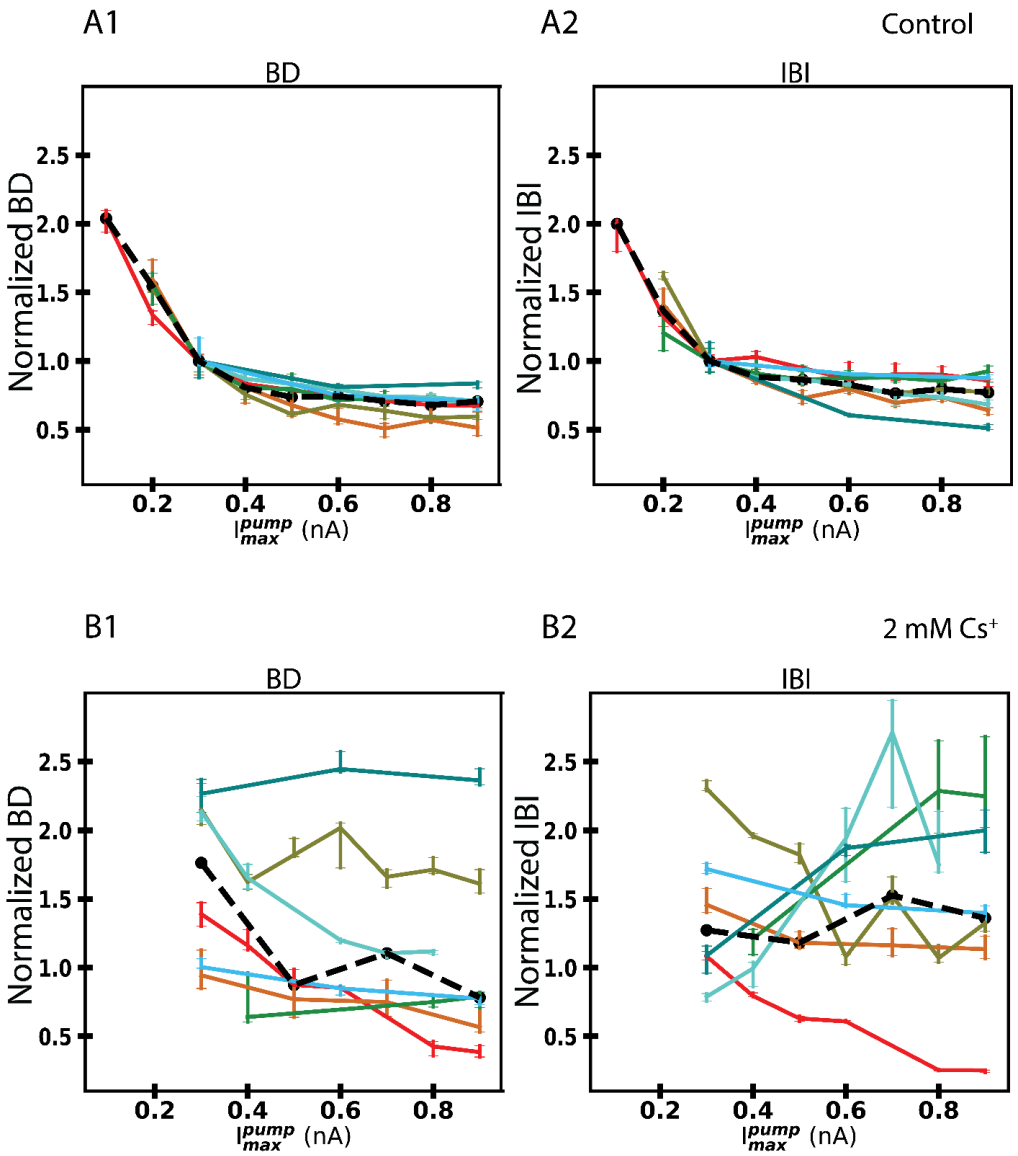

Figure 23. High variability in 2 mM Cs^+ compared to control

Normalized burst characteristics in normal (control) and 2 mM Cs^+ saline. A1: control burst duration, A2: control interburst interval, B1: 2 mM Cs^+ burst duration, B2: 2 mM Cs^+ interburst interval. Each color represents a different preparation, and the overlying black dashed line is the average across experiments (N=7). The horizontal curves are the averaged burst characteristics, and the vertical lines are the first and third quantiles of the burst characteristics. The range of I_{max}^{pump} differs between control and 2 mM Cs^+ conditions because a stronger I_{max}^{pump} was required to ensue rhythmic activity with the higher Cs^+ concentration.

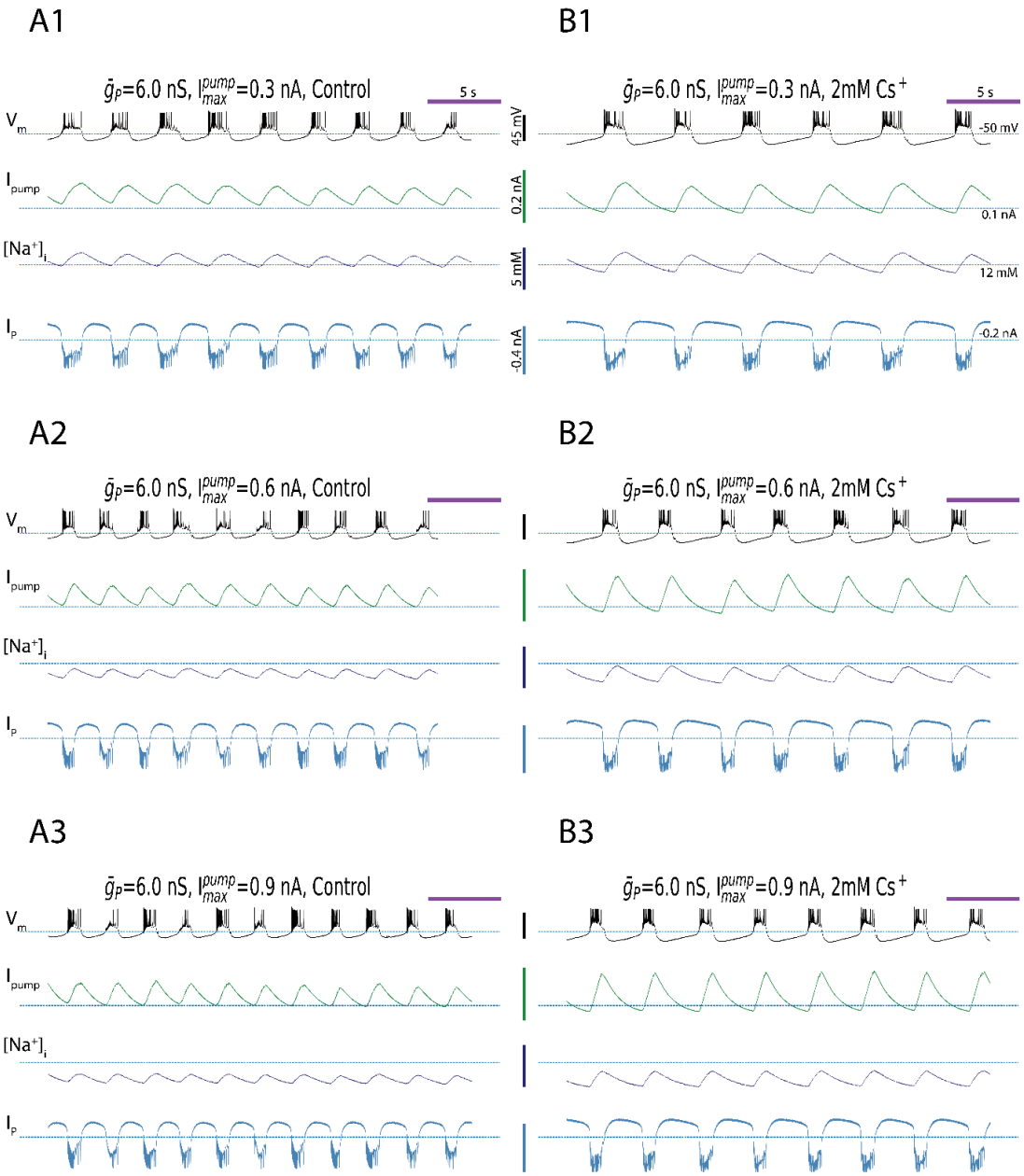

Figure 24. Sample traces with regular rhythmicity in 2 mM Cs^+

Experimental data in normal (control) and 2 mM Cs^+ saline. This sample preparation showed small variability in burst characteristics (<27%). The data correspond to the sky-blue curve in Figure 23. A1-3: three levels of I_{max}^{pump} (0.3, 0.6 and 0.9 nA) in control condition. B1-3: three levels of I_{max}^{pump} in 2mM Cs^+ condition.

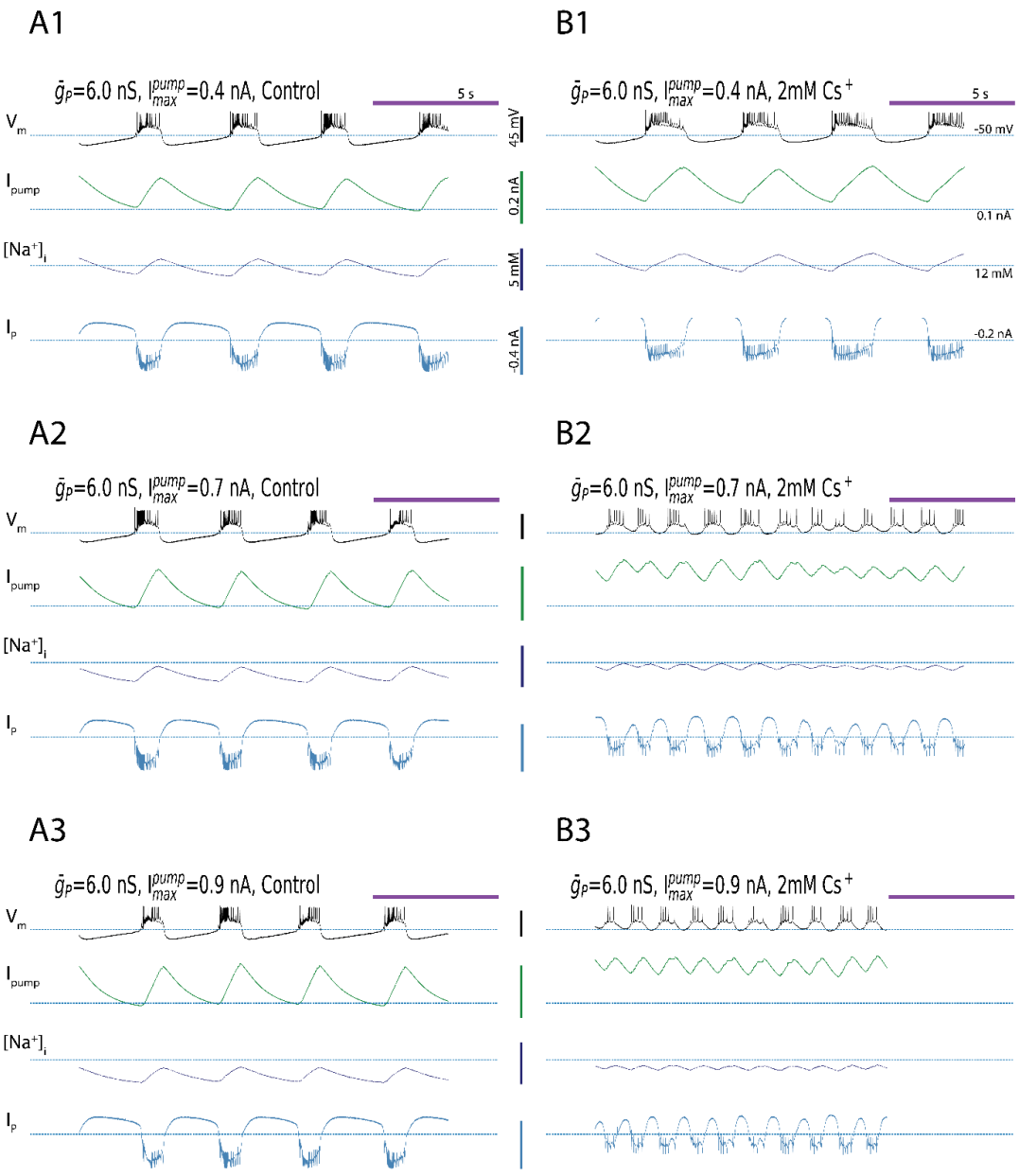

Figure 25. Sample traces with depolarized V_m with 2 mM Cs^+

Experimental data in normal (control) and 2mM Cs^+ saline. This sample preparation showed small variability in burst characteristics (<27%) with I_{max}^{pump} = 0.4 and 0.9 nA, and large variability in burst characteristics (>27%) with I_{max}^{pump} = 0.7 nA. The V_m depolarized in 2 mM Cs^+ saline. The data correspond to the red curve in Figure 23. A1-3: three levels of I_{max}^{pump} (0.3, 0.6 and 0.9 nA) in control condition. B1-3: three levels of I_{max}^{pump} in 2mM Cs^+ condition.

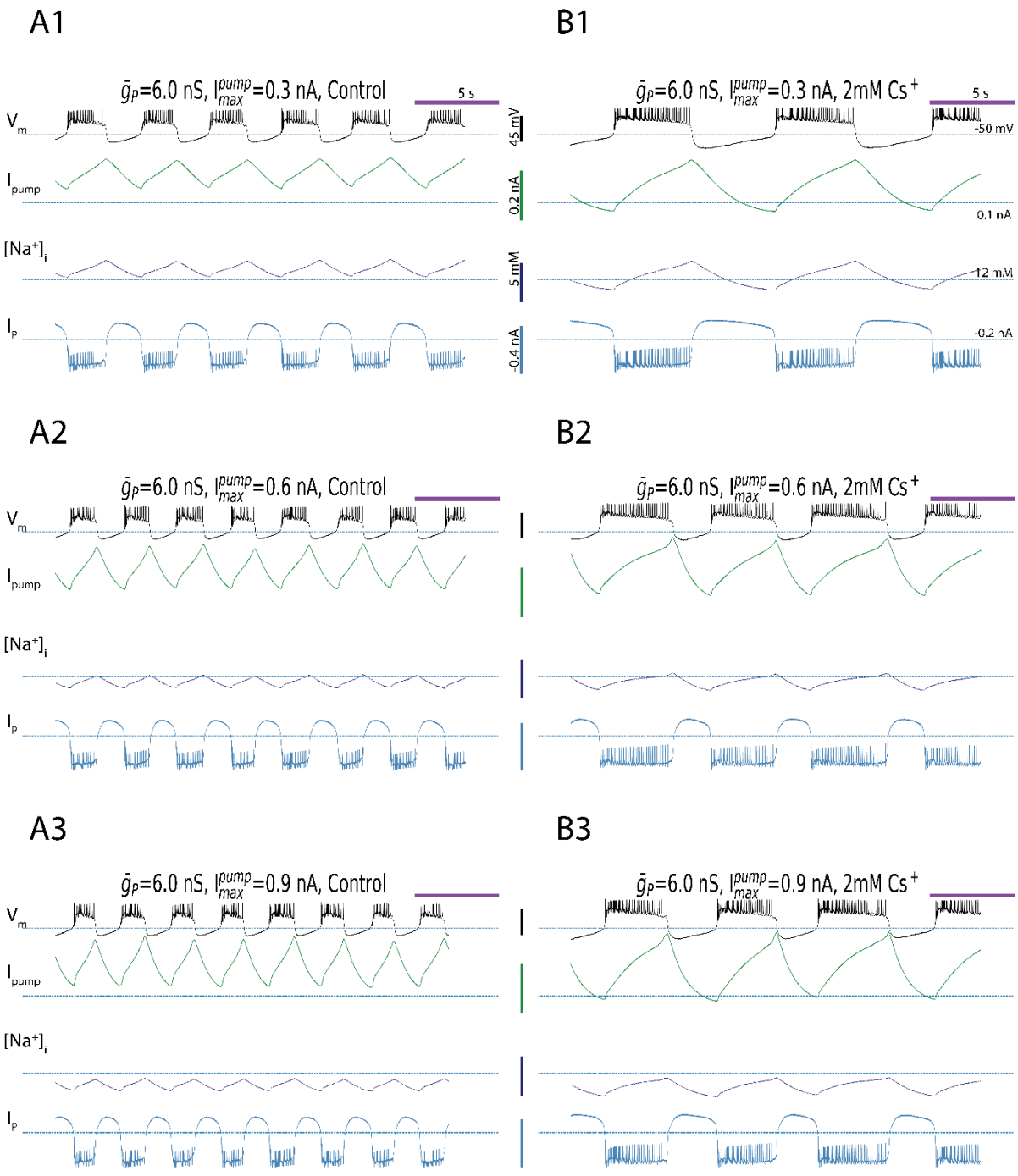

Figure 26. Sample traces with lengthened BD and IBI with 2 mM Cs^+

Experimental data in normal (control) and 2 mM Cs^+ saline. This sample preparation showed small variability (<27%), but BD and IBI lengthened in 2 mM Cs^+. The data correspond to the olive curve in Figure 23. A1-3: three levels of I_{max}^{pump} (0.3, 0.6 and 0.9 nA) in control condition. B1-3: three levels of I_{max}^{pump} in 2mM Cs^+ condition.

5 SYNAPTIC PROPAGATION IN NEURONAL NETWORKS WITH FINITE-SUPPORT SPACE DEPENDENT COUPLING

Preface

This is a copy from our manuscript accepted for publication: Erazo-Toscano, R. J., Osan, R. Synaptic propagation in neuronal networks with finite-support space dependent coupling (accepted). Phys Rev E

5.1 Abstract

Traveling waves of electrical activity are ubiquitous in biological neuronal networks. Traveling waves in the brain are associated with sensory processing, phase coding, and sleep. The neuron and network parameters that determine traveling waves' evolution are synaptic space constant, synaptic conductance, membrane time constant, and synaptic decay time constant. We used an abstract neuron model in a one-dimensional network to investigate the propagation characteristics of traveling wave activity. We formulated a set of evolution equations based on the network connectivity parameters. Using a combination of numerical and analytical approaches, we showed that these traveling waves are stable to a series of perturbations with biological relevance.

5.1.1 Keywords: traveling waves, computer simulation, analytical solution, leaky-integrate-andfire, neuronal networks

5.2 Introduction

Traveling waves of electrical activity are everywhere in the nervous system. For example, cortical brain waves of activity are found in visual (Sato, Nauhaus, & Carandini, 2012; Wanger, , Lippert, Goldschmidt, & Ohl, 2013; Ackman & Crair, 2014; Ackman, Burbridge, & Crair, 2012; Zanos, Mineault, Nasiotis, Guitton, & Pack, 2015; Nauhaus, Busse, Ringach, & Carandini, 2012), olfactory (Compte, Sanchez-Vives, McCormick, & Wang, 2003; Murakami, Kashiwadani,

Kirino, & Mori, 2005), auditory (Reimer, Hubka, Engel, & Kral, 2011; Chrostowski, Yang, Wilson, Bruce, & Becker, 2011), and motor (Belov, Stepanova, & Kolodyazhnyi, 2015; Rubino, Robbins, & Hatsopoulos, 2006) cortices, as well as in the cerebellum (Dipierro & Valdinoci, 2018). Traveling waves may play roles in working memory (Poll & Kilpatrick, 2017), sensory processing, phase coding (Takahashi, Saleh, Penn, & Hatsopoulos, 2011; Bahramisharif et al., 2013), and sleep (Massimini, Huber, Ferrarelli, Hill, & Tononi, 2004). In the hippocampus, traveling waves of synchronization, such as theta and gamma waves, influence spatialtemporal dynamics (Lubenov & Siapas, 2009; H. Zhang & Jacobs, 2015). Sensorimotor systems rely on traveling waves; for example, in mammals, the spinal cord relays afferent and efferent waves(Cuellar et al., 2009), in fish, the cuttlefish skin pigmentation depends on traveling waves to apply camouflage (Laan, Gutnick, Kuba, & Laurent, 2014), in invertebrates, the mollusk olfactory network produces waves when presented with an olfactory stimulus (Kleinfeld et al., 1994). Waves are physical phenomena observed ubiquitously in nervous systems across taxa. Understanding the dynamics of traveling waves bridges a gap between observable phenomena and neuroscience theory.

In the present paper, we investigate traveling waves in a one-dimensional system where the network is a line of neurons. We restrict the analysis of single-spike integrate-and-fire neuronal network activity propagation (J. Zhang & Osan, 2016). Our model assumes that synaptic connections between neurons are space-dependent: the finite support connectivity kernel assumes that synaptic coupling does not decay with distance. One neuron is coupled to all neighbor neurons within one synaptic space constant (synaptic footprint σ). We formulated a system of ordinary differential equations for traveling wave propagation to study the first, second, and potentially higher-order derivatives of firing times as a function of space. The finite support connectivity kernel and the time evolution of spike-dependent synaptic excitation allow the computation of evolution equations in an analytically tractable form. For this work, the

evolution equations of the traveling wave dynamics depend on local dynamics and other parameters with a delayed effect. A key characteristic of our model is that the evolution equations are linear.

The finite support connectivity function is mathematically and conceptually more straightforward than other connectivity functions widely used, such as Gaussian (Osan & Ermentrout, 2002) or exponential decay (J. Zhang & Osan, 2016). However, constant speed wave dynamics in finite support connectivity kernel are more complicated than waves in networks with exponential decay kernel. Specifically, for the exponential kernel, wave acceleration depends quadratically on instantaneous speed plus delayed parameters, a system with straightforward dynamics (J. Zhang & Osan, 2016). The approach used in the present paper allows us to solve equations for speed and acceleration explicitly, and therefore to precisely define how wave speed and acceleration fluctuate as a function of time and space. Overall, the equations of evolution are in excellent agreement with the numerical simulations. The evolution equations predict the traveling wave speed and acceleration based on the network excitability parameters. We further investigated the dynamics of traveling waves with different biologically relevant perturbations; these show that traveling waves are all-or-none events: waves can only propagate at the speed solution determined by the excitability parameters or fail to propagate and die off.

5.3 Wave evolution in Integrate-and-Fire neuron model

Our theoretical framework accurately describes the system of activity propagation in neuronal networks; the framework has simple assumptions about neuronal excitability and network connectivity. In our simulations, for simplicity, we considered one-dimensional systems where all neurons form a continuous line. We initiated traveling wave activities by applying an external current to a subset of neurons in the network labeled the “shocked region.” Consequently, the neurons in the shocked region spiked at the same time (t=0). We assume the

wave propagates only in the positive direction, and we monitor the spiking times of the neurons in the network. As neurons integrate excitatory synaptic inputs, they may reach the firing threshold and spike. Each spike has an excitatory effect to other neurons in the networks, which is usually modeled via a kernel function where nearby neurons receive larger amounts of excitation that vanishes for the ones further apart. Previous research typically examined Gaussian, exponential and finite support kernels (Osan & Ermentrout, 2002; Osan, Curtu, Rubin, & Ermentrout, 2004; Osan, Rubin, Curtu, & Ermentrout, 2003; Osan & Ermentrout, 2001; Ermentrout, 1998; Ermentrout, Rubin, & Osan, 2006; J. Zhang & Osan, 2016), leading to the following equation in $V(x,t)$(Osan et al., 2003):

$$\tau \frac{\partial V}{\partial t} = -V + I_{syn} = -V + g_{syn} \int_D J(|x-y|) \sum_k \alpha\big(t - t_k(y)\big) dy \qquad (1)$$

where$\alpha(t) = e^{-\frac{t}{\tau_2}} H(t)$

Here $t_k(x)$ is the k^{th} spike of the neuron at location x and

$$J(x,y) = J(|x-y|) = \frac{1}{\sigma} H(\sigma - |x-y|)$$

with H being the Heaviside function, $H(x) = 1$ if $x > 0$ and 0 otherwise. To permit propagation we need to have the sypatic integration constant τ_1 be smaller than the decay time of excitation τ_2, that is, $0 < \tau_1 < \tau_2$, and synaptic footprint to be positive, that is, $\sigma > 0$.

Here, we consider traveling waves solutions, therefore the spiking times of neurons are a monotonic function of their position 'x' within the network. Furthermore, we restrict the analysis to single-spike solutions to facilitate analytical results. Therefore, instead of multiple firing times $t_k(y)$, one only has single spikes across the network, that is, $t(y) = t_1(y)$. Consequently, for a single-spike wave, we can now obtain the integral-form equivalent:

$$V(x,t) = \frac{g_{syn}}{1 - \frac{\tau_1}{\tau_2}} \int_{x-\sigma}^{x} J(x,y) A(t - t(y)) dy \qquad (2)$$

where

$$A(t) = (e^{-\frac{t}{\tau_2}} - e^{-\frac{t}{\tau_1}})H(t)$$

The neuronal network model Eq. (2) describes membrane potential (V) as a function of time and space-dependent kernel multiplied by network excitability parameters: g_{syn}, σ, τ_1, τ_2 (synaptic conductance, synaptic space constant, membrane time constant, and synaptic decay time constant). The neurons are set to spike when V = V_T, and this crossing of the threshold results in additional excitation sent by the spiking neuron to other parts of the neural tissue. The parameters of the finite support kernel, 'x' and '$x - \sigma$', define the boundaries of the integral. Integrating Eq. (2), the evolution of the wavefront can now be computed as the moment $t(x)$ when the neuron a position x spikes, that is, $V(x,t(x)) = V_T$, using the following equation:

$$V\big(x,t(x)\big) = V_T = \frac{\frac{g_{syn}}{\sigma}}{1-\frac{\tau_1}{\tau_2}}\Big(I_2\big(x,t(x)\big) - I_1\big(x,t(x)\big)\Big)$$

$$= \frac{\frac{g_{syn}}{\sigma}}{-\frac{\tau_1}{\tau_2}}\left(e^{-\frac{-t(x)}{\tau_2}}dy\int_{x-\sigma}^{x} e^{\frac{t(y)}{\tau_2}}dy - e^{\frac{-t(x)}{\tau_1}}\int_{x-\sigma}^{x} e^{\frac{t(y)}{\tau_1}}dy\right) \quad (3)$$

where:

$$I_i(x,t(x)) = e^{-\frac{t(x)}{\tau_i}}\int_{x-\sigma}^{x} dy e^{\frac{t(y)}{\tau_i}}, i = 1,2$$

Taking the first derivative of Eq. (3), we get the traveling wave speed as a function of integrals I_1 and I_2:

$$\frac{I_1}{c\tau_1} - \frac{I_2}{c\tau_2} + e^{-\frac{t(x)-t(x-\sigma)}{\tau_1}} - e^{-\frac{t(x)-t(x-\sigma)}{\tau_2}} = 0 \quad (4)$$

Taking the second derivative of Eq. (3), we obtain:

$$\frac{dt}{dx}\left(-\frac{1}{\tau_2}+\frac{e^{-\frac{t(x)-t(x-\sigma)}{\tau_2}}}{\tau_2}+\frac{1}{\tau_1}-\frac{e^{-\frac{t(x)-t(x-\sigma)}{\tau_1}}}{\tau_1}\right)+\left(\frac{dt}{dx}-\frac{dt(x-\sigma)}{dx}\right)\left(\frac{e^{-\frac{t(x)-t(x-\sigma)}{\tau_2}}}{\tau_2}-\frac{e^{-\frac{t(x)-t(x-\sigma)}{\tau_1}}}{\tau_1}\right)+$$

$$\frac{d^2t}{dx^2}\left(-\frac{1}{\tau_2}I_2+\frac{1}{\tau_1}I_1\right)+\left(\frac{dt}{dx}\right)^2\left(\frac{1}{\tau_2^2}I_2-\frac{1}{\tau_1^2}I_1\right)=0 \quad (5)$$

In Eq. (5) we can determine $\frac{d^2t}{dx^2}$ as a function of speed and convert $\frac{d^2t}{dx^2}$ into the instantaneous acceleration. We used the same relationship from Zhang and Osan(2016):

$$a(x)=\frac{d^2x}{dt^2}=-c^3\frac{d^2t}{dx^2}$$

The equations of evolution connect the wave speed and acceleration in a similar way to the ones from the exponential kernel (J. Zhang & Osan, 2016), but with some major differences that will become apparent later on. We now have a system of two equations where the unknowns are the speed $c(x)$, acceleration $a(x)$, $I_1(x,t(x))$ and $I_2(x,t(x))$. Unfortunately for these equations we cannot solve the system explicitly, because the network has memory so that the wave acceleration at 'x' depends not only on speed at x, but also on the speed at '$x-\sigma$' and on the difference between the spiking times at these two different spatial locations $\Delta t(x)$. The instantaneous acceleration of the wave propagation then becomes:

$$a=\left(\frac{1}{e^{-\frac{\Delta t(x)}{\tau_2}}-e^{-\frac{\Delta t(x)}{\tau_1}}}\right)\left[\frac{V_T\sigma}{g_{syn}\tau_2}\left(\frac{1}{\tau_2}-\frac{1}{\tau_1}\right)+c\left(\frac{1}{\tau_1}+\frac{1}{\tau_2}\right)\left(e^{-\frac{\Delta t(x)}{\tau_1}}-e^{-\frac{\Delta t(x)}{\tau_2}}\right)+c\left(\frac{1}{\tau_1}-\frac{1}{\tau_2}\right)+\right.$$

$$\left.\left(2c-\frac{c^2}{c(x-\sigma)}\right)\left(\frac{e^{-\frac{\Delta t(x)}{\tau_2}}}{\tau_2}-\frac{e^{-\frac{\Delta t(x)}{\tau_1}}}{\tau_1}\right)\right] \quad (6)$$

The theoretical wave speed and acceleration are described by Eqs. (6) and (4). The objective of our derivations was to accurately describe the wave propagation based on the excitability parameters, and on previous network activity. The system of equations has the following unknown variables: Eq. (4) has $t(x)$ and $t(x-\sigma)$, the spike time of neuron at the location 'x' and

spike time of neuron at the location '$x - \sigma$'; Eq. (6) has $c(x)$ and $c(x - \sigma)$, the speed of the wave at the location 'x' and the speed at the location '$x - \sigma$.'

To confirm our approach, we first conducted simulations to compute the numerical wave speed and acceleration (Figure 27). For numerical simulations, neurons in the network are located adjacent to one another and separated by a discretization constant δ. We performed simulations varying the value of the discretization constant δ. Table 1 summarizes percentage change between numerical simulations with varying magnitudes of δ, and the percentage change between theoretical and numerical speeds.

δ	numeric speed	numeric relative change	theoretic speed	theoretic relative to numeric change
$5 \cdot 10^{-5}$	6.984	-	6.984	0.007%
$1 \cdot 10^{-4}$	6.984	0.006%	6.984	0.012%
$5 \cdot 10^{-4}$	6.981	0.042%	6.984	0.053%
$1 \cdot 10^{-3}$	6.977	0.052%	6.984	0.105%
$5 \cdot 10^{-3}$	6.948	0.416%	6.984	0.519%
$1 \cdot 10^{-2}$	6.912	0.521%	6.984	1.038%
$5 \cdot 10^{-2}$	6.622	4.197%	6.984	5.191%

Table 8. Speed and the discretization constant

5.4 Constant speed traveling wave

We further explored the equations of evolution to estimate the speed of the traveling wave. We assume two intuitive features: (1) self-propagating traveling waves move at a constant

speed, and (2) traveling waves that do not self-propagate eventually extinguish. The acceleration of constant speed waves is zero; therefore solving Eq. (6) when a=0 yields the consistency equation (Eq. (7)), which describes neuron membrane potential as a function of traveling wave speed:

$$\sigma V_T \frac{1-\frac{\tau_1}{\tau_2}}{g_{syn}} = c\left(\tau_2 - \tau_1 - \tau_2 e^{-\frac{\sigma}{c\tau_2}} + \tau_1 e^{-\frac{\sigma}{c\tau_1}}\right) \quad (7)$$

For a traveling wave that arrives from -∞ to a location 'x', and with speed c, one can compute the corresponding voltage. If the voltage is V_T then the solution c is consistent with Eq. (7); otherwise, a traveling wave with speed c cannot exist.

The accuracy of the equations of evolution allows us to estimate the solutions of traveling wave propagation. Figure 28 illustrates that c_{fast} and c_{slow} are located at the intersection between V_T and V(c). Figure 28 also shows how the wave acceleration and speed oscillate while the wave evolves towards the stable state of activity propagation, where a=0 and c=c_{fast}.

Our numerical simulations demonstrate that traveling waves are all-or-none phenomena, determined by neuronal and network connectivity properties. Parameters g_{syn} (Figure 29), V_T (Figure 30), σ (data not shown), τ_1 (data not shown), and τ_2 (data not shown) control traveling wave speed, and thus varying any of these parameters beyond a critical value determines wave propagation or failure. Figure 29 shows that as g_{syn} decreases, c_{fast} and c_{slow} become closer in value before disappearing, and diverge asymptotically as g_{syn} increases. Figure 30 shows that as V_T increases the wave speed decreases. While Figure 28 shows that there is a speed at which a wave can induce a maximum V_{max} voltage, Figure 30 shows that if $V_T > V_{max}$, the wave fails to propagate. Standard bifurcation analysis is not compatible with the system at hand, because perturbation of the constant speed solutions does not decay back to steady states, as showed by our results in the upcoming sections. In conclusion, our simulations determined that waves are all-or-none events determined by the excitability parameters.

5.5 Perturbation-based stability analysis

First, we established the existence of constant speed traveling waves in neuronal networks of Integrate-and-Fire neurons with finite support connectivity kernel. According to the consistency Eq. (7), the threshold V_T constrains the neurons' membrane potential and traveling wave speed. Figure 28 illustrates that above V_T activity propagation generates additional excitation, and below V_T the traveling wave does not generate enough excitation. If the wave travels faster than c_{slow} but slower than c_{fast}, the wave builds a surplus of excitation in the network. In this case, the membrane voltage is higher than the threshold voltage (Figure 28, left panel). The surplus of excitation will speed up the activity propagation until the wave speed reaches c_{fast}. If the wave is traveling faster than c_{fast}, the network does not have the resources to sustain activity propagation, and the voltage falls lower than the threshold. Then, the wave slows down and settles at c_{fast} because, in c_{fast}, the voltage equals V_T. If the wave travels slower than c_{slow}, voltage is below the threshold, and it does not generate enough energy to self-sustain; the wave speed slows down to zero (propagation failure). We ran series of simulations that support this notion; numerically, c_{fast} is stable, and c_{slow} is unstable. Next, we use a series of approaches to investigate the stability of the constant speed traveling wave. Here, the stable speed solution (c_{fast}) is computed from Eq. (7) as well as determined from numerical simulations, and it represents the speed of the constant speed traveling wave.

5.5.1 An analytical argument for the stability of traveling wave speed

We introduced a small parameter ϵ perturbation at t=0. This theoretical perturbation consisted of imposed initial conditions that force the wave to travel from x = -∞ to x= 0 at a constant speed faster than c_{fast}. The initial wave speed is defined by

$$c0 = cfast + c1 = cfast + \epsilon \cdot cfast$$

where ,$c_1 \ll c_{fast}$, with a typical value for $\epsilon \approx 0.01$. In this context, the consistency equation becomes:

$$c_0\left(\tau_2-\tau_1-\tau_2 e^{-\frac{\sigma}{c_0\tau_2}}+\tau_1 e^{-\frac{\sigma}{c_0\tau_1}}\right)=\sigma\frac{1-\frac{\tau_1}{\tau_2}}{g_{syn}}(V_T+\epsilon V_1) \tag{8}$$

For small values of the parameter ϵ, we can look at solutions that are correct in the first order of ϵ by linearizing Eq. (8) to obtain the first order correction in voltage for $V_0 = V_T + \epsilon \cdot V_1$:

$$\epsilon V_1=\frac{g_{syn}\cdot c_1}{\left(1-\frac{\tau_1}{\tau_2}\right)}\cdot\left(-\frac{e^{-\frac{\sigma}{c_{fast}\tau_2}}-e^{-\frac{\sigma}{c_{fast}\tau_1}}}{c_{fast}}+\frac{\tau_2-\tau_1-\left(\tau_2 e^{-\frac{\sigma}{c_{fast}\tau_2}}-\tau_1 e^{-\frac{\sigma}{c_{fast}\tau_1}}\right)}{\sigma}\right) \tag{9}$$

Intuitively, this means that since the wave is traveling faster than c_{fast}, the neuron at position $x = 0$ will not cross the threshold at $t = 0$, stopping the propagation of the wave temporarily. Therefore, the sign of V_1 is negative and the neuron needs more time to integrate the synaptic currents before potentially crossing the threshold and spiking at a later time, allowing for the wave propagation to restart. The computation of this delay is done next.

In addition to the correction in voltage, the synaptic current also has an order ϵ correction as $I_0 + \epsilon I_1$, with its derivation as follows:

$$I(x,t)=g_{syn}\int_{x-\sigma}^{x}e^{-\frac{t-t(y)}{\tau_2}}dy \tag{10}$$

Since firing times are described by the constant speed traveling wave, it follows that $t(y) = y/c_0$, and:

$$I(0^+,t)=I_{syn}\cdot e^{-\frac{t}{\tau_2}}=g_{syn}\int_{-\sigma}^{0}e^{\frac{y}{c_0\cdot\tau_2}}dy\cdot e^{-\frac{t}{\tau_2}} \tag{11}$$

$$I_{syn}=I_0+\epsilon\cdot I_1=\frac{g_{syn}}{\sigma}\left(\left(c_{fast}+c_1\right)\cdot\tau_2\cdot\left(1-e^{-\frac{\sigma}{\left(c_{fast}+c_1\right)\tau_2}}\right)\right) \tag{12}$$

Finally, we obtain

$$I_0 = \frac{g_{syn}}{\sigma} \cdot \left(c_{fast} \cdot \tau_2 \cdot \left(1 - e^{-\frac{\sigma}{c_{fast} \cdot \tau_2}} \right) \right) \epsilon \cdot I_1 = -c_1 \cdot g_{syn} \left(\frac{e^{-\frac{\sigma}{c_{fast} \cdot \tau_2}}}{c_{fast}} - \tau_2 \frac{1 - e^{-\frac{\sigma}{c_{fast} \cdot \tau_2}}}{\sigma} \right) \quad (13)$$

The voltage evolution at $x = 0$ follows this explicit formula:

$$V(t) = V_0 \cdot e^{-\frac{-t}{\tau_1}} + \frac{I_{syn}}{1 - \frac{\tau_1}{\tau_2}} \cdot \left(e^{-\frac{t}{\tau_2}} - e^{-\frac{t}{\tau_1}} \right) \quad (14)$$

We can compute the delay in firing for the neuron at $x = 0^+$ by computing the moment when $V(t) = V_T$ in the previous equation. Again, by focusing only on Taylor expansion up to linear terms, we obtain the following expression for the delay $\Delta t = t_0$:

$$t_0 = \frac{\epsilon V_1}{\frac{V_T}{\tau_1} - \frac{g_{syn}\tau_2}{\sigma \cdot (1 - \frac{\tau_1}{\tau_2})} c_{fast} (1 - e^{-\frac{\sigma}{c_{fast}\tau_2}}) (\frac{1}{\tau_1} - \frac{1}{\tau_2})} \quad (15)$$

To summarize, we investigated how the traveling wave behaved near x= 0. We determined that there is a delay once the perturbation is removed. The delay is a function of perturbation speed c_1 and network parameters. In addition to the delay to restart the wave at $x = 0$, namely t_0, our methods also allow us to estimate the wave characteristics speed. By using the fact that prior to $x = 0$ we have constant propagation with $t(y) = y/c_0$, we can now use Eqs. (5) and (6) to obtain the restarting speed ($c(0^+)$) and acceleration acceleration ($a(0^+)$) at $x = 0^+$.

$$c(0^+) = -c_{fast} \frac{e^{-\frac{t_0}{\tau_2}} \left(1 - e^{-\frac{\sigma}{c_{fast}\tau_2}} \right) - e^{-\frac{t_0}{\tau_1}} \left(1 - e^{-\frac{\sigma}{c_{fast}\tau_1}} \right)}{e^{-\frac{t_0}{\tau_2}} e^{-\frac{\sigma}{c_{fast}\tau_2}} - e^{-\frac{t_0}{\tau_1}} e^{-\frac{\sigma}{c_{fast}\tau_1}}} \quad (16)$$

$$a(0^+) = \left(\frac{1}{e^{\frac{\sigma+c_{fast}t_0}{\tau_2}} - e^{\frac{\sigma+c_{fast}t_0}{\tau_1}}}\right)\left[\frac{V_T\sigma}{g_{syn}\tau_2}\left(\frac{1}{\tau_2}-\frac{1}{\tau_1}\right) + c(0^+)\left(\frac{1}{\tau_1}+\frac{1}{\tau_2}\right)\left(e^{-\frac{\sigma+c_{fast}t_0}{c_{fast}\tau_1}} - e^{-\frac{\sigma+c_{fast}t_0}{c_{fast}\tau_2}}\right) + c(0^+)\left(\frac{1}{\tau_1}-\frac{1}{\tau_2}\right) + \left(2c(0^+) - \frac{c(0^+)^2}{c_{fast}}\right)\left(\frac{e^{-\frac{\sigma+c_{fast}t_0}{c_{fast}\tau_2}}}{\tau_2} - \frac{e^{-\frac{\sigma+c_{fast}t_0}{c_{fast}\tau_1}}}{\tau_1}\right)\right] \quad (17)$$

We now have the initial conditions at $x = 0^+$ to use in conjunction with the system of equations Eq. (5) and Eq. (6) to determine the wave evolution without resorting to full network numerical simulations. Figure 31 shows that this approach is in excellent agreement with the numerical simulations from perturbation-imposed initial conditions where the wave propagates from x= -∞ to x=0 at speed greater than c_{fast}. The perturbation is removed at x=0, and the wave further evolves due to the dynamics determined by the neuron and network parameters. Not surprisingly, the traveling wave stopped and then restarted with a lower speed than $c_0 = c_{fast} + c_1$, but at a velocity still higher than c_{fast}.

Together, Figure 27 and Figure 31 demonstrate that the theoretical framework is in excellent agreement with the numerical simulations. However, as mentioned earlier in the text, the accuracy of the equations depends on the magnitude of ϵ. How accurate are the delay, initial speed, and initial acceleration of the wave from Eqs? (15) (16), and (17) compared to their numerical counterparts? We computed series of simulations with varying magnitudes of ϵ ranging from 0.001 to 0.1, as shown in Figure 32. We performed linear regression and polynomial regression for these data. The linear and quadratic regressions we performed were both quite accurate, with $R^2 > 0.99$, with marginal improvements by the quadratic method in some cases.

Overall, these results support an argument for the stability of the waves as follows. If the wave travels with a speed c that is faster than c_{fast} until $x = 0$, the tissue at $x > 0$ has a voltage $V < V_T$ at $t = 0$. Consequently, the firing stops for t_0^+ to allow the neuron at $x = 0$ to further increase its

voltage and spike at a later time. Due to additional excitation in the system, the waves still restart with a new speed $c_{fast} < c_{new} < c$, that is, the wave still travels faster than needed for stability. As shown by results in Figure 32, acceleration a_0^+ is negative for all values of ϵ considered here, effectively acting as a restoring dynamic toward the constant speed traveling wave.

The discontinuity at the spatial boundary of the finite support connectivity kernel complicates solving analytically the evolution of the wave. In contrast to the exponential connectivity kernel where the absence of discontinuity within the connectivity kernel (one-way propagation) allows for explicit solutions (J. Zhang & Osan, 2016).

While have examined perturbations with speeds exceeding c_{fast}, same analysis cannot be performed in a similar way for $c < c_{fast}$ due to the following reasons. The current framework assumes that propagation is monotonic from -∞ to +∞. Waves can accelerate or decelerate but not jump over any region. There is a delay for the fast wave case because the neuron at position $x = 0^+$ needs time to integrate inputs before firing. But if we implement a slower wave perturbation ($-\epsilon$), the neuron at position $x = 0^+$ fires before the wave arrives and creates a second traveling wavefront. The equations and implementation of non-monotonic propagating waves with two wavefronts are beyond this paper's scope.

5.5.2 Traveling wave stability: the effect of synaptic perturbations such as synaptic inhomogeneity, demyelination, and cell death

We investigate how perturbations to the microstructure of the neuronal network affect traveling wave propagation. In the synaptic inhomogeneity perturbation, the synaptic coupling parameter (g_{syn}) is allowed to oscillate sinusoidally as a function of space in a subsection of the network; the result is a sudden increase followed by a sharp decrease in synaptic conductance (Figure 33), which is one period of the sine function. In the demyelination perturbation, the synaptic coupling parameter decreases in a subsection of the network; here, the synaptic

coupling is relatively weak (Figure 34). Lastly, in the cell death perturbation, the synaptic coupling is completely turned off for a subsection of the network; it emulates the network's activity when the coupled neurons do not spike (Figure 35). If the subsection is not too large activity can jump over the dead region due to the longer-range connections that can extend over this region. We investigate how the traveling wave speed depends on the synaptic coupling parameter and space constant. Our results are numerical evidence of the stability of the traveling wave solution.

5.5.2.1 Synaptic inhomogeneity perturbation

Synaptic inhomogeneity refers to the media microstructure; it represents periodic variation of strenghts of synaptic coupling. We assume g_{syn} is equal throughout the network, except for one synaptic space constant (σ), where g_{syn} oscillates sinusoidally with wavelength $\lambda = \sigma$. Here, the connections between neurons are stronger, followed by weaker connections than baseline (Figure 33). These synaptic coupling patterns are common in neuronal networks where neurons from different populations co-exist, such as optical preference columns in the visual cortex and the barrel cortex (Kandel et al., 2000). In our simulations, these synaptic arrangements show interesting transient phenomena while also supporting the stability of the traveling wave speed c_{fast} (Figure 33).

The traveling wave propagated at a constant speed before the perturbation. The wave speed oscillated at the perturbation location; the speed and acceleration drifted away from the stable baseline state. After removing the perturbation, the wave speed continued to oscillate. The oscillations damped while approaching c_{fast} (Figure 33); while the wave speed approached c_{fast}, the wave acceleration approached zero. The wave reaches a constant speed when speed equals c_{fast} and acceleration is 0. Interestingly, the effects of the perturbation are maximal during the next two synaptic footprints to the right of the perturbation region.

5.5.2.2 Demyelination perturbation

Synaptic demyelination is a neurodegenerative condition in which neurons lose their myelin sheath. Demyelination may be caused by aging (Adinolfi, Yamuy, Morales, & Chase, 1991), Huntington's disease (Phillips et al., 2013), and ALS (Kang et al., 2013). We modeled the effects of demyelination as a quadratic function; within two synaptic space constants (σ), the synaptic coupling between neurons (g_{syn}) sharply and continuously decreases until reaching a minimum value and returns to the baseline value (Figure 34). In the demyelination perturbation, the strength of the neuronal connections decreases dramatically in a network subsection. The decrease in g_{syn} synaptic coupling represents the decay of synaptic coupling is common in demyelinating and neurodegenerative diseases (Kang et al., 2013; Phillips et al., 2013; Adinolfi et al., 1991). We performed simulations to investigate the traveling wave speed and acceleration with varying magnitudes of perturbations. Consistently with previous sections of the paper, our results strongly suggest that for this class of models, neuronal traveling wave phenomena are all-or-none events (Figure 34).

The traveling wave propagated at a constant speed before reaching the location of the perturbation. At the perturbation location, g_{syn} decays drastically for one σ; in the subsequent σ, g_{syn} rapidly recovers baseline (Figure 34). The wave traveled at a constant speed when it arrived at the perturbation location. Our simulations showed a critical value of ϵ (Figure 34) that separated the waves that recovered from those that died off. The waves that recovered after removing the perturbation oscillated while approaching c_{fast}; however, the waves that died off approached c_{slow} (Figure 34). In conclusion, we demonstrated a small parameter change that determines the dynamics of wave evolution; when $\epsilon < \epsilon_{critical}$, the wave recovers, and when $\epsilon > \epsilon_{critical}$, the wave dies off.

5.5.2.3 Cell-death perturbation

We assume synaptic coupling is equal throughout the network, except for a subsection where neurons are not coupled and do not spike. As the wave travels from -∞ toward positive values for 'x' it encounters a non-conducting gap for a finite region, then synaptic coupling returns to baseline values. The gap's size is determined by the ratio $\alpha \cdot \sigma$, where the value of α ranges from 0 to 1. In the cell-death perturbation, a gap of synaptic non-conductance represents the area of dead neurons. The perturbation methods model acute events of neural cell death that may result from cerebral infarction (Ferrer & Planas, 2003) or traumatic brain injury (Raghupathi, 2004; Rink et al., 1995); these sorts of insults produce neuronal cell death at the location of the accident, while adjacent neurons may survive the insult.

Similar to the other section results, the outcomes from the cell-death perturbation support the idea that constant speed neural waves are all-or-none events (Figure 35). Waves typically recover from smaller non-conducting gaps; the wave speed oscillates transiently but eventually settles back to a constant speed value, namely c_{fast} ($\alpha < \alpha_{critical}$, Figure 35, green). However, larger perturbations break traveling wave propagation ($\alpha >= \alpha_{critical}$, Figure 35, magenta). The traveling wave's speed is slower than c_{fast} right where synaptic coupling returns to baseline; the speed after the break decreases monotonically as α grows and approaches $\alpha_{critical}$.
Computer simulations determined the smallest $\alpha_{critical} \cdot \sigma$ gap that breaks traveling wave propagation (Figure 36). $\alpha_{critical}$ represents the ratio of the synaptic space constant σ in the borderline between traveling wave propagation and failure. Simulations with varying values of g_{syn} demonstrate that $\alpha_{critical}$ is relatively low at low synaptic conductances, but $\alpha_{critical}$ increases rapidly, and approaches asymptotically to σ as synaptic coupling grows. Indicating that as excitation in the network increases propagation failure is less likely to be triggered, as it requires larger perturbations to suppress the activity in some propagation regions. Figure 36shows an accurate fit between $\alpha_{critical}(g_{syn})$ and the power function.

5.6 Conclusions and future directions

We present an extensive analysis of traveling waves in neuronal networks with finite support synaptic coupling. In neuronal networks with exponential or Gaussian connectivity kernels (J. Zhang & Osan, 2016), neurons are connected to neighbors up to infinity, although the connections decay with distance. In contrast, these model networks represent a simplification in network topology by assuming that synapses strictly space dependent. Connections are only between neighboring neurons within a synaptic footprint σ, and zero elsewhere; this simplification is based on the assumption that synaptic coupling is strictly space dependent. However, the finite support kernel introduces discontinuities in the network. The finite support neuronal network proposes a more straightforward mathematical function and biological structure compared to other connectivity functions, such as Gaussian or exponential. Despite the inherent simplicity in the finite support function, the mathematical model is complicated and has no analytical solutions. However, we managed to describe wave propagation as a set of evolution equations that predict wave dynamics without the need to run the entire computer simulation Eqs. (4),(6), (16), and (17).

In order to investigate the stability of the wave, we presented a number of perturbations. First, a traveling wave coming from -∞ to 0 at a constant speed $c_0 = c_{fast} + \epsilon c_{fast}$. Simulations and analytical studies show there is a delay to spike once the perturbation is removed. We compute the delay, the speed, and acceleration after the break, Eqs. (15) (16), and (17)) respectively. We then presented perturbations relevant to a biological context, resembling effects of demyelinating disorders and cell death. Demyelinating disorders were presented as continuous perturbations (Figure 34) in the topology of parameter g_{syn} in a subsection the network. These results were consistent with the notion that synaptic coupling facilitates traveling wave propagation: in the cases the introduced perturbation increased coupling, the wave accelerated; and in the cases the perturbation decreased coupling, the wave decelerated (Figure 7). If the

wave decelerates slower than c_{slow}, propagation fails to continue (Figure 34, Figure 35). The last perturbation we presented was a non-conducting gap, which resembles a small section of "dead tissue" (Figure 35). The gap was defined as $gap = \alpha\sigma$ and represented the ratio $gap = \alpha * \sigma$. For any given g_{syn} there is a corresponding critical value $\epsilon_{critical}$ between activity propagation and failure (Figure 36). The demyelination and dead tissue perturbations (Figure 34and Figure 35, respectively) show remarkable stability of the system because despite how much the perturbation decelerated the wave, all the waves that continued to propagate evolved back to the steady state c_{fast}.

Altogether, the present work demonstrates waves respond robustly in neuronal networks with finite support coupling and that network parameters influence traveling wave propagating speed. Waves in neuroscience are ubiquitous, and unraveling population dynamics can inform us of underlying mechanisms that give rise to neuronal function and dysfunction. For example, the inhomogeneity perturbation (Figure 33) shows how speed of neuronal activity can fluctuate if there is a subsection of tightly coupled neurons. On the other hand, the demyelination perturbation suggests that because waves are all-or-none phenomena, they represent a resilient mechanism for neuronal communication. Demyelination is common in myelination diseases, such as Huntington's Disease and multiple sclerosis. In this framework, it is intuitive to understand why many symptoms are not expressed until demyelination reaches a critical point, at which neuronal function fall apart. Likewise, in the non-conducting gap of "dead tissue" (Figure 35) may be an example of post-infarction neuronal tissue. This hypothesis could explain the impairment of neuronal functions in context of the local characteristics and topology of the network where the cerebral infarction took place.

The exponential connectivity kernel imposes the longest-reaching connections (e^{-x}) (J. Zhang & Osan, 2016). The finite support kernel imposes the shortest ranging connections. Future studies could focus on the Gaussian kernel, which imposes mid-range connections (e^{-x2}). However, the

derivation of the evolution equations become more complicated for the Gaussian kernel inside the integral. For example, the first derivative of the Gaussian kernel e^{-x2} results in some integrals terms that did not exist before, such as $x \cdot e^{-x2}$. Furthermore, for additional derivatives, while some terms revert to existing factors, others correspond to higher order polynomicals, such as $x^2 \cdot e^{-x2}$ for the second order derivative. As a result, it is impossible to fully solve this infinite system of equations, although it could be possible to attempt to solve a finite system of equations that approximate the full one.

5.7 References

Ackman, J. B., Burbridge, T. J., & Crair, M. C. (2012, Oct). Retinal waves coordinate patterned activity throughout the developing visual system. *Nature*, *490*(7419), 219. doi: 10.1038/nature11529

Ackman, J. B., & Crair, M. C. (2014, Feb). Role of emergent neural activity in visual map development. *Curr. Opin. Neurobiol.*, *24*, 166–175. doi: 10.1016/j.conb.2013.11.011

Adinolfi, A. M., Yamuy, J., Morales, F. R., & Chase, M. H. (1991). Segmental demyelination in peripheral nerves of old cats. *Neurobiology of aging*, *12*(2), 175–179.

Bahramisharif, A., van Gerven, M. A. J., Aarnoutse, E. J., Mercier, M. R., Schwartz, T. H., Foxe, J. J., ... Jensen, O. (2013, Nov). Propagating Neocortical Gamma Bursts Are Coordinated by Traveling Alpha Waves. *J. Neurosci.*, *33*(48), 18849–18854. doi: 10.1523/JNEUROSCI.2455-13.2013

Belov, D. R., Stepanova, P. A., & Kolodyazhnyi, S. F. (2015, Nov). Traveling Waves in the Human EEG during Voluntary Hand Movements. *Neurosci. Behav. Physi.*, *45*(9), 1043–1054. doi: 10.1007/s11055-015-0184-7

Chrostowski, M., Yang, L., Wilson, H. R., Bruce, I. C., & Becker, S. (2011, Apr). Can homeostatic plasticity in deafferented primary auditory cortex lead to travelling waves of excitation? *J. Comput. Neurosci.*, *30*(2), 279–299. doi: 10.1007/s10827-010-0256-1

Compte, A., Sanchez-Vives, M. V., McCormick, D. A., & Wang, X.-J. (2003). Cellular and network mechanisms of slow oscillatory activity (¡1 hz) and wave propagations in a cortical network model. *Journal of neurophysiology*, *89 5*, 2707-25.

Cuellar, C. A., Tapia, J. A., Ju´arez, V., Quevedo, J., Linares, P., Mart´ınez, L., & Manjarrez, E. (2009, Jan). Propagation of Sinusoidal Electrical Waves along the Spinal Cord during a Fictive Motor Task. *J. Neurosci.*, *29*(3), 798–810. doi: 10.1523/JNEUROSCI.340808.2009

Dipierro, S., & Valdinoci, E. (2018, Jul). A Simple Mathematical Model Inspired by the Purkinje Cells: From Delayed Travelling Waves to Fractional Diffusion. *Bull. Math. Biol.*, *80*(7), 1849–1870. doi: 10.1007/s11538-018-0437-z

Ermentrout, B. (1998, May). The Analysis of Synaptically Generated Traveling Waves. *J. Comput. Neurosci.*, *5*(2), 191–208. doi: 10.1023/A:1008822117809

Ermentrout, B., Rubin, J., & Osan, R. (2006, Jul). Regular Traveling Waves in a OneDimensional Network of Theta Neurons. *SIAM J. Appl. Math.* Retrieved from https://epubs.siam.org/doi/abs/10.1137/S0036139901387253

Ferrer, I., & Planas, A. M. (2003). Signaling of cell death and cell survival following focal cerebral ischemia: life and death struggle in the penumbra. *Journal of Neuropathology & Experimental Neurology*, *62*(4), 329–339.

Kandel, E. R., Schwartz, J. H., Jessell, T. M., of Biochemistry, D., Jessell, M. B. T., Siegelbaum, S., & Hudspeth, A. (2000). *Principles of neural science* (Vol. 4). McGraw-hill New York.

Kang, S. H., Li, Y., Fukaya, M., Lorenzini, I., Cleveland, D. W., Ostrow, L. W., ... Bergles, D. E. (2013). Degeneration and impaired regeneration of gray matter oligodendrocytes in amyotrophic lateral sclerosis. *Nature neuroscience*, *16*(5), 571–579.

Kleinfeld, D., Delaney, K. R., Fee, M. S., Flores, J. A., Tank, D. W., & Gelperin, A. (1994, Sep). Dynamics of propagating waves in the olfactory network of a terrestrial mollusk: an electrical and optical study. *Journal of Neurophysiology*. doi: 10.1152/jn.1994.72.3.1402

Laan, A., Gutnick, T., Kuba, M. J., & Laurent, G. (2014, Aug). Behavioral Analysis of Cuttlefish Traveling Waves and Its Implications for Neural Control. *Curr. Biol.*, *24*(15), 1737–1742. doi: 10.1016/j.cub.2014.06.027

Lubenov, E. V., & Siapas, A. G. (2009, May). Hippocampal theta oscillations are travelling waves. *Nature*, *459*(7246), 534. doi: 10.1038/nature08010

Massimini, M., Huber, R., Ferrarelli, F., Hill, S., & Tononi, G. (2004, Aug). The Sleep Slow Oscillation as a Traveling Wave. *J. Neurosci.*, *24*(31), 6862–6870. doi: 10.1523/JNEUROSCI.1318-04.2004

Murakami, M., Kashiwadani, H., Kirino, Y., & Mori, K. (2005, Apr). State-Dependent Sensory Gating in Olfactory Cortex. *Neuron*, *46*(2), 285–296. doi: 10.1016/j.neuron.2005.02.025

Nauhaus, I., Busse, L., Ringach, D. L., & Carandini, M. (2012, Feb). Robustness of Traveling Waves in Ongoing Activity of Visual Cortex. *J. Neurosci.*, *32*(9), 3088–3094. doi: 10.1523/JNEUROSCI.5827-11.2012

Osan, R., Curtu, R., Rubin, J., & Ermentrout, B. (2004, Mar). Multiple-spike waves in a one-dimensional integrate-and-fire neural network. *J. Math. Biol.*, *48*(3), 243–274. doi: 10.1007/s00285-003-0228-4

Osan, R., & Ermentrout, B. (2001, Jun). Two dimensional synaptically generated traveling waves in a theta-neuron neural network. *Neurocomputing*, *38-40*, 789–795. doi: 10.1016/S0925-2312(01)00390-3

Osan, R., & Ermentrout, B. (2002, Mar). The evolution of synaptically generated waves in one- and two-dimensional domains. *Physica D*, *163*(3), 217–235. doi: 10.1016/S01672789(02)00347-0

Osan, R., Rubin, J., Curtu, R., & Ermentrout, B. (2003, Jun). Traveling waves in a onedimensional integrate-and-fire neural network with finite support connectivity. *Neurocomputing*, *52-54*, 869–875. doi: 10.1016/S0925-2312(02)00818-4

Phillips, O., Sanchez-Castaneda, C., Elifani, F., Maglione, V., Di Pardo, A., Caltagirone, C., ... Di Paola, M. (2013). Tractography of the corpus callosum in huntington's disease. *PloS one*, *8*(9), e73280.

Poll, D. B., & Kilpatrick, Z. P. (2017, Jul). Velocity integration in a multilayer neural field model of spatial working memory. *SIAM J. Appl. Dyn. Syst.* Retrieved from https://epubs.siam.org/doi/abs/10.1137/16M1102471

Raghupathi, R. (2004). Cell death mechanisms following traumatic brain injury. *Brain pathology*, *14*(2), 215–222.

Reimer, A., Hubka, P., Engel, A. K., & Kral, A. (2011, Jan). Fast Propagating Waves within the Rodent Auditory Cortex. *Cereb. Cortex*, *21*(1), 166–177. doi: 10.1093/cercor/bhq073 Rink, A., Fung, K.-M., Trojanowski, J. Q., Lee, V., Neugebauer, E., & McIntosh, T. K. (1995). Evidence of apoptotic cell death after experimental traumatic brain injury in the rat. *The American journal of pathology*, *147*(6), 1575.

Rubino, D., Robbins, K. A., & Hatsopoulos, N. G. (2006, Nov). Propagating waves mediate information transfer in the motor cortex. *Nat. Neurosci.*, *9*(12), 1549. doi: 10.1038/nn1802

Sato, T. K., Nauhaus, I., & Carandini, M. (2012, Jul). Traveling Waves in Visual Cortex. *Neuron*, *75*(2), 218–229. doi: 10.1016/j.neuron.2012.06.029

Takahashi, K., Saleh, M., Penn, R. D., & Hatsopoulos, N. (2011, Apr). Propagating Waves in Human Motor Cortex. *Front. Hum. Neurosci.*, *5*. doi: 10.3389/fnhum.2011.00040

Wanger, T., K. T., Lippert, M. T., Goldschmidt, J., & Ohl, F. W. (2013, Dec). Wave propagation of cortical population activity under urethane anesthesia is state dependent. *BMC Neuroscience*, *14*(1), 78. doi: 10.1186/1471-2202-14-78

Zanos, T. P., Mineault, P. J., Nasiotis, K. T., Guitton, D., & Pack, C. C. (2015, Feb). A Sensorimotor Role for Traveling Waves in Primate Visual Cortex. *Neuron*, *85*(3), 615–627. doi: 10.1016/j.neuron.2014.12.043

Zhang, H., & Jacobs, J. (2015, Sep). Traveling Theta Waves in the Human Hippocampus. *J. Neurosci.*, *35*(36), 12477–12487. doi: 10.1523/JNEUROSCI.5102-14.2015

Zhang, J., & Osan, R. (2016, May). Analytically tractable studies of traveling waves of activity in integrate-and-fire neural networks. *Phys. Rev. E*, *93*(5), 052228. doi: 10.1103/PhysRevE.93.052228

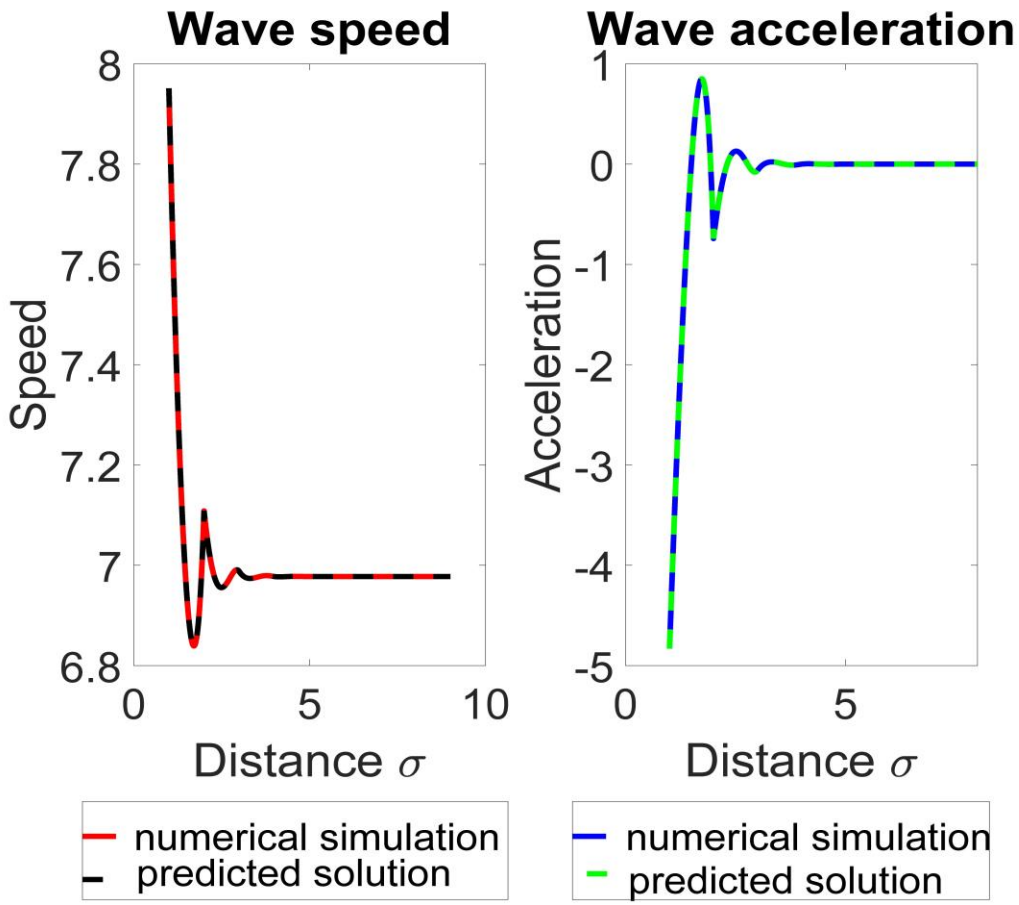

Figure 27. Comparison of analytical solutions and numerical simulations

The finite support neuronal network of integrate-and-fire neurons with excitatory coupling is at rest; at t=0, the neurons at x=0 to x=1 receive an additional current that drives them over the threshold. All shocked neurons spike synchronous because they receive their input at the same time. The wave evolution shows damped oscillations with an amplitude that decays exponentially. The self-propagating wave settles at the constant speed c_{fast}.

The left panel shows the wave speed as a function of space. The red trace is the computer simulation, and the black trace is the speed solution from Eq (4).

The right panel shows traveling wave acceleration as a function of space. The blue trace is the computer simulation, and the green trace is the solution from Eq. (6). Parameters: $g_{syn} = 15$, $\sigma = 1$, $\tau_1 = 1$, $\tau_2 = 2$, $V_T = 1$.

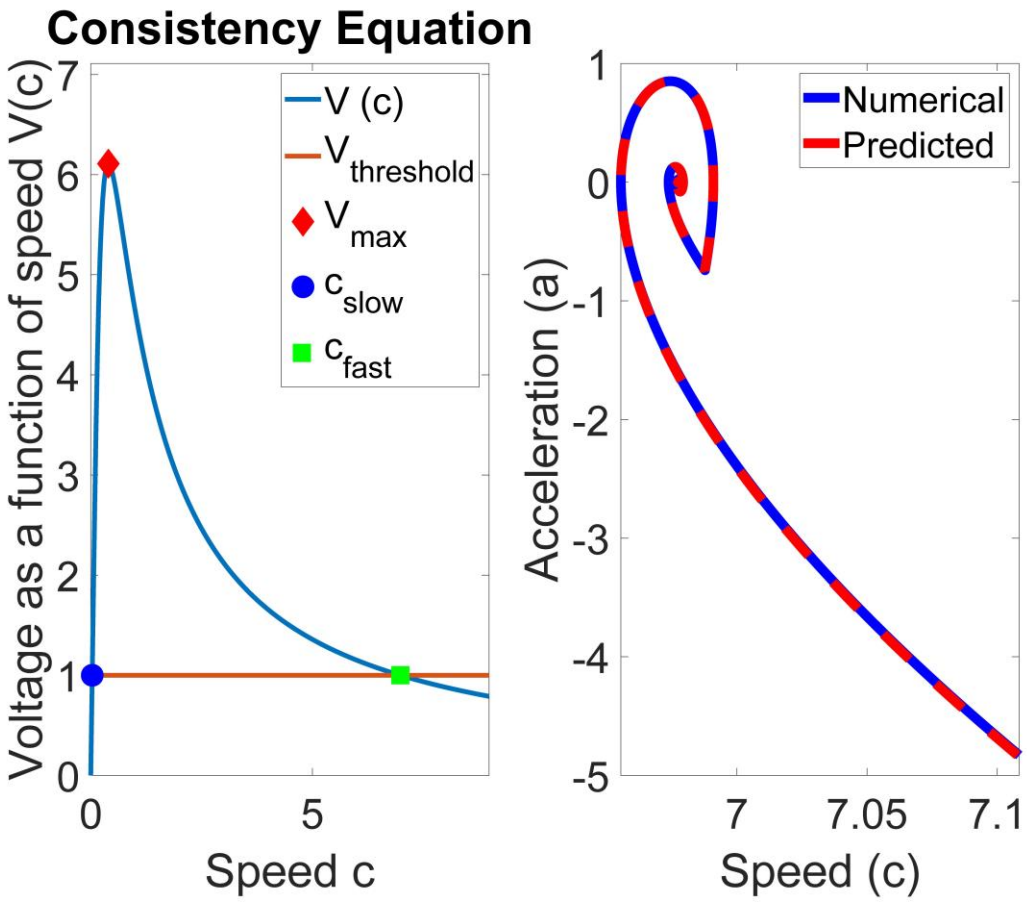

Figure 28. Stable and unstable fixed points of the wave propagation system.

The left panel graphs the solutions to the consistency equation as intersections between V = V(c) and the horizontal line at V_T. According to the consistency equation, the neuron membrane potential is a function of traveling wave speed. These numerical solutions allow one to compute both c_{fast} and c_{slow}. V_{max} denotes the maximum achievable voltage as a function of the traveling wave speed. If this value is less that V_T, no traveling wave can exist.

The right panel shows results from numerical simulations. The attractor graph of acceleration as a function of speed indicates that the traveling wave settles into a constant speed solution. The magnitude of the oscillations is consistent with the synaptic footprint space constant σ. The speed (c) and acceleration (a) of the traveling wave oscillate while approaching the intersection between c= c_{fast}, and a=0. Parameters: $g_{syn} = 15$, $\sigma = 1$, $\tau_1 = 1$, $\tau_2 = 2$, $V_T = 1$.

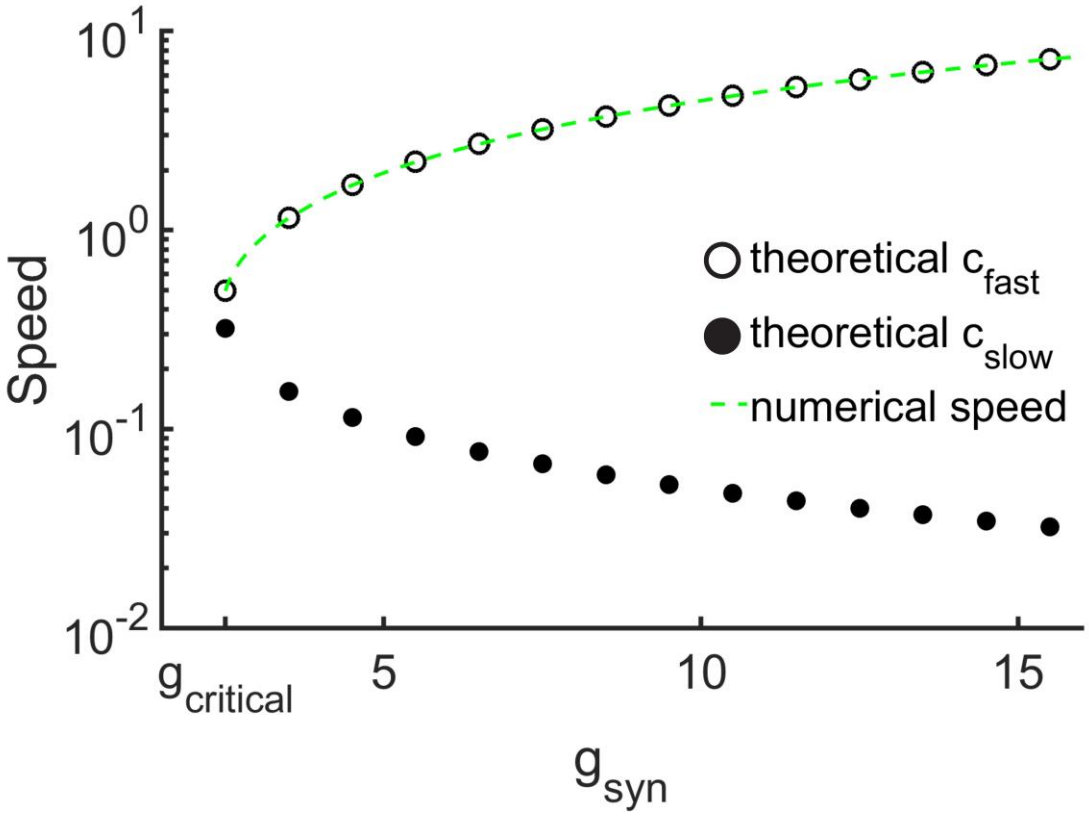

Figure 29. Traveling wave speed as a function of g_{syn}

This graph represents c_{fast} and c_{slow} as a function of global excitability parameter, in log scale. For this set of simulations, we systematically varied g_{syn} and kept all other parameters constant. Our results show there is a critical vallue (g_{crit}) where global excitation is so small that traveling wave activities are not sustainable. These curves also illustrate the dependence of traveling wave dynamics on global excitability: as g_{syn} grows, c_{fast} increases while c_{slow} decreases, both asymptotically.

Parameters: $\delta = 1e-3$ $\sigma = 1$, $\tau_1 = 1$, $\tau_2 = 2$, $V_T = 1$.

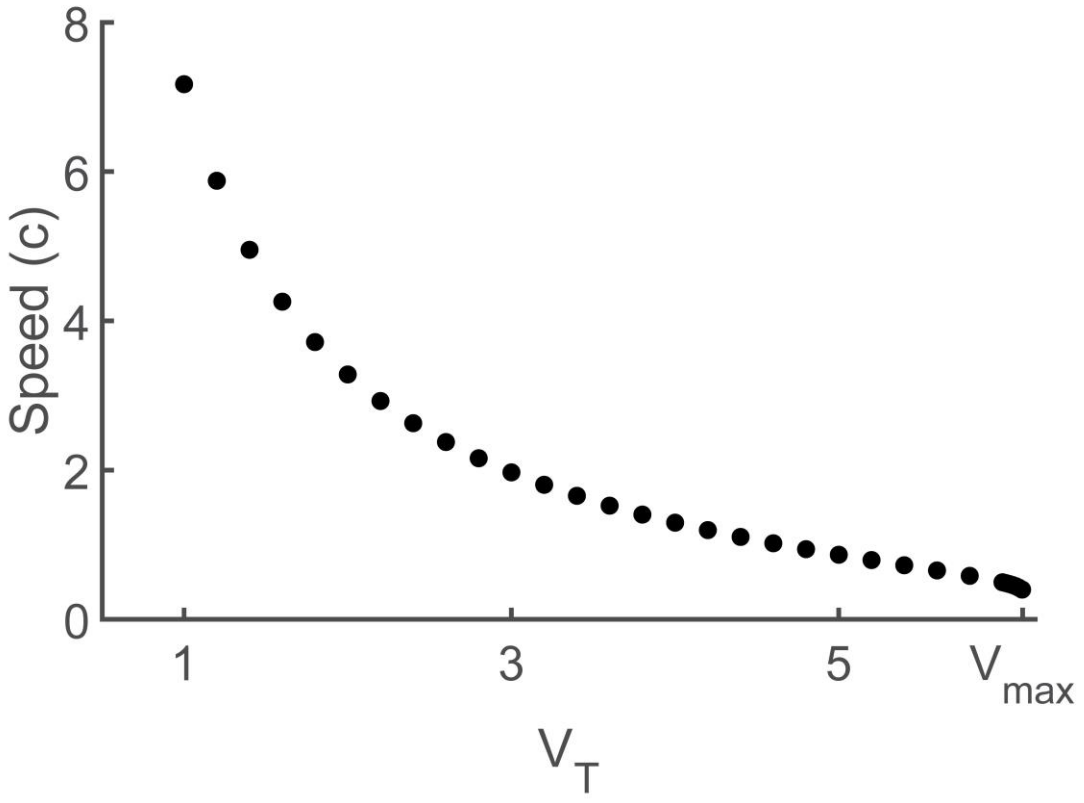

Figure 30. Traveling wave speed as a function of V_T

For this set of simulations, we systematically varied V_T and kept all other parameters constant.

Our results show that as V_T increases, the wave speed decreases.

The critical value V_{max} is the critical value between activity propagation and failure.

Parameters: $\delta = 1e-3$ $\sigma = 1$, $g_{syn} = 15$, $\tau_2 = 2$, $V_T = 1$.

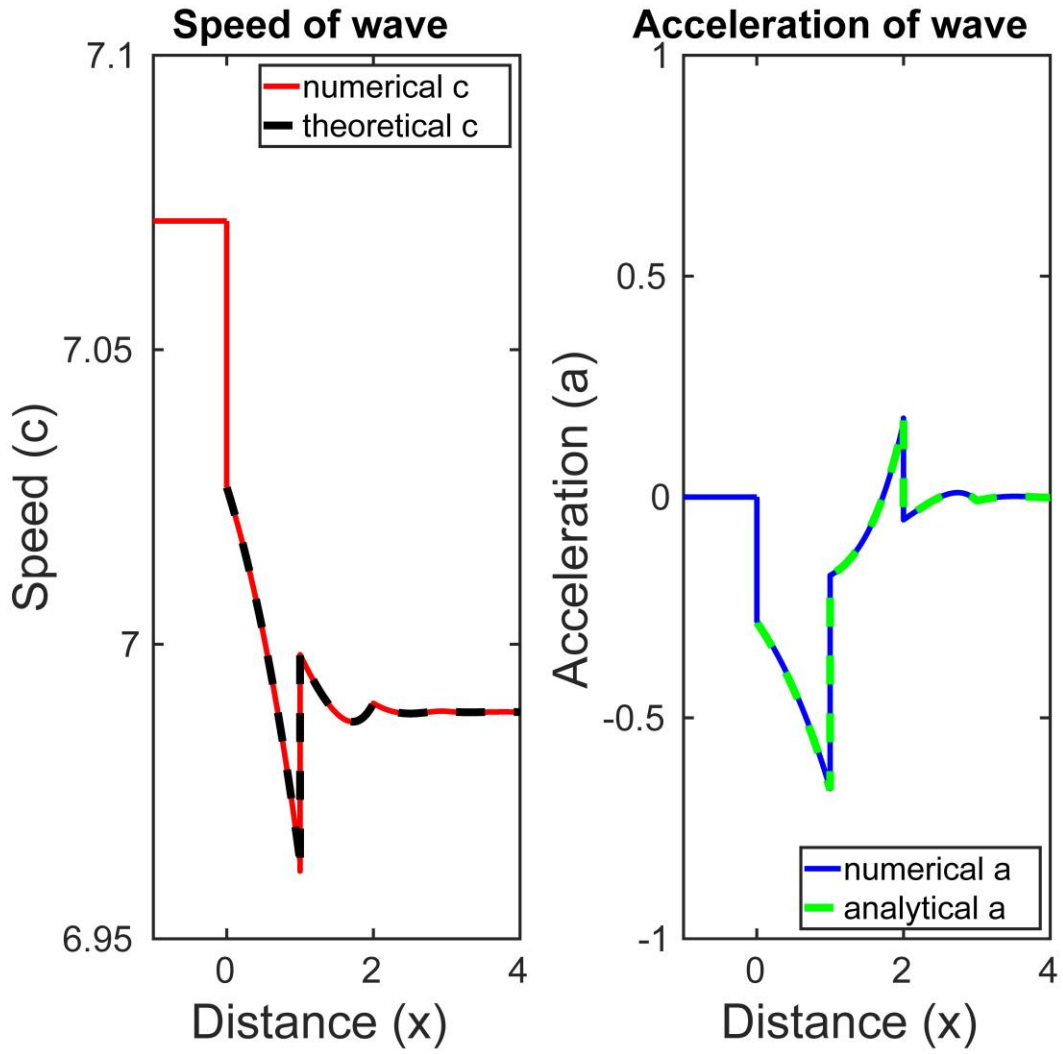

Figure 31. Faster wave speed perturbation

This graph shows the stability test of the wave speed solution c_{fast}. Without loss of generality, we consider a wave that prior to t=0 and x=0 travels at a slightly faster speed than the stable wave, that is, at $c_0 = c_{fast} + \epsilon \cdot c_{fast}$. The wave is initialized at a propagating speed faster than c_{fast}, due to an external drive. The wave travels from $\sigma = -\infty$ to σ=0 at a constant speed $c_0 = c_{fast} + \epsilon \cdot c_{fast}$. At x=0, there is no external drive, and the wave is free to evolve due to the dynamics defined by network and neuron parameters. Removal of the external drive creates a delay between the spiking time of the last neuron (with external drive) and the first neuron (without external drive).

Delay from numerical simulation: 8.6253e-4, delay from Eq. (15): 8.9347e-4. Initial speed after the break from simulation: 7.0253, initial speed from Eq. (16): 7.0225 Initial acceleration from simulation: -0.2914, initial acceleration from Eq. (17): -0.3095. V_1= -0.928915. The left panel displays traveling wave speed as a function of space. The red trace is the computer simulation, and the black trace is the result from Eq. (16).

The right panel shows traveling wave acceleration as a function of space. The blue trace is the computer simulation, and the green trace is the solution from Eq. (17) Note that acceleration is initially negative (the wave slows down), but then becomes positive because of the oscillations. Parameters: g_{syn} = 15, σ = 1, τ_1 = 1, τ_2 = 2, V_T = 1, and ϵ = 0.012

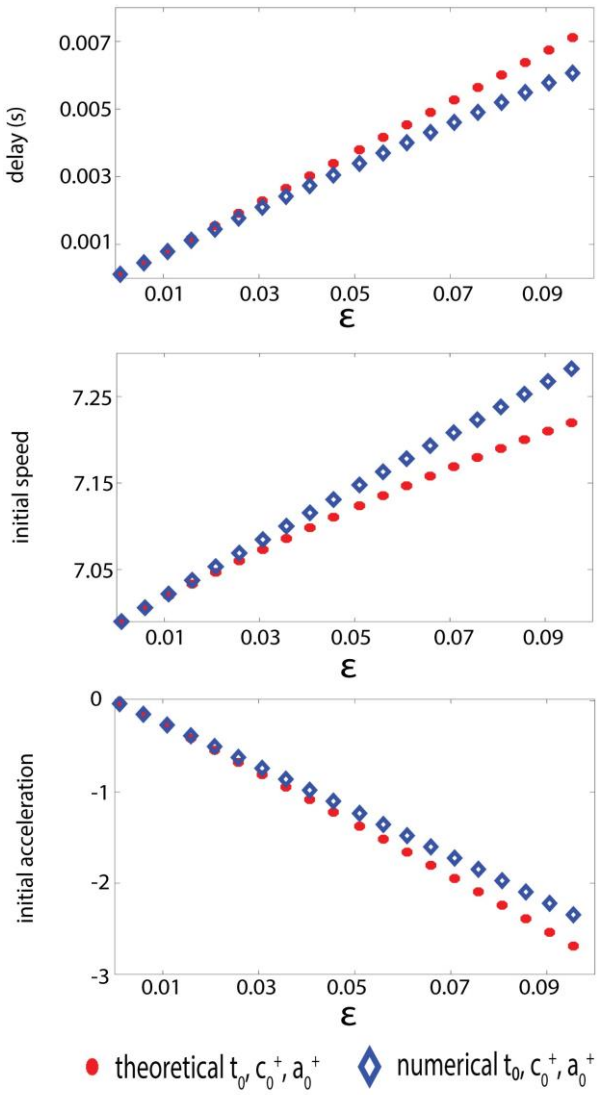

Figure 32. The accuracy of estimated delays as a function of ϵ

For these graphs, we performed multiple simulations with varying magnitudes for ϵ, and saved the delay, speed, and acceleration after the break. Here, we summarize the numerical and theoretical values of relevant wave characteristics after removing perturbation: numerical and theoretical t0, c0, and a0. These numerical and theoretical delays, speeds, and accelerations after pe rturbation removal show consistent trends dependent on control parameter ϵ. The range of relative error of *t*0 Eq. (15) compared to the numerical delay is [6.2e-6, 0.0011], c_0 Eq.(16) relative to the initial speed from simulations is [2.5e-4, 0.065], and a_0 Eq.(17) relative to the

numerical acceleration is [7.2e-4, 0.35]. For small values of ϵ, our approximations from Eqs.(15) (16), and (17) are accurate, but as ϵ increases, the system loses accuracy.

The top panel shows the delay computed from Eq. (15) and the delay from numerical simulations. The middle panel shows the speed computed from Eq. (16) and the speed from numerical simulations. And the bottom panel shows the acceleration computed from Eq. (17) and the acceleration from numerical simulations.

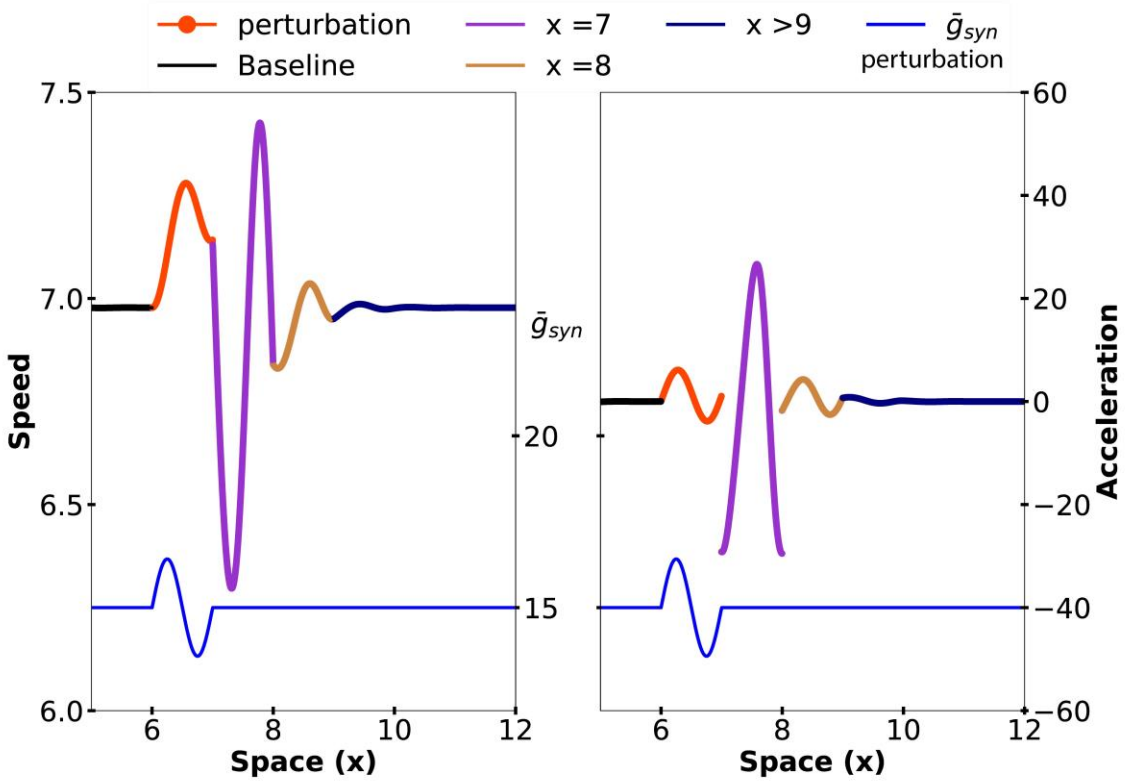

Figure 33. The wave speed oscillates as a function of both the synaptic coupling and the wave's state

Both Panels: The wave travels from x= 0 to x=12. The blue line at the bottom of the graph represents how $g_{syn}(x)$ oscillates as a function of space and the sinusoidal perturbation; g_{syn} is constant everywhere else.

If x > 6 and x< 7, $g_{syn}(x) = g \cdot (1 + \epsilon \cdot \sin(\frac{2\pi x}{\sigma}))$,

else $g_{syn}(x) = g$

The traveling wave speed fluctuated dramatically while the synaptic inhomogeneity perturbation was present. Because of the effect of the delayed parameters of the finite support kernel, this perturbation produced a peak of traveling wave speed after the perturbation was removed. Interestingly, the magnitude of the second peak was greater than the first peak.

The left panel illustrates that the speed of the wave at x =7 affects the speed of the wave at x=8; although the perturbation was totally removed at x>7. The wave speed peaks twice: The increase in local excitability $g_{syn}(x)$ causes the first peak. The delayed effect of wave speed ($t(x - \sigma)$, Eq. 3, $c(x - \sigma)$, Eq. 4) causes the second peak. This phenomenon exemplifies some of the complicated dynamics of the finite support connectivity kernel compared to the exponential.

The right panel illustrates how the traveling wave speed at any given “x” affects the instantaneous acceleration of the wave of subsequent “x+σ”. The instant acceleration oscillated transiently in a sinusoidal fashion while g_{syn} perturbation was present.

Parameters: g = 15, σ = 1, τ_1 = 1, τ_2 = 2, V_T = 1, δ = $1e^{-3}$,and ϵ = 0.0943

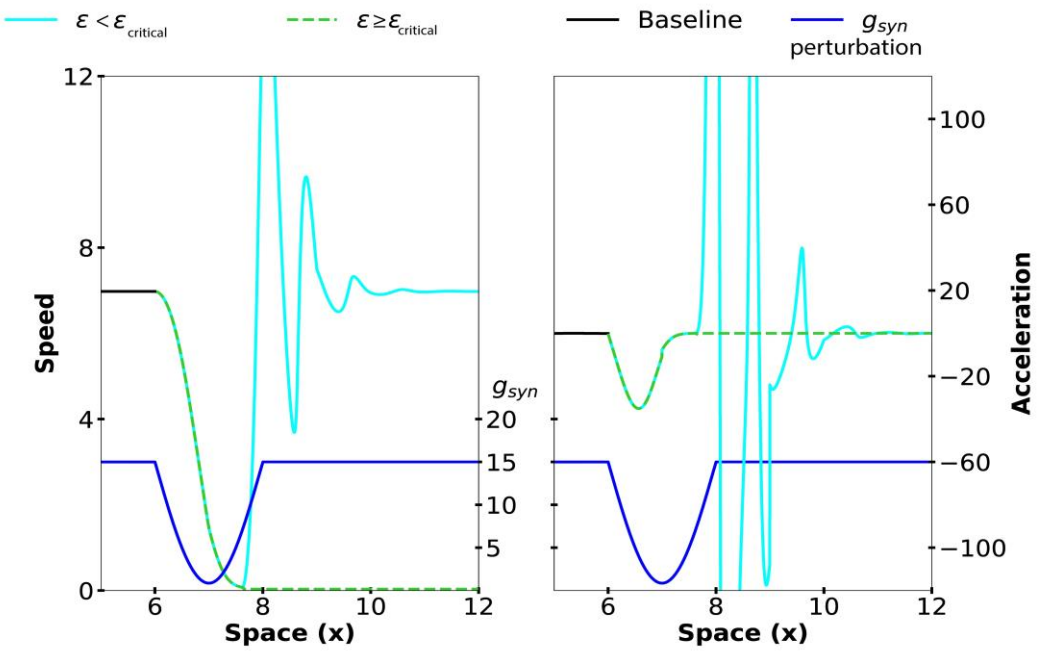

Figure 34. Neuronal traveling wave phenomena are all-or-none events: one small change in the control parameter separates activity propagation from propagation failure.

Both Panels: The wave travels from x= 0 to x=12. The blue line at the bottom of the graph represents how $g_{syn}(x)$ oscillates as a function of space and the demyelination perturbation. At the perturbation, g_{syn} decreases sharply; the g_{syn} decay is determined by:

if x > 6 and x < 7 $g_{syn} = g \cdot (1 + \epsilon 10 \sin(\frac{\pi x}{2\sigma}))$,

else $g_{syn}(x) = g$

The cyan and purple wave speeds demonstrate how a small increase in parameter ϵ (+1e-6) determines whether the perturbation terminates the wave or if the wave continues to propagate after removing the perturbation. The amplitude of the perturbation controls the breaking point of the traveling wave. Here, two simulations with the same initial conditions and parameters but with one difference in ϵ (+1e-6) differ qualitatively. The cyan wave continued to propagate, at c_{fast} wave speed; the purple wave failed to propagate.

Parameters: $g = 15, g_{syn} = 15$, $\sigma = 1$, $\tau_1 = 1$, $\tau_2 = 2$, $V_T = 1$, $\epsilon_1 = -0.094289$, $\epsilon_2 = -0.094288$.

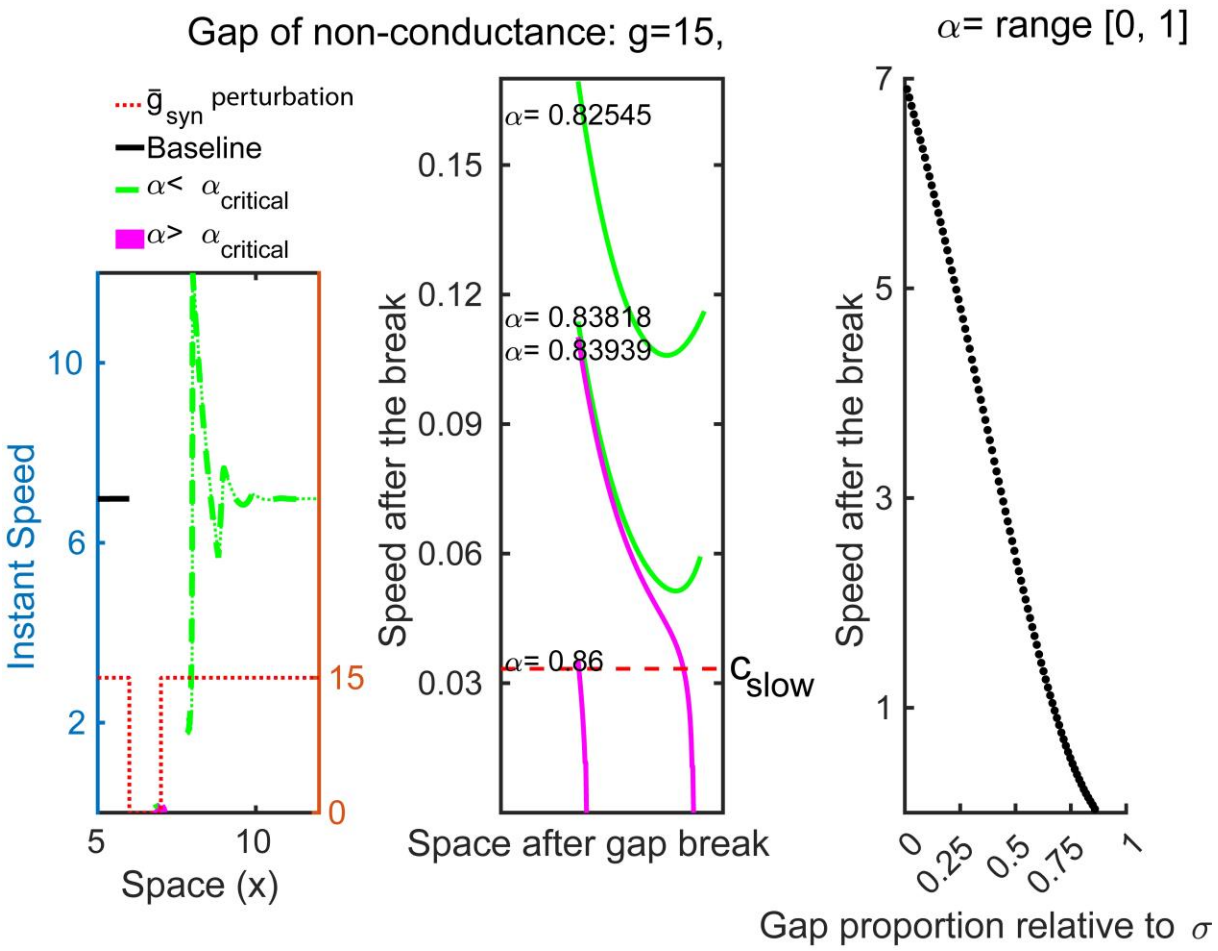

Figure 35. Dynamics of the traveling wave induced by a non-conducting gap

The simulation consists of a wave traveling at a constant speed c_{fast}, located at x = 6 there is the non-conducting gap of "dead neurons", which do not spike or synapse. The gap is relative to the synaptic space constant σ, and determined by the ratio: dead $gap = \alpha * \sigma$

To compute $\alpha_{critical}$, we uniformly sampled one hundred points between 0 and 1. Then iterated between 0.8 and 0.86, to find $\alpha_{critical}$ with 4-point decimal accuracy.

Left Panel The wave travels at a constant speed arriving at x = 6 (black trace). The green and magenta traces show the speed of the wave after the non-conducting gap results from multiple simulations; green curves represent $\alpha < \alpha_{critical}$, and magenta represent $\alpha > \alpha_{critical}$. As the non-conducting gap becomes larger, the wave speed after the break decreases. Larger gaps induce propagation failure.

Middle Panel Speed after the gap for the simulations with α near $\alpha_{critical}$. The green and magenta traces show a critical qualitative change in traveling wave evolution as a result of a small parameter change. **Right Panel** The speed after the gap is a monotonically decreasing function of the gap size.

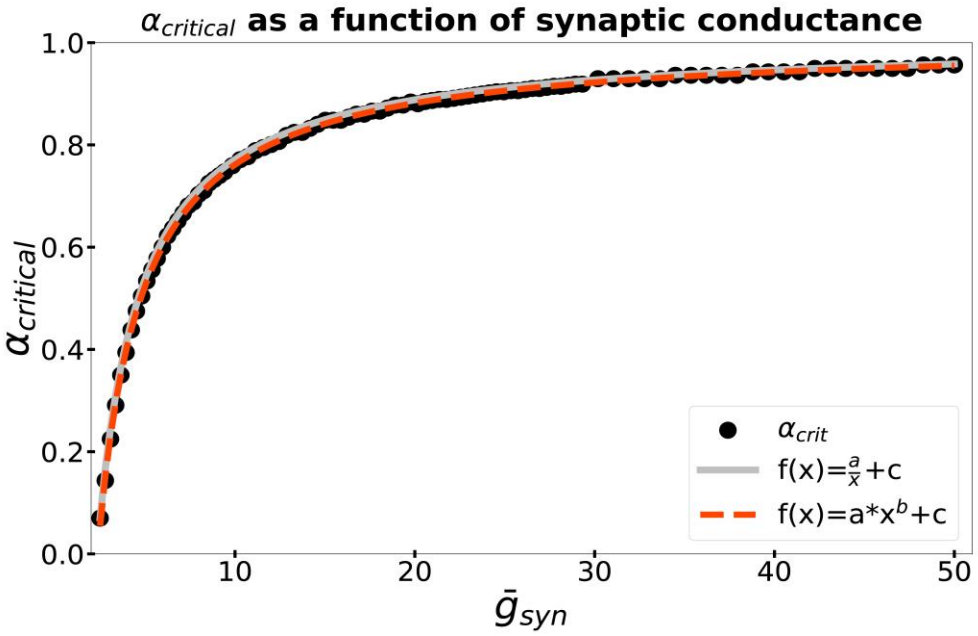

Figure 36. The smallest gap lengths that induce propagation failure gap=σα.

Networks with strong excitatory coupling allow for robust wave propagation. The data above shows the critical value of *α* as a function of network global excitability. The trend demonstrates that with greater excitability, the network's ability to sustain propagating traveling waves is more resilient to nonconducting-gaps (areas of dead tissue). Intuitively, this indicates that when overall network excitation is larger, more drastic reduction in the non-conducting gap is needed to produce propagation failure.

Curve fit analysis of $\alpha_{critical}$ as a function of g_{syn} demonstrated the power function was a good fit for the curve. $f(x) = a \cdot x^b + c$. b = -0.982 (-0.9904, -0.9736), c = 1.005 (1.003, 1.007), (SSE = 0.00284, R^2 = 1, Adjusted R^2 =

1, RMSE = 0.002918, p<0.1) Interestingly, the exponent is so close to -1 that other curves such as $f(x) = \frac{a}{x} + c$ are also a relatively good fit (SSE=0.00318, R^2 = 1, Adjusted R^2 = 1, RMSE=0.00317, p<0.01).

6 CONCLUSIONS

Neuronal rhythms are ubiquitous in neuronal activity. Rhythmic coordination of neuronal populations underlies neuronal synchronization important for memory consolidation, sleep, and many others. Life-sustaining motor functions such as heartbeat in the leech, and the breathing in humans require of robust and adaptive generation of neuronal rhythmicity. Bursting is a ubiquitous neuronal phenomenon that plays multiple roles in the nervous system and is critical for the functional activity of CPG neurons. This research aimed to investigate the mechanisms controlling the burst duration (BD) and interburst interval (IBI) of rhythmic bursting in isolated CPG interneurons (HN neurons) and rhythm propagation in neuronal networks, relevant to metachronal waves that control motor patterns. Metachronal waves are sequential propagation of synaptic activity down a linear network of neurons. It is well established that traveling waves organize CPG neuron activities to enable locomotion patterns such as swimming and crawling (Cacciatore & Rozenshteyn, 2000; Ijspeert, 2001; Ijspeert et al., 2007; Ijspeert et al., 1998; Iwasaki et al., 2014; Landsman & Slotine, 2012; Saltiel et al., 2016; Seo & Slotine, 2007). Determining the mechanisms that control the BD, IBI, and support propagation of synaptic activity are essential building blocks for the theory of motor systems.

Chapter 1 defined that the aims of the research were to (chapter 3) determine how the interaction between IP and Ipump, and the interaction between IP, Ih, and Ipump (chapter 4) determine the bursting characteristics of endogenous bursting neurons; in addition, we aimed to characterize the propagation of synaptic activity in a neuron network with strictly space-dependent connectivity (chapter 5). In isolated neurons (Chapters 2, 3 and 4), we sought to investigate a robust oscillatory mechanism formed by the interaction of I_P and I_{pump}. First, we applied a novel implementation of a dynamic clamp; our approach allowed us to estimate intracellular Na^+ concentration, simulate the Na^+/K^+ pump activity, and inject I_{pump} into a living interneuron. Dynamic clamp experiments allowed us to develop and test the 2D model in a way

not available with ordinary voltage recording and current clamp techniques (Chapter 2). Using dynamic clamp, we demonstrated that I_P upregulation gave rise to a new bursting regime (High Voltage Amplitude bursting regime- HVA; the baseline regime is the Low Voltage Amplitude bursting regime- LVA). In the HVA regime, manipulation of I_{pump} supports a flexible oscillatory mechanism that controls the BD and the IBI (Chapter 3); further, the h current (I_h) interacts with I_P and I_{pump} and plays a role in controlling the IBI (Chapter 4). Altogether these results elucidate the dynamics underlying burst rhythm generation that arise from the interaction of I_P, I_{pump}, and I_h.

In all our dynamic clamp experimental results, the roles of membrane currents are consistent with the literature. Specifically, the role of I_P is to initiate burst depolarization and facilitate spiking (Del Negro et al., 2002; Koizumi & Smith, 2008; Opdyke & Calabrese, 1994; Tazerart et al., 2008). The role of I_{pump} is to terminate bursts and maintain ion gradients in excitable neurons (Forrest et al., 2012; Kueh et al., 2016; Picton, Nascimento, et al., 2017; Pulver & Griffith, 2009; Tobin & Calabrese, 2005a). I_h plays an important role in determining the IBI (Kueh et al., 2016; Tobin & Calabrese, 2005a). However, although the individual role of these currents is well-characterized, the interaction between currents and the underlying dynamics of such interactions have remained elusive. Our interdisciplinary approach allowed us to supplement experimental results with computational modeling. Our analysis elucidated underlying dynamics that support the rhythmic characteristics recorded experimentally.

Although the Na^+/K^+ pump is widely expressed in excitable cells across taxa, the specific mechanisms underlying how Na^+/K^+ pump activity contributes to rhythmic bursting remain elusive to traditional experimental techniques. Our dynamic clamp technique allowed us to simulate and inject an artificial I_{pump} into a living rhythmically active CPG interneuron. In turn, manipulating the I_{pump} allowed us to control the pace of the neuron rhythm. However, one fundamental limitation of the technique is that we estimate $[Na^+]_i$ and inject current although we

do not directly inject Na^+ ions, we inject an outward current into the neuron. To control for such technical limitations, we developed a 2D model that accurately replicates the rhythmic characteristics recorded experimentally; despite its inherent simplicity, the 2D model is a powerful model for dynamical systems analyses. Altogether, we developed a series of theoretical and experimental tools that led us to our key findings that future investigators can use to further understand the Na^+/K^+ pump effects on burst dynamics. Future studies should investigate how pharmacological manipulations, such as adding myomodulin (inhibits I_{pump}, enhances I_h) or monensin (Na^+ ionophore, raises $[Na^+]_i$ and stimulates I_{pump}), affects the HVA rhythm of HN neurons. Moreover, future studies could use the 2D model to explore how the influx and efflux of Na^+ correlate with the phases of the rhythmic bursting activity and with membrane currents. Such studies could be essential to understanding how intracellular Na^+ concentration plays a role in neuronal activity. Lastly, based on the success of the 2D model, future studies could add one dynamic variable (for the activation of I_h, e.g.) and thoroughly investigate how the interaction of I_P, I_{pump}, and I_h controls the IBI.

In neuronal networks, we sought to characterize synaptic propagation with finite-support space-dependent coupling (chapter 5). The finite-support connectivity kernel is a robust network configuration that supports the propagation of synaptic activity. Consistent analytical and numerical solutions to traveling waves demonstrate that the finite-support kernel sustains synaptic activity propagation resilient to small and large perturbations (chapter 5).

This dissertation studied the control and propagation of neuronal rhythms. We demonstrated that I_P, I_h, and I_{pump} interact to form a flexible and robust rhythmic mechanism. The dynamic clamp experiments demonstrated that HN neurons have two bursting regimes. In the HVA regime, the Na^+/K^+ activity determines the BD and IBI, making the neuron rhythm flexible and adaptable to behavioral or environmental needs. We developed a neuron model and studied the dynamic systems underlying the neuronal rhythmic control. Finally, we investigated synaptic and

rhythmic activity propagation in a neuron network. Our results demonstrate that the finite-support connectivity kernel represents a resilient network configuration to propagate synaptic activity. Taken together, we identified a robust and flexible oscillatory rhythmogenic mechanism and a resilient synaptic connectivity kernel.

6.1 References

Angstadt, J. D., & Calabrese, R. L. (1989). A hyperpolarization-activated inward current in heart interneurons of the medicinal leech. *Journal of Neuroscience*, *9*(8), 2846-2857.

Angstadt, J. D., & Calabrese, R. L. (1991). Calcium currents and graded synaptic transmission between heart interneurons of the leech. *Journal of Neuroscience*, *11*(3), 746-759.

Ashlock, D. (2006). *Evolutionary Computation for Modeling and Optimization*. Springer-Verlag GmbH. https://www.ebook.de/de/product/12472033/daniel_ashlock_evolutionary_computation_for_modeling_and_optimization.html

Barnett, W., & Cymbalyuk, G. (2011a). Hybrid Systems Analysis: Real-Time Systems for Design and Prototyping of Neural Interfaces and Prostheses. *Biohybrid Systems: Nerves, Interfaces, and Machines*, 115–138.

Barnett, W., & Cymbalyuk, G. (2011b). Hybrid Systems Analysis: Real-Time Systems for Design and Prototyping of Neural Interfaces and Prostheses. *Biohybrid Systems: Nerves, Interfaces, and Machines*, 115-138.

Brines, M. L., Dare, A. O., & de Lanerolle, N. C. (1995). The cardiac glycoside ouabain potentiates excitotoxic injury of adult neurons in rat hippocampus. *Neuroscience letters*, *191*(3), 145-148.

Brodsky, J. L., & Guidotti, G. (1990). Sodium affinity of brain Na (+)-K (+)-ATPase is dependent on isozyme and environment of the pump. *American Journal of Physiology-Cell Physiology*, *258*(5), C803-C811.

Butera Jr, R. J., Rinzel, J., & Smith, J. C. (1999). Models of respiratory rhythm generation in the pre-Botzinger complex. II. Populations of coupled pacemaker neurons. *Journal of Neurophysiology*, *82*(1), 398-415.

Cacciatore, T. W., & Rozenshteyn, R. (2000). A kinematic and computational study of leech crawling: Support for a CPG based on travelling waves of excitation. *Journal of Neuroscience*, *20*, 1643-1655.

Calabrese, R. L. (1977). The neural control of alternate heartbeat coordination states in the leech, Hirudo medicinalis. *Journal of Comparative Physiology*, *122*(1), 111-143.

Calabrese, R. L., Norris, B. J., & Wenning, A. (2016). The neural control of heartbeat in invertebrates. *Current Opinion in Neurobiology*, *41*, 68-77.

Calabrese, R. L., & Prinz, A. A. (2009). Realistic modeling of small neuronal networks. In *Realistic modeling of small neuronal networks*: Cambridge, Mass.: MIT Press.

Calandriello, L., Curini, R., Pennisi, E. M., & Palladini, G. (1995). Spongy state (status spongiosus) and inhibition of Na, K-ATPase: a pathogenetic theory. *Medical hypotheses*, *44*(3), 173-178.

Canavier, C. C. (1999). Sodium dynamics underlying burst firing and putative mechanisms for the regulation of the firing pattern in midbrain dopamine neurons: a computational approach. *Journal of computational neuroscience*, *6*(1), 49-69.

Cohen, A. H., Ermentrout, G. B., Kiemel, T., Kopell, N., Sigvardt, K. A., & Williams, T. L. (1992). Modelling of intersegmental coordination in the lamprey central pattern generator for locomotion. *Trends in Neurosciences*, *15*(11), 434-438.

Cuellar, Tapia, J. A., Jurez, V., Quevedo, J., Linares, P., Martnez, L., & Manjarrez, E. (2009). Propagation of Sinusoidal Electrical Waves along the Spinal Cord during a Fictive Motor Task. *J. Neurosci.*, *29*(3), 798-810.

Cuellar, C. A., Tapia, J. A., Juárez, V., Quevedo, J., Linares, P., Martínez, L., & Manjarrez, E. (2009). Propagation of sinusoidal electrical waves along the spinal cord during a fictive motor task. *Journal of Neuroscience*, *29*(3), 798-810.

Cymbalyuk, G. S., & Calabrese, R. L. (2000). Oscillatory behaviors in pharmacologically isolated heart interneurons from the medicinal leech. *Neurocomputing*, *32*, 97-104.

Cymbalyuk, G. S., & Calabrese, R. L. (2001). A model of slow plateau-like oscillations based upon the fast Na+ current in a window mode. *Neurocomputing*, *38*, 159-166.

Cymbalyuk, G. S., Gaudry, Q., Masino, M. A., & Calabrese, R. L. (2002a). Bursting in leech heart interneurons: cell-autonomous and network-based mechanisms. *Journal of Neuroscience*, *22*(24), 10580-10592.

Cymbalyuk, G. S., Gaudry, Q., Masino, M. A., & Calabrese, R. L. (2002b). Bursting in leech heart interneurons: cell-autonomous and network-based mechanisms. *Journal of Neuroscience*, *22*, 10580–10592.

Del Negro, C. A., Koshiya, N., Butera Jr, R. J., & Smith, J. C. (2002). Persistent sodium current, membrane properties and bursting behavior of pre-botzinger complex inspiratory neurons in vitro. *Journal of Neurophysiology*, *88*(5), 2242-2250.

Dobretsov, M., & Stimers, J. R. (2005). Neuronal function and alpha3 isoform of the Na/K-ATPase. *Front Biosci*, *10*, 2373-2396.

Doloc-Mihu, A., & Calabrese, R. L. (2011). A database of computational models of a half-center oscillator for analyzing how neuronal parameters influence network activity. *Journal of biological physics*, *37*(3), 263-283.

Doloc-Mihu, A., & Calabrese, R. L. (2014). Identifying crucial parameter correlations maintaining bursting activity. *PLoS Comput Biol*, *10*(6), e1003678. https://doi.org/10.1371/journal.pcbi.1003678

Doloc-Mihu, A., & Calabrese, R. L. (2016). Analysis of family structures reveals robustness or sensitivity of bursting activity to parameter variations in a half-center oscillator (HCO) model. *eNeuro*, *3*(4).

Dou, Y., Pandey, S., Cartier, C. A., Miller, O., & Bishop, K. J. (2018). Emergence of traveling waves in linear arrays of electromechanical oscillators. *Communications Physics*, *1*(1), 1-9.

Eiben, A. (2015). *Introduction to evolutionary computing*. Springer.

Ellingson, P. J., Barnett, W. H., Kueh, D., Vargas, A., Calabrese, R. L., & Cymbalyuk, G. S. (2021). Comodulation of h- and Na$$/K$$ Pump Currents Expands the Range of Functional Bursting in a Central Pattern Generator by Navigating Between Dysfunctional Regimes. *The Journal of Neuroscience*, JN-RM-0158-0121.

Ellingson, P. J., Barnett, W. H., Kueh, D., Vargas, A., Calabrese, R. L., & Cymbalyuk, G. S. (2021). Comodulation of h- and Na(+)/K(+) Pump Currents Expands the Range of Functional Bursting in a Central Pattern Generator by Navigating between Dysfunctional Regimes. *J Neurosci*, *41*(30), 6468-6483. https://doi.org/10.1523/JNEUROSCI.0158-21.2021

Ellis, D. Z., Rabe, J., & Sweadner, K. J. (2003). Global loss of Na, K-ATPase and its nitric oxide-mediated regulation in a transgenic mouse model of amyotrophic lateral sclerosis. *Journal of Neuroscience*, *23*(1), 43-51.

Elson, R. C., & Selverston, A. I. (1997). Evidence for a persistent Na+ conductance in neurons of the gastric mill rhythm generator of spiny lobsters. *Journal of Experimental Biology*, *200*(12), 1795-1807.

Erazo-Toscano, R. J., Ellingson, P. J., Calabrese, R. L., & Cymbalyuk, G. S. (2021). Contribution of the Na/K Pump to Rhythmic Bursting, Explored with Modeling and Dynamic Clamp Analyses. *Journal of Visualized Experiments*(171).

Ermentrout, B., Rubin, J., & Osan, R. (2006). Regular Traveling Waves in a One-Dimensional Network of Theta Neurons. *SIAM J. Appl. Math.* https://epubs.siam.org/doi/abs/10.1137/S0036139901387253

Forrest, M. D., Wall, M. J., Press, D. A., & Feng, J. (2012). The sodium-potassium pump controls the intrinsic firing of the cerebellar Purkinje neuron. *PLoS One*, *7*(12), e51169.

Glitsch, H. G. n. (2001). Electrophysiology of the sodium-potassium-ATPase in cardiac cells. *Physiological Reviews*, *81*(4), 1791-1826.

Glynn, I. M. (1993). All hands to the sodium pump (Annual Review Prize Lecture). *J. Physiol*, *462*, 1-30.

Golowasch, J., Casey, M., Abbott, L. F., & Marder, E. (1999). Network stability from activity-dependent regulation of neuronal conductances. *Neural Computation*, *11*(5), 1079-1096.

Hage, T. A., & Salkoff, L. (2012). Sodium-activated potassium channels are functionally coupled to persistent sodium currents. *Journal of Neuroscience*, *32*(8), 2714-2721.

Harris-Warrick, R. M. (1993). Pattern generation. *Current Opinion in Neurobiology*, *3*(6), 982-988.

Harris-Warrick, R. M. (2002). Voltage-sensitive ion channels in rhythmic motor systems. *Current Opinion in Neurobiology*, *12*(6), 646-651.

Harris-Warrick, R. M., & Marder, E. (1991). Modulation of neural networks for behavior. *Annual review of neuroscience*, *14*(1), 39-57.

Hill, A. A. V., Lu, J., Masino, M. A., Olsen, O. H., & Calabrese, R. L. (2001a). A model of a segmental oscillator in the leech heartbeat neuronal network. *Journal of computational neuroscience*, *10*(3), 281-302.

Hill, A. A. V., Lu, J., Masino, M. A., Olsen, O. H., & Calabrese, R. L. (2001b). A model of a segmental oscillator in the leech heartbeat neuronal network. *Journal of computational neuroscience*, *10*, 281–302.

Hill, A. A. V., Masino, M. A., & Calabrese, R. L. (2002). Model of intersegmental coordination in the leech heartbeat neuronal network. *Journal of Neurophysiology*, *87*(3), 1586-1602.

Huczyski, A., Ratajczak-Sitarz, M., Katrusiak, A., & Brzezinski, B. (2007). Molecular structure of the 1: 1 inclusion complex of monensin A sodium salt with acetonitrile. *Journal of molecular structure*, *832*(1-3), 84-89.

Ijspeert, A. J. (2001). A connectionist central pattern generator for the aquatic and terrestrial gaits of a simulated salamander. *Biological cybernetics*, *84*(5), 331-348.

Ijspeert, A. J., Crespi, A., Ryczko, D., & Cabelguen, J.-M. (2007). From swimming to walking with a salamander robot driven by a spinal cord model. *science*, *315*(5817), 1416-1420.

Ijspeert, A. J., Hallam, J., & Willshaw, D. (1998). From lampreys to salamanders: evolving neural controllers for swimming and walking. From Animals to Animats, Proceedings of the Fifth International Conference of The Society for Adaptive Behavior (SAB98),

Itoh, Y., Law, M. J., & Sokoloff, L. (2000). Effects of the Na+/H+ exchanger monensin on intracellular pH in astroglia. *Brain research*, *882*(1-2), 226-229.

Iwasaki, T., Chen, J., & Friesen, W. O. (2014). Biological clockwork underlying adaptive rhythmic movements. *Proceedings of the National Academy of Sciences*, *111*(3), 978-983.

Jasinski, P. E., Molkov, Y. I., Shevtsova, N. A., Smith, J. C., & Rybak, I. A. (2013). Sodium and calcium mechanisms of rhythmic bursting in excitatory neural networks of the pre-B otzinger complex: a computational modelling study. *European Journal of Neuroscience*, *37*(2), 212-230.

Katz, P. S. (1996). Neurons, networks, and motor behavior. *Neuron*, *16*(2), 245-253.

Katz, P. S. (2016). Evolution of central pattern generators and rhythmic behaviours. *Philosophical Transactions of the Royal Society B: Biological Sciences*, *371*(1685), 20150057.

Kleinfeld, D., Delaney, K. R., Fee, M. S., Flores, J. A., Tank, D. W., & Gelperin, A. (1994). Dynamics of propagating waves in the olfactory network of a terrestrial mollusk: an electrical and optical study. *Journal of Neurophysiology*.

Koester, J., & Siegelbaum, S. A. (2013). Membrane potential and the passive electrical properties of the neuron. *Principles of neural science, Ed*, *5*, 126-147.

Koizumi, H., & Smith, J. C. (2008). Persistent Na+ and K+-dominated leak currents contribute to respiratory rhythm generation in the pre-Botzinger complex in vitro. *Journal of Neuroscience*, *28*(7), 1773-1785.

Kueh, D., Barnett, W. H., Cymbalyuk, G. S., & Calabrese, R. L. (2016). Na+/K+ pump interacts with the h-current to control bursting activity in central pattern generator neurons of leeches. *Elife*, *5*, e19322.

Landsman, A. S., & Slotine, J.-J. (2012). Control of traveling-wave oscillations and bifurcation behavior in central pattern generators. *Physical Review E*, *86*(4), 041914.

Lees, G. J. (1993). Contributory mechanisms in the causation of neurodegenerative disorders. *Neuroscience*, *54*(2), 287-322.

Li, Y.-X., Bertram, R., & Rinzel, J. (1996). Modeling N-methyl-D-aspartate-induced bursting in dopamine neurons. *Neuroscience*, *71*(2), 397-410.

Lin, W.-H., Gnay, C., Marley, R., Prinz, A. A., & Baines, R. A. (2012). Activity-dependent alternative splicing increases persistent sodium current and promotes seizure. *Journal of Neuroscience*, *32*(21), 7267-7277.

Luger, P. (1991). *Electrogenic ion pumps*.

Marder, E., & Bucher, D. (2001). Central pattern generators and the control of rhythmic movements. *Current Biology*, *11*(23), R986-R996.

Marder, E., & Calabrese, R. L. (1996). Principles of rhythmic motor pattern generation. *Physiological Reviews*, *76*(3), 687-717.

Marder, E., & Prinz, A. A. (2002). Modeling stability in neuron and network function: the role of activity in homeostasis. *Bioessays*, *24*(12), 1145-1154.

Masino, M. A., & Calabrese, R. L. (2002a). Period differences between segmental oscillators produce intersegmental phase differences in the leech heartbeat timing network. *Journal of Neurophysiology*, *87*(3), 1603-1615.

Masino, M. A., & Calabrese, R. L. (2002b). Phase relationships between segmentally organized oscillators in the leech heartbeat pattern generating network. *Journal of Neurophysiology*, *87*(3), 1572-1585.

Nadim, F., & Calabrese, R. L. (1997). A slow outward current activated by FMRFamide in heart interneurons of the medicinal leech. *Journal of Neuroscience*, *17*(11), 4461-4472.

Nadim, F., Olsen, y. H., De Schutter, E., & Calabrese, R. L. (1995). Modeling the leech heartbeat elemental oscillator I. Interactions of intrinsic and synaptic currents. *Journal of computational neuroscience*, *2*(3), 215-235.

Norris, B. J., Weaver, A. L., Morris, L. G., Wenning, A., Garca, P. A., & Calabrese, R. L. (2006). A central pattern generator producing alternative outputs: temporal pattern of premotor activity. *J. Neurophysiol.*, *96*(1), 309-326.

Olsen, y. H., & Calabrese, R. L. (1996). Activation of intrinsic and synaptic currents in leech heart interneurons by realistic waveforms. *Journal of Neuroscience*, *16*(16), 4958-4970.

Olsen, y. H., Nadim, F., & Calabrese, R. L. (1995). Modeling the leech heartbeat elemental oscillator II. Exploring the parameter space. *Journal of computational neuroscience*, *2*(3), 237-257.

Olypher, A., Cymbalyuk, G., & Calabrese, R. L. (2006a). Hybrid systems analysis of the control of burst duration by low-voltage-activated calcium current in leech heart interneurons. *Journal of Neurophysiology*, *96*(6), 2857-2867.

Olypher, A., Cymbalyuk, G., & Calabrese, R. L. (2006b). Hybrid systems analysis of the control of burst duration by low-voltage-activated calcium current in leech heart interneurons. *Journal of neurophysiology*, *96*, 2857–2867.

Opdyke, C. A., & Calabrese, R. L. (1994). A persistent sodium current contributes to oscillatory activity in heart interneurons of the medicinal leech. *Journal of Comparative Physiology A: Neuroethology, Sensory, Neural, and Behavioral Physiology*, *175*(6), 781-789.

Osan, R., & Ermentrout, B. (2002). The evolution of synaptically generated waves in one- and two-dimensional domains. *Physica D*, *163*(3), 217-235.

Osan, R., Rubin, J., Curtu, R., & Ermentrout, B. (2003). Traveling waves in a one-dimensional integrate-and-fire neural network with finite support connectivity. *Neurocomputing*, *52-54*, 869-875.

Picton, L. D., Nascimento, F., Broadhead, M. J., Sillar, K. T., & Miles, G. B. (2017). Sodium pumps mediate activity-dependent changes in mammalian motor networks. *Journal of Neuroscience*, *37*(4), 906-921.

Picton, L. D., Zhang, H., & Sillar, K. T. (2017). Sodium pump regulation of locomotor control circuits. *Journal of Neurophysiology*, *118*(2), 1070-1081.

Prinz, A. A., Abbott, L. F., & Marder, E. (2004a). The dynamic clamp comes of age. *Trends in neurosciences*, *27*, 218–224.

Prinz, A. A., Abbott, L. F., & Marder, E. (2004b). The dynamic clamp comes of age. *Trends in Neurosciences*, *27*(4), 218-224.

Prinz, A. A., Bucher, D., & Marder, E. (2004). Similar network activity from disparate circuit parameters. *Nature neuroscience*, *7*(12), 1345.

Pulver, S. R., & Griffith, L. C. (2009). Spike integration and cellular memory in a rhythmic network from Na+/K+ pump current dynamics. *Nat. Neurosci.*, *13*(1), 53-59.

Pusuluri, K., Li, Y., Hochman, S., & Prinz, A. A. (2021). Enhanced ensemble computational models of mouse thoracic sympathetic postganglionic neurons with offline compensation of electrode artifacts. Journal of computational neuroscience,

Rybak, I. A., Molkov, Y. I., Jasinski, P. E., Shevtsova, N. A., & Smith, J. C. (2014). Chapter 1 - Rhythmic Bursting in the Pre-Boo}tzinger Complex: Mechanisms and Models. *Progress in Brain Research*, *209*, 1-23.

Rybak, I. A., Shevtsova, N. A., Ptak, K., & McCrimmon, D. R. (2004). Intrinsic bursting activity in the pre-Botzinger complex: role of persistent sodium and potassium currents. *Biological cybernetics*, *90*(1), 59-74.

Rybak, I. A., Shevtsova, N. A., St-John, W. M., Paton, J. F. R., & Pierrefiche, O. (2003). Endogenous rhythm generation in the pre-Botzinger complex and ionic currents: modelling and in vitro studies. *European Journal of Neuroscience*, *18*(2), 239-257.

Saltiel, P., d'Avella, A., Wyler-Duda, K., & Bizzi, E. (2016). Synergy temporal sequences and topography in the spinal cord: evidence for a traveling wave in frog locomotion. *Brain Structure and Function*, *221*(8), 3869-3890.

Schmidt, J., Calabrese, R. L. (1992). Evidence that acetylcholine is an inhibitory transmitter of heart interneurons in the leech. *Journal of Experimental Biology*, *171*(1), 329-347.

Schmidt, J., Gramoll, S., & Calabrese, R. L. (1995). Segment-specific effects of FMRFamide on membrane properties of heart interneurons in the leech. *Journal of Neurophysiology*, *74*(4), 1485-1497.

Seo, K., & Slotine, J.-J. E. (2007). Models for global synchronization in CPG-based locomotion. Proceedings 2007 IEEE International Conference on Robotics and Automation,

Sharp, A. A., O'Neil, M. I. C. H. A. E. L. B., Abbott, L. F., & Marder, E. (1993). Dynamic clamp: computer-generated conductances in real neurons. *Journal of neurophysiology*, *69*, 992–995.

Sharples, S. A., Parker, J., Vargas, A., Milla-Cruz, J. J., Lognon, A. P., Cheng, N., Young, L., Shonak, A., Cymbalyuk, G. S., & Whelan, P. J. (2021). Contributions of h- and Na(+)/K(+) Pump Currents to the Generation of Episodic and Continuous Rhythmic Activities. *Front Cell Neurosci*, *15*, 715427. https://doi.org/10.3389/fncel.2021.715427

Simon, T. W., Opdyke, C. A., & Calabrese, R. L. (1992). Modulatory effects of FMRF-NH2 on outward currents and oscillatory activity in heart interneurons of the medicinal leech. *Journal of Neuroscience*, *12*(2), 525-537.

Skou, J. C. (1988). Overview: The Na, K-Pump. Methods. *Enzymol.*, *156*, 1-25.

Sorensen, M., Cymbalyuk, G., Calabrese, R., & DeWeerth, S. (2002). Effect of a hyperpolarization-activated inward current on rhythmic activity in a hybrid half-center

oscillator. In Ieee, Proceedings of the Second Joint 24th Annual Conference and the Annual Fall Meeting of the Biomedical Engineering Society][Engineering in Medicine and Biology,

Sorensen, M., DeWeerth, S., Cymbalyuk, G., & Calabrese, R. L. (2004a). Using a hybrid neural system to reveal regulation of neuronal network activity by an intrinsic current. *Journal of Neuroscience*, *24*(23), 5427-5438.

Sorensen, M., DeWeerth, S., Cymbalyuk, G., & Calabrese, R. L. (2004b). Using a hybrid neural system to reveal regulation of neuronal network activity by an intrinsic current. *Journal of Neuroscience*, *24*, 5427–5438.

Stimers, J. R., & Dobretsov, M. (1998). Adrenergic stimulation of Na/K pump current in adult rat cardiac myocytes in short-term culture. *The Journal of membrane biology*, *163*(3), 205-216.

Tazerart, S., Vinay, L., & Brocard, F. (2008). The persistent sodium current generates pacemaker activities in the central pattern generator for locomotion and regulates the locomotor rhythm. *Journal of Neuroscience*, *28*(34), 8577-8589.

Tobin, A.-E., & Calabrese, R. L. (2005a). Myomodulin increases I h and inhibits the Na/K pump to modulate bursting in leech heart interneurons. *Journal of Neurophysiology*, *94*(6), 3938-3950.

Tobin, A.-E., & Calabrese, R. L. (2005b). Myomodulin increases I h and inhibits the Na/K pump to modulate bursting in leech heart interneurons. *Journal of neurophysiology*, *94*, 3938–3950.

Van Vreeswijk, C., Abbott, L. F., & Ermentrout, G. B. (1994). When inhibition not excitation synchronizes neural firing. *Journal of computational neuroscience*, *1*(4), 313-321.

Wang, X.-J., & Rinzel, J. (1992). Alternating and synchronous rhythms in reciprocally inhibitory model neurons. *Neural Computation*, *4*(1), 84-97.

Wang, Y.-C., Yang, J.-J., & Huang, R.-C. (2012). Intracellular Na+ and metabolic modulation of Na/K pump and excitability in the rat suprachiasmatic nucleus neurons. *Journal of Neurophysiology*, *108*(7), 2024-2032.

Weaver, A. L., Roffman, R. C., Norris, B. J., & Calabrese, R. L. (2010). A role for compromise: synaptic inhibition and electrical coupling interact to control phasing in the leech heartbeat CpG. *Front. Behav. Neurosci.*, *4*.

Wenning, A., Cymbalyuk, G. S., & Calabrese, R. L. (2004). Heartbeat control in leeches. I. Constriction pattern and neural modulation of blood pressure in intact animals. *Journal of Neurophysiology*, *91*(1), 382-396.

Wenning, A., Hill, A. A. V., & Calabrese, R. L. (2004). Heartbeat control in leeches. II. Fictive motor pattern. *Journal of Neurophysiology*, *91*(1), 397-409.

Yokoyama, H., Hagio, K., Ogawa, T., & Nakazawa, K. (2017). Motor module activation sequence and topography in the spinal cord during air-stepping in human: Insights into the traveling wave in spinal locomotor circuits. *Physiological Reports*, *5*(22), e13504.

Zhang, H.-Y., Picton, L., Li, W.-C., & Sillar, K. T. (2015). Mechanisms underlying the activity-dependent regulation of locomotor network performance by the Na+ pump. *Scientific reports*, *5*, 16188.

Zhang, H.-Y., & Sillar, K. T. (2012). Short-term memory of motor network performance via activity-dependent potentiation of Na+/K+ pump function. *Current Biology*, *22*(6), 526-531.

Zhang, J., & Osan, R. (2016). Analytically tractable studies of traveling waves of activity in integrate-and-fire neural networks. *Phys. Rev. E*, *93*(5), 052228.